ANALYTICAL MODELING OF GRINDING PROCESS FOR IMPROVED PRODUCTIVITY, PART QUALITY AND MATERIAL PROPERTIES

by

HAMID JAMSHIDI

Submitted to the Graduate School of Engineering and Natural Sciences
in partial fulfillment of
the requirements for the degree of Doctor of Philosophy

Sabancı University
July 2021

ANALYTICAL MODELING OF GRINDING PORCESS FOR IMPROVED PRODUCTIVITY, PART QUALITY AND MATERIAL PROPERTIES

Approved by:

Approval: July 07, 2021

ABSTRACT

ANALYTICAL MODELING OF GRINDING PROCESS FOR IMPROVED PRODUCTIVITY, PART QUALITY AND MATERIAL PROPERTIES

HAMID JAMSHIDI

MANUFACTURING ENGINEERING, JANUARY 2021

Dissertation Supervisor: Prof. ERHAN BUDAK

Keywords: Grinding, force, temperature, analytical model, surface quality, burn, grit trajectory

Grinding is one of the oldest machining processes which accounts for about 25% of the total expenditure of machining operations in industry. It is mostly used in finishing operation of the parts to achieve the required final geometry, tolerance integrity and surface quality. For some special cases, it is also possible to use grinding technology to perform roughing operations, e.g. for difficult-to-cut materials. Due to many influential parameters and complicated nature of grinding, process conditions are mostly selected based on experience which cannot determine the optimum values. The aim of this thesis is to develop analytical models in grinding considering true physical mechanisms involved in the process. First of all, a kinematic-geometrical model to identify the real active number of grits and undeformed chip thickness is proposed as it is the fundamental parameter influencing the mechanics of the process. A thermomechanical force model is developed based on the trajectory of the grits. According to the model, the grinding force composed of three portions namely ploughing, cutting and dead metal zone. It has been showed that only the cutting portion of the force resulted in material removal and the ploughing and dead metal zone account for most of the grinding force. A new temperature model is also proposed based on the fundamentals of moving heat source theory. The state of the art is based on the fact that the heat source is time-dependent in nature instead of a constant heat source applied in the previous models. The theoretical results and experimental validations confirm that by considering the time-dependent heat source the workpiece temperature is predicted more accurately. The models are validated by measuring workpiece surface roughness and grinding force and workpiece temperature. Furthermore, surface burn as one of the thermally-induced

damages has been studied in this thesis analytically and experimentally. All models showed good agreements with the experimental data.

ÖZET

GELİŞTİRİLMİŞ VERİMLİLİK, PARÇA KALİTESİ VE MALZEME ÖZELLİKLERİ İÇİN ÖĞÜTME SÜRECİNİN ANALİTİK MODELLENMESİ

HAMID JAMSHIDI

ÜRETİM MÜHENDİSLİĞİ, OCAK 2021

Tez Danısmanı: Prof. Erhan Budak

Anahtar Kelimeler**:** Öğütme, kuvvet, sıcaklık, analitik model, yüzey kalitesi, yanık, tane yörüngesi

Taşlama, endüstrideki toplam işleme operasyonlarının yaklaşık %25'ini oluşturan en eski işleme süreçlerinden biridir. Çoğunlukla gerekli nihai geometriyi, tolerans bütünlüğünü ve yüzey kalitesini elde etmek için parçaların finiş işlemlerinde kullanılır. Bazı özel durumlarda, kaba işleme işlemlerini gerçekleştirmek için taşlama teknolojisini kullanmak da mümkündür, örn. kesilmesi zor malzemeler için. Taşlamanın birçok etkili parametresi ve karmaşık doğası nedeniyle, süreç koşulları çoğunlukla optimum değerleri belirleyemeyen deneyimlere dayalı olarak seçilir. Bu tezin amacı, süreçte yer alan gerçek fiziksel mekanizmaları dikkate alarak taşlamada analitik modeller geliştirmektir. Öncelikle, sürecin mekaniğini etkileyen temel parametre olduğu için gerçek aktif tane sayısı ve deforme olmamış talaş kalınlığını belirlemek için kinematik-geometrik bir model önerilmiştir. Tanelerin yörüngesine dayalı olarak bir termomekanik kuvvet modeli geliştirilmiştir. Modele göre taşlama kuvveti, pulluk, kesme ve ölü metal bölgesi olmak üzere üç kısımdan oluşmaktadır. Kuvvetin sadece kesme kısmının talaş kaldırma ile sonuçlandığı ve taşlama kuvvetinin çoğunu kesme ve ölü metal bölgesinin oluşturduğu gösterilmiştir. Hareketli ısı kaynağı teorisinin temellerine dayanan yeni bir sıcaklık modeli de önerilmiştir. Tekniğin bilinen durumu, önceki modellerde uygulanan sabit bir ısı kaynağı yerine, ısı kaynağının doğası gereği zamana bağlı olduğu gerçeğine dayanmaktadır. Teorik sonuçlar ve deneysel doğrulamalar, zamana bağlı ısı kaynağı dikkate alınarak iş parçası sıcaklığının daha doğru bir şekilde tahmin edildiğini doğrulamaktadır. Modeller, iş parçası yüzey pürüzlülüğü, taşlama kuvveti ve iş parçası sıcaklığı ölçülerek doğrulanır. Ayrıca, termal kaynaklı hasarlardan biri olan yüzey

yanığı, bu tezde analitik ve deneysel olarak incelenmiştir. Tüm modeller deneysel verilerle iyi uyum göstermektedir.

ACKNOWLEDGEMENTS

From the bottom of my heart I would like to thank my patient and supportive supervisor Prof. Erhan Budak who provided this opportunity for me to do this research at Sabanci University. Without his knowledge, support this thesis could not be completed.

I would like to thank the member of committee Prof. Mostafa Bakkal, Prof. Yusuf Ziya Menceloğlu, Prof. Lütfi Taner Tunç, and Prof. Umut Karagüzel.

Most of the works and experiments for this thesis were carried out at Manufacturing Research Lab (MRL) at Sabanci University and I am truly grateful for its staff and Maxima R&D members who helped me building fixtures, providing materials especially Dr. Emre Özlü, Muharrem Sedat Erberdi, Suleyman Turkan, Veli Nakşiler and Ertugrul Sadikoglu.

A great appreciation would go to my friends at material science engineering department who helped me for SEM and microscopy measurements of the samples. I would like to thank especially Dr. Ali Tufani, Dr. Sirous Khabbazabkenar and Dr, Pozhhan Mokhtari for their valuable help.

I am grateful to all students who did their B.Sc and M.Sc thesis on grinding. The results of their work helped me a lot to do this research especially my friends Mert Gurtan, Batuhan Yastıkçı, Mert Kocaefe.

Last but not least, I am grateful to my parents and family members. My wife Baran without her support, patient and love this work could not be finished.

Istanbul, July 2021

Hamid Jamshidi

To my Lovely wife, Baran

without her support, encouragement and love

this work could not be possible.

TABLE OF CONTENTS

Contents

LIST OF TABLES

LIST OF FIGURES

1 INTRODUCTION

1.1 Introduction and Literature Survey

Grinding, as one of the common abrasive machining processes, has some characteristics that make it distinguished from all other material removal operations from industrial and scientific perspectives. First of all, the surface finish of the products produced by this process could be up to 10 times better than in turning or milling [1]. It accounts for about 25% of the total expenditure of machining operations in industry according to Malkin [2]. Since grinding is generally the final operation on a part, the surface integrity is of high importance. This process is essential for the parts required tight tolerances and high precision. From scientific point of view, due to very high negative rake angles of the grits on a grinding wheel, chip formation mechanism could differ substantially from machining. In addition, material removal occurs in micro level in grinding such that the maximum undeformed chip thickness varies from 0.5-10 μm and the contribution of rubbing and ploughing mechanisms are considerable compared to other metal removal processes. Because of the complexity of the process with so many variables, selection of grinding conditions has mostly been done based on trial and error or experience. Figure 1-1 shows a schematic view of different aspects of the grinding with related parameters. Modelling of the process provides the ability to select proper grinding parameters so that depending on the production strategy optimum conditions can be acquired. In some cases, rapid wheel wear increases the tool cost whereas in some other cases improper selection of the grinding parameters results in surface burn. These problems can be avoided if a comprehensive grinding model could predict the process outcome. In addition, having grinding models provides the opportunity to improve the efficiency of the process. Recently engineered wheels in which the grits are positioned on the wheel with a specific pattern gained attention to improve the efficiency of the process. Evaluation of their performance and finding which specific patterns provide the optimum conditions can only be achieved by process modelling. These considerations show the necessity and the importance of process modelling.

Figure 1-1- different aspects of the grinidng process and related parameters

Different aspects of the grinding process have been studied so far and the focus is mainly on surface topography, grinding force and workpiece temperature and related issues [3]. Grit-workpiece interaction can be obtained by simulation of grit trajectory and the models which consider the shape of the grits have been known as kinematic-geometrical models according to Brinksmeier et.al. [3]. A primary stage in kinematic-geometrical modeling of the grinding processes has been wheel topography modeling. Many researchers have investigated the characteristics of the grinding wheel [4] and used different models for simulation purposes[5]. Aslan and Budak [6] measured the geometric properties of grooved and regular wheels through optical measurement systems and modeled the grinding wheel by constructing a Gaussian distribution function based on experimentally obtained properties of the individual grits. Nguyen and Butler [7] developed a numerical procedure based on random field theory to generate the surface of a grinding wheel. Chakrabarti and Paul [8] developed another simulation technique by assuming square pyramidal grit shape to generate the surface topography of the wheel. In another work as an experimental approach, Darafon et al.

[9] developed a non-contact scanning system by using a white light chromatic sensor traversing across the wheel surface to measure grit characteristics such as cutting edge density, width, spacing and protrusion height. Chang and Wang [10] developed a grinding force model incorporating the random nature of grits by introducing a stochastic grit density function. Yu et al. [11] introduced a model of dynamic cutting point density for an engineered grinding wheel. Aurich et al. [12] developed kinematic equations assuming different patterns for an engineered wheel and produced an optimized prototype engineered wheel to improve process stability and workpiece surface quality. Yet, application of most of these models in a kinematic-geometrical grinding model that represent the real physical mechanism of chip formation process is restricted since they are time-consuming in practice and have not considered some important geometrical properties of the grits such as cutting angles and edge radii.

In relation to kinematic-geometrical modeling of the process, the number of cutting edges interacting with the workpiece, which is called active number of grits, is the most critical parameter that has also been hardly possible to capture directly. The need for identification of the active number of grits is that, unlike milling tools, the number of teeth participating in the cutting process is not known in a grinding wheel due to height differences of the grits. Therefore, it must be known for accurate modeling and simulation of any abrasive process. For this reason, many approaches have been utilized in the literature to predict it. Cai and Rowe [4] introduced active cutting edge density as one of the main parameters of the wheel and assumed that they are the topmost grits which could be identified by counting those having higher height than a certain radial depth. Identification of the active number of grits based on investigation of the wheel characteristics can only provide a static active number of grits. This approach cannot provide the real active number of grits during the process since it does not consider the dynamic effects. Furthermore, there is no theoretical explanation on how that certain radial depth could be identified. Some other researchers developed different empirical models to identify the active grits more precisely. Malkin and Guo [13] correlated the dynamic number of active grits with the infeed angle (ε) rather than the radial depth by a power function:

$$C_{dyn} = C_0(\tan\varepsilon)^m \tag{1.1}$$

where C_0 and m are experimentally identified constants for a particular wheel and dressing conditions. Hecker et al. [14] developed another empirical model correlating the dynamic active number of grits with infeed angle and the static active number of grits as follows:

$$C_{dyn} = \frac{C_{static}}{1 + \frac{C_{stat}}{3} \frac{\tan\theta}{\tan\varepsilon} \frac{E(h^3)}{z}} \quad , C_{static} = A(z)^k \qquad (1.2)$$

where, C_{stat} is static number of active grits, A and k are empirical constants, θ is grit cone angle, z is radial distance into the wheel, $E(h)$ is expected value function of chip thickness estimated by Rayleigh probability distribution function. The empirical constants used in this model were calibrated by using them in another empirical force model. The problem of this kind of modeling is that they need experimental coefficients as mentioned above and may not show the real active grits since the dynamics of the process are not taken into account. Recently, more advanced kinematic models have been developed which concentrate on the micro interaction of grit-workpiece. Jiang et al. [15] developed a numerical model describing the micro interaction of workpiece-grit and concluded that there are four kinds of grits including non-contact, sliding, ploughing and cutting grits. However, validation of the model was done by comparing the surface roughness obtained from the simulations and the experiments only perpendicular to the cutting direction. Furthermore, grits were modeled as spherical which may not represent the proper geometrical properties of the grits. In addition, the criteria for the classification of grits as sliding and ploughing must be obtained experimentally. Ding et al. [16] modeled a textured monolayer CBN wheel and predicted the undeformed chip thickness and surface roughness of the workpiece by considering trajectories of the grits. They reported the surface roughness values only perpendicular to the cutting direction and there is no discussion on the active number of grits and its effect on the process. In another study, Li et al. [17] developed a grinding force model by considering variable stages of grit-workpiece micro interaction. The kinematic analysis of cutting grits was validated by comparing the force obtained experimentally with the model. Since many assumptions and experimental coefficients needed in the force model, the validation of kinematic analysis in this way is questionable. Zhang et al. [18] raised the concept of distribution of the undeformed chip thickness by simulating the kinematic equations of the grinding process for a single-layer brazed diamond wheel fabricated for their study without discussion on the active number of grits. They validated their wheel model by comparing the grit density and validated their kinematic model by comparing surface roughness of the workpiece only perpendicular to the cutting direction.

Another important issue in grinding wheel modeling is type of distribution of the grit and grit modeling itself. Ding et al. [16] manipulated the measured grain protrusion height by using Johnson transformation to reconstruct a normal distribution. Koshy et al. [19] used a uniform penetration height distribution for a fresh diamond grinding wheel. In a similar method, J. L. Jiang et al. [20] used normal distribution function in their MATLAB code for grain diameters. However, before using a normal distribution function, data should be examined statistically (analysis of normality) to see whether they follow a normal distribution.

Kinematic geometrical models provides calculation of undeformed chip thickness Undeformed chip thickness is an important parameter in grinding force model and also affects the surface quality of the ground parts, specific energy, temperature and wheel wear. Consequently, control of the required force is a key factor to achieve better surface quality and to increase productivity. A lot of efforts have been devoted by researchers to predict the grinding force through modeling. Most early force models were empirical in which force was expressed by the product of main process variables such as feed rate, depth of cut, wheel diameter, cutting edge density, workpiece properties where each variable had a constant [21]. In some cases, the main variables themselves were modeled empirically to be used in the final force equation [22]. These models predict the force magnitude with high accuracy; however, a large number of experiments are required to identify the constants which are restricted to a specific wheel and workpiece pair. Later, researchers tried to develop more advanced models based on different theories of material removal mechanisms. Malkin and Guo [13] expressed the force in terms of energy consisting of sliding energy, ploughing energy and the energy required for chip formation:

$$U = U_{sl} + U_{pl} + U_{chip} \tag{1.3}$$

They attributed the high specific grinding energy to the high shear stress needed for chip formation due to the poor condition of grinding grits and correlated it to the energy required to melt the workpiece material. Shaw [23] assumed the wheel grit shape as a sphere and claimed that the grinding mechanism differs from other cutting processes where an extrusion-like mechanism is involved in grinding. He proposed a hardness model of chip formation in which the normal force is related to the hardness of the workpiece. Chen and Rowe [24] used the grinding force model of Shaw and simulated the cutting action of every grit and workpiece surface. They did not provide any direct validation of the grinding force simulation, but instead compared the ground surface of the workpiece and reported a similar surface feature of simulation results with the experiment. Scanning electron microscopy (SEM) of the grinding swarf, especially for ductile materials has revealed the similarity of the grinding chip with the chip obtained from other machining processes [13] which was in contrast to Shaw's assumption. By observing under SEM Doyle and Dean [25] distinguished three types of grinding debris namely, particles with no characteristic shape, spherical particles and chips. The debris obtained from surface grinding of medium-carbon steel led the authors to conclude that a large amount of debris is in the form of chips similar to the other cutting processes. Furthermore, the quick stop device used to study material removal in grinding showed direct evidence of chip formation similar to other machining operations. Statistical evaluation of more than 120 samples of chips obtained by quick stop test conducted by Buda and Liptak [26] showed 1/3 of the obtained chips pointed to pure cutting i.e. chip is formed in a shearing process similar to the other metal cutting processes while the rest of the samples showed that pure cutting was accompanied by a ploughing mechanism. In another study, Denkena et al. [27] investigated the chips during up grinding and showed the formation of the fine continuous chip when the grit is at the exit zone. Malkin and Hwang [28] reviewed the grinding mechanism of ceramics considering both indentation fracture mechanics and machining approach. They concluded that even though both methods provided a good insight into the grinding process, the indentation fracture mechanics could not be applied in real grinding operations due to the dissimilarity of the indentation tool with the random-oriented grits. Furthermore, the effect of consecutive grinding scratches and high stress, stress rate and temperature in the grinding zone cannot be modeled by the indentation test. Experimental investigation and FEM simulations of single scratching tests were also performed in the literature to enhance the knowledge of the chip formation mechanism.

Anderson et al. [29] modeled the grit as a spherical shape and concluded the cutting speed can change the force component via changing the strain rate hardening of the workpiece material and coefficient of friction. They later [30] compared the spherical and truncated cone tools and concluded that the truncated cone geometry had better perfomanceand spherical geometry can be used to model dull abrasive grain. Axinte et al. [31] manufactured different grit shapes including square, triangle and circular grits and studied the influence of grit geometry on the material removal mechanism. They showed that a girt shape with higher number of cutting can reduce the specific cutting force for the ductile material. Rasim et.al [32] investigated the effect of grinding grit angles on the mechanism of chip formation. They concluded that the length of different deformation zones i.e. rubbing, ploughing and cutting was affected by the grit angles. Transchel et al. [33] studied the effect of clearance angle on the ploughing and cutting portion of the grinding force. By changing the clearance angle from -1 to +7 degrees in the single grit scratching test, they showed that a small negative clearance angle could increase the grinding force profoundly.

The basic mechanisms of chip formation and grinding behavior most resemble the metal cutting process [34] and milling analogy has been adopted to model the process in surface grinding [35] or when a grooved wheel is used [36]. However, there are some important aspects such as the stochastic nature of the grinding wheel and the high negative rake angle of the grits, which should be taken into account in the models. Measuring [37] and simulating the surface topography of the wheel [38] considering dressing and wear effects [15], provide models for the stochastic nature of the grinding. In addition, machining with a negative rake angle is not limited to grinding and has been reported in other machining operations such as machining with chamfered tools [39], hard turning [40], micro [41] and nano machining [42]. Experimental results showed the existence of a triangle region formed ahead of the tool tip [43] which preserved its shape and changed the geometry of the tool. The results of quick stop test with a single grit grinding wheel confirmed the formation of the dead zone in grinding in specific circumstances as it was discussed in [44] and [45]. However, to the best knowledge of the author, the effect of the dead metal zone has not yet been considered in the grinding force models.

Almost all force models proposed in the literature need some calibration tests where experiments are needed to identify the empirical coefficients in the model. Experimental constants appear in the determination of the cross-sectional area of the grit, [46] or grinding forces per grit [47]. Recently, Li et al. [17] proposed a detailed force model using the indentation fracture mechanics developed by Shaw [23] which is able to predict the force profile in a micro scale. Even in that model, some constants must be obtained experimentally. For example, the critical indentation depths defined as the depth above which the chip is formed, have been obtained from the results of a single diamond grain test reported in [48].

In addition to the calibration problem of the current force models, the force coefficients for a single grit obtained from the experiments had very high values. Values of 20-36 GPa were reported for the force coefficients in the literature [49] for different metal workpiece materials which are much higher than the yield strengths of those materials. Furthermore, the ratio of normal to tangential force above 2.5 has been reported in grinding, and this cannot be explained even when a very high negative rake angle is assumed in the models. These observations suggest there are other mechanisms than just pure cutting involved.

Among the output parameters, the workpiece temperature is probably the most important variable in grinding that should be completely in control. Temperature modeling and problems related to the excessive temperature in the workpiece account a large part of literature in grinding. In general, thermally-induced damages are usually the main concern in finishing of industrial products especially where grinding is used as the final operation. This is mainly due to the high specific energy required to remove the material, most of which is converted to heat [13]. Depending on the wheel-workpiece pair, wheel characteristics and grinding conditions, some portion of the total heat transfers to the workpiece and may cause problems described in detail in [50] including surface burn, phase transformation, softening, residual stresses and cracks.

Different types of thermal models have been developed in the literature to predict the temperature field in the workpiece in order to avoid thermal damages. Analytical temperature models in literature are based on the work of Jaeger [51] and Carslaw and Jaeger [52]. In their book they considered different heat conduction problems and solved those using different methods. The moving heat source was one of the problems Jaeger [51] formulated and solved for various geometrical bodies with different boundary conditions in general cases. Later, different researchers modified the solution and used it in a wide variety of engineering problems such as laser applications [53], machine tools [54], welding [55] and metal cutting [56].

When it comes to the use of moving heat source theory in grinding, several aspects should be taken into account. In this respect, distribution of heat flux along the contact length is one issue that many studies concentrated on. A horizontal uniform distribution has been used in many works. For example, Malkin and Guo used it for simplicity [57], Rowe et al. [58] applied it to drive the proportional energy entering to the workpiece and Des Ruisseaus and Zerkle utilized it to find the workpiece temperature in wet condition [59]. Even though this distribution provided a good approximation for maximum workpiece temperature it failed to predict temperature profile precisely [60]. More accurate heat source models were later employed in which the heat source was proportional to the undeformed chip thickness. Some examples are a triangle heat source [61], [13-15] a circular [62] and elliptical [63] profiles. In some studies, an inverse method was applied to predict the heat flux profile. For example Brosse et al. [64] used an inverse method and showed that a parabolic heat flux profile matches with the workpiece temperature obtained experimentally. Tian et al. [65] did a theoretical study and utilized different heat source profiles including uniform, triangular, trapezoidal, parabolic and elliptic in ultra-precision grinding, and concluded that a triangle heat source predicted a higher temperature distribution than others. While horizontal moving heat source profiles provide a good approximation in fine grinding, different oblique heat source profiles which have an angle with feed direction are more efficient and accurate in deep-cut grinding applications such as creep feed grinding or high efficiency deep grinding (HEDG). In these cases, the depth of cut can reach to an order of millimeter [66] where in shallow-cut grinding a few microns are usually removed. The effect of high depth of cut was taken into account by considering an oblique plane heat source [66]. The result of using a uniform [66] and triangle profiles [67] in an oblique heat source implied that the oblique angle of the heat source plays a crucial effect in prediction of the workpiece temperature accurately. Authors in [68] reviewed heat source profiles used in the literature and concluded that the contact angle and Peclet number were two influential factors which should be considered to define a proper heat source profile in various grinding processes.

Another important issue which gathered much attention in literature was the heat partition ratio, which is the portion of the total generated heat transferred to the workpiece during grinding. Generally the total heat dissipated through four sinks i.e. grinding swarf, wheel, coolant and workpiece. In fine grinding a very small percentage of the total heat is dissipated through the chip [69]. Malkin and Guo [57] argued that melting energy of the workpiece material is the limit of the amount of the heat that can be carried away by chip. In real grinding conditions this limit cannot be reached since chips do not glow immediately and at a short period of time after they leave wheel-workpiece interface the peak in the chip temperature occurs due to oxidation reaction on their surface [70]. Experimental studies usually based on temperature matching and inverse heat transfer methods have showed that 60-85% of the total heat is transported to the workpiece in the case of using conventional wheels [71] while this number is reduced to around 20-30% in the case of using superabrasive wheels [72]. This number could reach up to 5% in case of using porous vitrified CBN wheel in wet condition [73]. Analytical approaches to the heat partition ratio solution have been proposed for general case in [58] and for HEDG in [74]. Guo and Malkin [60] claimed that the heat partition ratio varies along the wheel-workpiece contact zone, and proposed a model to calculate the partition ratio depending on the contact length position. In some models, for example in [75] and [76], the effect of using coolant have been included by building a composite wheel model consisting of the grain and fluid filling the pores of the wheel. The most accurate and acceptable heat partition model was proposed by Rowe [77] using grain contact analyses in which the convective effect of fluid was considered locally in the grain-workpiece interface.

Apart from analytical approaches and experimental investigations, numerical methods have also been employed to study the temperature field in the workpiece [78]. Putz et al. [79] used the FEM approach to analyze thermal behavior of the workpiece in cut-off grinding processes and concluded that it is possible to control the temperature distribution of the workpiece by optimization of cutting parameters and using CBN wheels. Jiang et al. [80] took the micro interaction of grits with the workpiece into account and developed a two dimensional FE model to predict the temperature distribution of the workpiece by using a quadratic curve shape for the heat flux. Wang et al. [81] used meshless finite block method to predict the temperature field in the workpiece and concluded that the method had better convergence compared to the FEM method. Furthermore, they compared 6 different types of heat flux sources and showed that a triangular distribution of the heat source had the best correlation with the experimental results. Mohamed et al. [82] developed an empirical approach to predict the grain radius parameter used in Rowe's heat partition model by correlating the workpiece surface roughness with the maximum grinding temperature. While most of the analytical approaches used two-dimensional analyses, FE methods were developed to solve the problem in three dimensions [83]. However, FE methods required long computational time making them difficult to use in practical applications [84].

Developments in thermal modeling took place by considering the temperature pulse coming from each single grit interaction with the workpiece. The method developed by Li and Axinte [85] provided highly-localized thermal information of the workpiece and a 3D temperature map can be obtained based on the input parameters. They showed that detailed information of temperature even in localized grit-workpiece interaction could be used to design textured or engineering abrasive tools [86].

Surface integrity is highly important in the grinding process. Prevention of the surface burn, as one of the thermal damages occurring in abrasive processes, is the main concern in many grinding applications. Despite excessive studies, its definition, however, is sometimes confusing and in many cases has been linked to a kind of metallurgical transformation causing a specific thermal damage in the workpiece surface. In some references it was related to the tempering or softening process [87] by defining the occurrence of the surface burn when the maximum workpiece temperature rises above the tempering temperature. This kind of workpiece burn was classified as the ''temper burn'' [50]. The workpiece burning temperature around 450 ºC was reported and characterized without exhibition of any visible color change on the AISI 52100 steel workpiece surface [48,99]. However, the tempering process in which steels are heated for a specified time is carried out in a wide range of temperatures (175 ºC-705 ºC) below austenite temperature[89]. As a result, in theory and application, there is not a precise tempering temperature that could be referred to as the threshold for burn occurrence. In case of grinding of hardened steels when the maximum workpiece temperature rises above the austenite formation temperature (around 723 ºC) rehardening was reported in the subsurface of the workpiece material along with a softened tempered zone beneath the hardened layer [90]. This metallurgical transformation was reported as a visible burn or ''re-hardening burn''[57] as another form of the surface burn. The above definitions are applicable for ferrous metals, while the surface burn has been reported in grinding of other metallic materials too [2]. In a broader category, any metallurgical damage including untempered or overtempered martensite, decarburization, oxidation and micro cracks caused as a result of the high temperature of the workpiece surface referred to as the surface burn in grinding [23]. Surface burn in a more precise definition can be directly related to the formation of the oxide layer in the workpiece material [57]. Oxidization of the workpiece surface as a chemical reaction between oxygen and the metal in the heat-affected zone (HAZ) in grinding is the common phenomenon in all forms of the burn occurring in different metallic workpieces. Authors in [91] studied the surface burn of Titanium alloys and confirmed the existence of titanium oxide and titanium carbide in the burn layer. In another study, EDX analysis of Inconel 718 as the grinding workpiece proved the formation of nickel oxide in the burn layer [92]. Yet, no burn model based on metal oxidation theory has been developed in the literature.

Experimental studies related the surface burn with the excessive workpiece temperature and different burn thresholds were reported mostly for ferrous metals in the literature. Burn threshold for cast iron was defined as 150 ^{o}C in high-efficiency deep grinding [93]. In another study, the burn threshold was obtained as 600 ^{o}C for rail steel even though at temperatures between 471^{o}C and 600 ^{o}C softening was also reported [94]. Jianshe et.al. [95] built a graphite-penetrated wheel to make a natural thermocouple between workpiece material and the wheel in order to monitor the workpiece temperature in process. They used a predefined threshold temperature equal to 635 ^{o}C for GCr15 bearing steel in their experiments. Temper colors due to the formation of a thin film oxide for a wide range of ferrous metals occurred between 450^{o} C to 500^{o} C as reported in [96]. Rowe et al. [97] developed a thermal model to predict the workpiece temperature and reported the surface burn for 1055 steel at 330 ^{o} C.

While experimental approach provided valuable data for monitoring [96-97] and detection of the burn[100], the number of theoretical studies on burn prediction is limited. In case of theoretical studies, generally a thermal model is developed to predict the workpiece temperature and a critical temperature is assigned as a threshold for burn occurrence. Using a thermal model Malkin [2] developed a burn threshold diagram in which critical burn temperature around 723 ^{o}C was considered for a variety of steel workpieces. Ali and Zhang [101] developed a fuzzy model to predict the surface burn applicable for different steel workpieces and aluminum oxide wheels. They assumed eutectoid temperature (725 ^{o}C) as the critical temperature in their model. Authors in

[102] developed a model in which the average coefficient of friction and depth of cut were monitored and correlated to the surface burn in robotic disc grinding under controlled force condition. In another study [103] a predefined threshold temperature equal to 550 ^{0}C was assigned as the threshold to determine feed increments in crankshaft grinding.

Based on what has been discussed above it can be concluded that the grinding process modeling has gained a lot of attention so far and different aspects of the process mostly kinematic and mechanics of the process and process temperature have been studied to understand and predict the workpiece surface quality, grinding force and workpiece temperature. Empirical, semi-analytical and FEM models were used to model the mentioned aspects of the process. Thermally-induced damages due to excessive temperature produced during the process have been mostly studied experimentally too.

1.2 Objective

As mentioned earlier, grinding models play an important role in terms of proper grinding conditions selection and improvement of the grinding efficiency. As reviewed in the introduction part, many grinding models have been developed by researchers to shed more light in the process. However, most models are empirical or mechanistic that need some calibrations. FEM models are not fast and analytical models have some limitations such as simplification assumptions. To be more percise, in kinematic-geometrical models unrealistic assumptions and neglecting some parameters made them unable to use in the industry. Wheel eccentricity is also an important issue that has been neglected in most models. Even though the grinding wheel should be mounted and dressed properly to eliminate any source of any unbalances, a small amount of wheel run out can have great effects on workpiece roughness and the grinding force. Wheel run out cannot be eliminated in some cases, for example single layer electroplated wheels in which a layer of CBN or diamond particles are located on the surface of the wheel cannot be dressed. Another common assumption in wheel modeling is considering a normal distribution of the grit properties representing the stochastic nature of the grinding wheel. However, this distribution can change as the wheel wears during the process. Moreover, in the previous studies, it was incorrectly assumed that any grit-workpiece interaction resulted in workpiece surface updating like a milling tool. In other words, grits with rubbing and ploughing action also removed material from the workpiece. However, dynamics of milling could not be directly utilized to describe the grinding process. Due to bigger undeformed chip thickness and better tool geometry condition in milling, rubbing and ploughing are negligible compared to the grinding process in which many grits may only create rubbing or ploughing action. Likewise, effects of the active number of grits on the process such as surface roughness, maximum chip thickness and forces have not been truly investigated and there was either none or incomplete validation of the active number of grits in the current models.

Regarding the force models in the grinding, in spite of a wide variety of grinding force models, there is no comprehensive model considering the metal cutting mechanics principles based on proper geometrical-kinematic interactions which could be used for industrial applications. In other words, the physical effect of a high negative rake angle i.e. the formation of the dead metal zone has not been included in the models and there is no analytical force model to predict the ploughing force based on the metal cutting mechanics.

Regarding the temperature models, based on what was discussed earlier, most of the analytical models developed so far are two-dimensional and the temperature field was calculated in macro-scale level where the wheel-workpiece interaction was considered as the source of the heat. As a result, a constant average value of the grinding force is used to calculate the power and heat flux. However, the grinding force is the result of active grit interaction with the workpiece causing intermittent force pulse similar to that of milling processes [17]. There are even some cases where the grinding force fluctuates between zero and its maximum value as a result of wheel vibration coming from run out or the grinding force itself. Other important cases are slotted, segmented and engineered wheels where the grits are positioned precisely on the wheel with a pattern. In all above cases the grinding force fluctuates with different frequencies depending on the situation. Accordingly, the heat source in grinding is a function of both time and position. Apart from the heat source distribution, boundary conditions especially in wet grinding in analytical models have not been fully considered i.e. the heat convection from the side walls has been neglected.

This thesis aims to develop grinding models considering the mentioned factors into account. To be more precise, a deterministic method has been proposed for identification of the active number of grits by developing kinematic equations considering practical conditions applied on the process such as wheel wear and wheel eccentricity. Using this approach, an analytical thermo-mechanical force model has been developed, whereby contributions of ploughing, shearing and the formation of the dead metal zone are identified. Furthermore, an analytical 3D temperature model with a time dependent heat source which considers more realistic boundary conditions in wet and dry grinding has been proposed which is able to provide detailed information of the temperature distribution in the workpiece analytically without much computational time and effort compared to FEM solutions. The maximum temperature of the workpiece can be predicted analytically and process parameters and grinding conditions can be evaluated to achieve maximum productivity (MRR) without causing any thermal damage to the parts. The temperature profile of the workpiece may be obtained from the model and be used in CCT (Continuous Cooling Transformation) and TTT (Time-Temperature-Transformation) diagrams to observe any microstructure change, phase transformation or surface burn in the workpiece. Using the proposed temperature model the occurrence of the burn can be predicted and in case of workpiece surface burn, the burn layer thickness is predicted.

1.3 Layout of the Thesis

The thesis is organized in 8 chapters as follow:

In chapter 2 a kinematic-geometrical model for surface grinding is provided. The model uses the statistical properties of the grits on the wheel and the effect of wear has been included in the model. The kinematic equations are developed by calculating the grit trajectory while some practical conditions such as wheel eccentricity are taken into account.

In Chapter 3 a force model is proposed by using the kinematic equations developed in the previous chapter. The true physical mechanisms of chip removal are considered in the model. The force model in grinding is based on the thermomechanical force model developed by Ozlu et al. [104]. The effect of dead metal zone due to high negative rake angle and ploughing is considered in the model.

In chapter 4 the temperature model is developed. The effects of different boundary conditions in dry and wet conditions for a slab workpiece are discussed. Furthermore, the concept of time dependent heat source due to intermittent nature of the grinding force is introduced and applied in the model.

In Chapter 5 an important thermally-induced damage namely surface burn has been studied. Its important and the conditions in which different workpiece material may experience the surface burn are discussed.. The effective parameters on the surface burn are discussed analytically. Based on the theory of metal oxidation in high temperature a burn model is proposed to predict the occurrence and the quality of the surface burn.

In Chapter 6 the experimental setup for the proposed models is explained. The surface roughness of the workpiece, grinding force and workpiece temperature are measured experimentally and compared with the model predictions.

The effects of related parameters and the results are discussed in chapter 7. A detailed discussion on the behavior of the output parameters namely surface roughness, force and temperature is provided. Furthermore, the experimental results of excessive workpiece temperature is discussed and compared with the burn model.

Finally, the conclusions drawn from this thesis and suggestions for future investigations are presented in chapter 8.

2 KINEMATIC-GEOMETRICAL MODEL

As the grinding wheel rotates, some of the grits interact with the workpiece. Due to stochastic nature of the grinding wheel, derivation of grit trajectory equations is not as simple and straight forward as in milling or turning. The first step of force or temperature modeling is developing the kinematic equations of grit-workpiece. This chapter presents this equation and the concept of active number of grits is discussed. The output of the kinematic-geometrical model is identification of the active number of grit and intentions and maximum undeformed chip thickness which will be used in the force and temperature model.

2.1 Wheel Modeling

A grinding wheel consists of a number of abrasive grits, each of which has its own geometrical characteristics which are randomly distributed. Figure 2-1 shows a SEM photo of a CBN single-layer grinding wheel. As it can be seen, the grits are randomly distributed; have a different geometry and orientation. The size and the height of the grits are not uniform either.

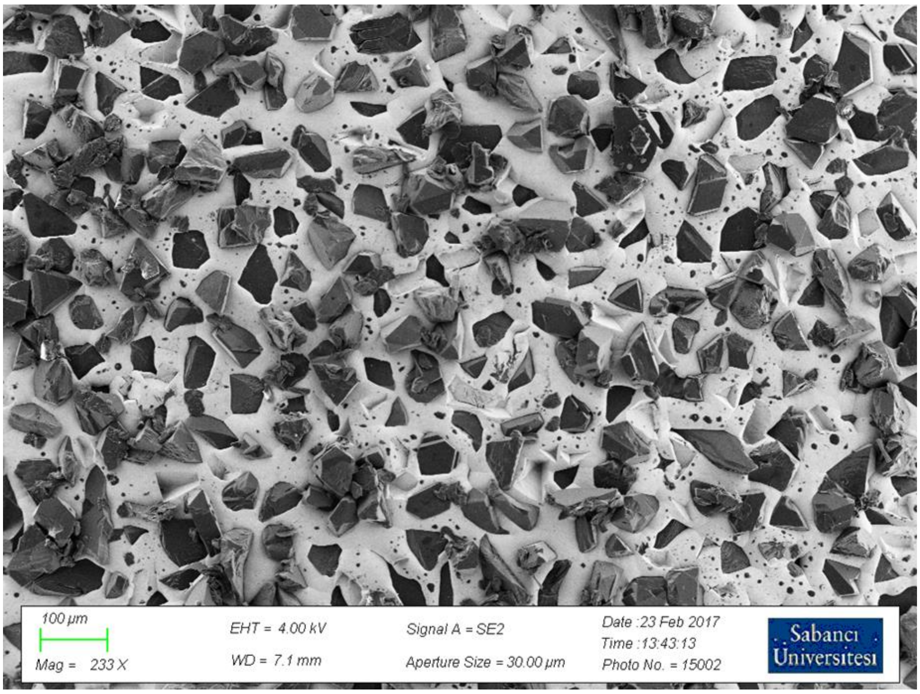

Figure 2-1 SEM photo of an electroplated CBN grinding wheel

Regarding the stochastic nature of the grinding wheel, some assumptions must be considered. In this thesis, the grinding wheel is discretized into elements along the axial direction. Each element is concentric and resembles a ring surrounding the circumference of the wheel. Figure 2-2 shows discretization of the wheel along the axial direction. Based on the Figure the width of each element has a value of the width of cutting edge,w_c which is equal to some portion of the grit's width, w_g. The grit height, H, and width of cut (w_c) are two parameters that are randomly distributed in derivation of the kinematic equations.

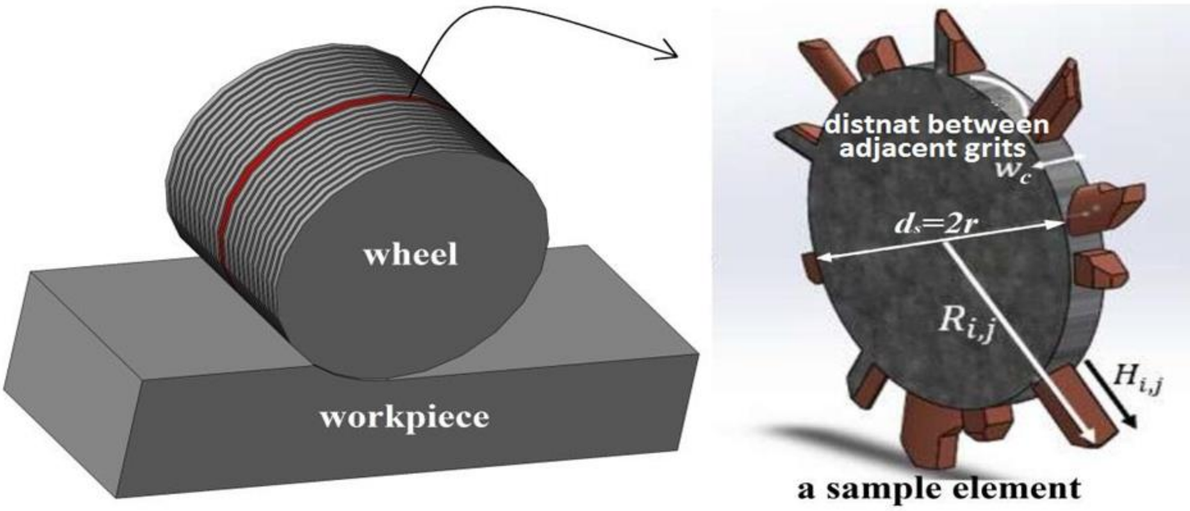

Figure 2-2 Discretization of grinding wheel along the radial direction

The real photo of the CBN wheel is shown again in figure 2-3 showing a sample element. The red band in this figure is a typical element that has been marked in Figure 2-2 with a red color and the green lines show the distance between two adjacent grits. In reality, because of the random distribution of the grits, the distances between each of the two grits in an element are not the same (see green lines in Figure 2-3). However, considering an average value of the distance between two adjacent grits provides a good approximation making the model easy for computer code generation. This is because of this fact that it eliminates the need to build extra functions and operations to generate the position of the grits. It can be assumed that a very small variation of the distance between two adjacent grits does not affect the accuracy of the model since it will be shown later that only a few grits are active and the important parameter here is the distance between two active grits.

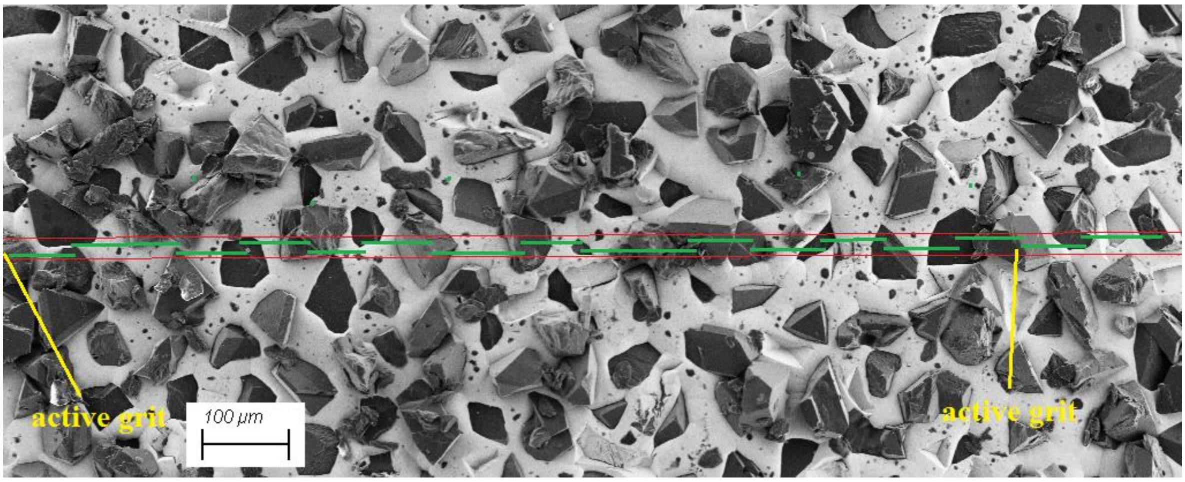

Figure 2-3 sample wheel discritization on asingle layer CBN wheel

Each of the cutting edges has its own height. Considering having a maximum run out equal to R_o the dynamic radius of i^{th} grit in j^{th} element, $R_{i,j}$ can be modeled as:

$$R_{i,j} = r + H_{i,j} + R_o.\sin\ ((i-1).2\pi/N) \qquad (2-1)$$

where r is the nominal radius of the wheel, $H_{i,j}$ is the height of i^{th} grit in j^{th} element and N is the total number of grits in each element which can be obtained as:

$$N = \pi.d_s.w_g.C \qquad (2-2)$$

where d_s is the nominal diameter of the wheel, $w_g$is the average grit width and C is the static number of cutting points which is the total number of grits in 1 mm^2 area. As it can be deduced from Equation 1, wheel run out changes the height distribution of the grits and the topmost grits may not necessarily have interaction with the workpiece as it claimed in [4].

2.2 Grit Trajectory

The path of the grits is obtained by superimposition of the rotational movement of the wheel, its linear reciprocal movement due to run out parallel and perpendicular to the feed direction, vibration due to wheel-workpiece interaction and linear movement of the workpiece in feed direction (Figure 2-4). The x and z coordinate of the trajectory of each cutting edge can be given as:

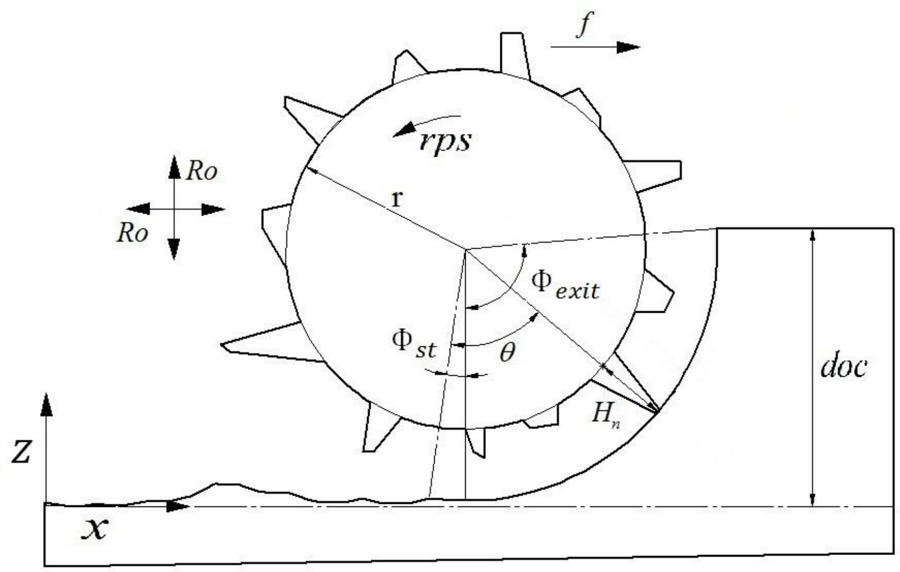

Figure 2-4 Schematic of wheel-workpiece interaction in surface grinding

$$x_{i,j} = \left[R_{i,j} + R_o.\sin\left(\frac{\theta_{i,j}}{2}\right)\ \right]\sin(\theta_{i,j}) + \ f.t \qquad (2-4)$$

$$z_{i,j} = \left[R_{i,j} + R_o.\sin\left(\frac{\theta_{i,j}}{2}\right)\right](1-\cos(\theta_{i,j})) \qquad (2-5)$$

where f is feed in mm/sec, $\theta_{i,j}$ is immersion angle of i^{th} grit in j^{th} element varying from $\emptyset_{st}$to $\emptyset_{exit}$, and t is time which can be calculated as:

$$t = \frac{\theta_{i,j}}{\omega} + \frac{(i-1)}{N.\omega} \qquad (2-6)$$

where ω is wheel rotational speed in terms of revolution per second and i varies from 1 to N.

When a particular grit trajectory has an intersection with the workpiece surface, that grit is considered as an active one. Therefore, the active number of grits does not only depend on the wheel properties, but it is also affected by cutting parameters such as feed rate and depth of cut as well as wheel vibrations. Once the grits' trajectory is identified, instantaneous chip thickness for each grit can be calculated for the active ones. Having grits with different heights is analogous to run out on milling cutter teeth. Instantaneous chip thickness calculation for a milling tool with run out is given in [105]. Figure 2-5 shows the situation in the grinding. Based on the figure the instantaneous chip thickness is obtained as follow:

$$h_{i,j}(\theta_{i,j}) = R_{n,j} - R_{m,j} + (n-m).f_t \sin(\theta_{i,j}) \qquad \emptyset_{st} < \theta_{i,j} < \emptyset_{exit} \qquad (2-7)$$

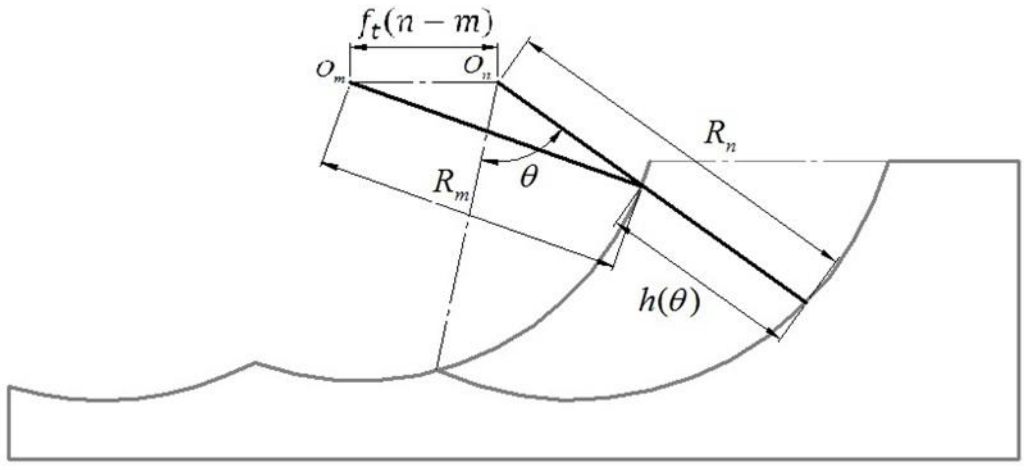

Figure 2-5 Instantaneous chip thickness in grinding

where $R_{n,j}$ and $R_{m,j}$ are the radius of n^{th} and m^{th} grit (two consecutive active grit) in the j^{th} element, f_t is feed per grit (mm/rev-grit). $\emptyset_{st}$ and $\emptyset_{exit}$ are calculated as:

$$\emptyset_{st} = sin^{-1}\left(\frac{R_{m,j}-R_{n,j}}{(n-m)f_t}\right) \qquad (2-8)$$

$$\emptyset_{exit} = cos^{-1}\left(1 - \frac{doc-R_{max}+R_{n,j}}{R_{n,j}}\right) \qquad (2-9)$$

where doc is depth of cut and other parameters have been defined before.

2.3 Workpiece Surface Generation

By knowing the grit's trajectory the workpiece surface topography can be generated. As it was shown in previous sections, due to grit height variations not all of the grits on the wheel have interaction with the workpiece. Depending on the grit height distributions, only a few percentages of the total number of grits are active. However, not all the active grits' interaction with the workpiece results in material removal from the workpiece surface. It is possible that some of the active grits barely touch the surface and produce a rubbing force which resulted in elastic deformation on the workpiece surface. Some of them may produce a ploughing force where there is plastic deformation without chip formation. For a specific active grit when the undeformed chip thickness reaches a value known as critical chip thickness, the material removal from the workpiece surface starts. Calculation of the ploughing force will be discussed in the next chapter. However, the critical chip thickness is required to be used for workpiece ground surface generation. Figure 2-6 shows a schematic view of a grit tip.

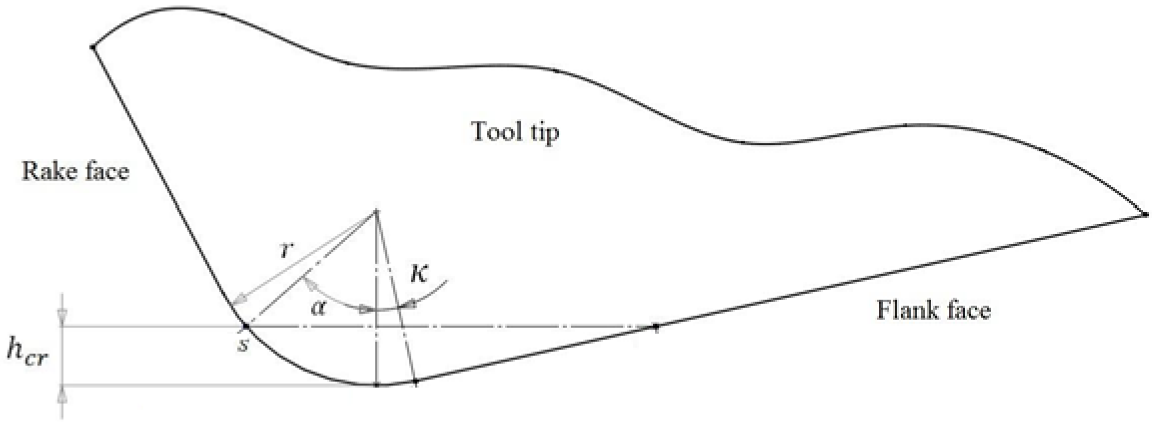

Figure 2-6 Tool tip considering edge radius in the third deformation zone

When the chip thicness is below the critical chip thickness, chip will not form and the tool-material interaction will be in the form of ploughing. The workpiece material is pressured to the downside and there will be no material removal from the workpiece surface. Considering full elastic recovery assumption [106] the critical chip thickness depends on the stagnation point, edge radius of the grit and the rake angle. Stagnation angle separates the second deformation zone from the third deformation zone. The authors in [106] measured the stagnation angle and concluded that it is in the range of 44-63^0. Other experimental works such as [107] also reported the similar values. In general, an average of 55^0 could be a good approximation in most cases. Thus, in this study, the stagnation angle is taken as 55^0. The critical undeformed chip thickness is calculated as [106]:

$$h_{cr} = r_t.[1 - \cos(\alpha)] \qquad (2-10)$$

where α is stagnation angle, r_t is edge radius of the grit and α is the rake angle.

Equation 2-10 is used as the criterion to update the path generated by active grits. In grinding similar to milling, chip thickness varies from zero to its maximum value depending on each grit height. If the maximum chip thickness created by a particular grit is less than the critical chip thickness and the workpiece surface is not updated then the grit is considered as an active one with ploughing effect.

In order to obtain the surface profile of the workpiece perpendicular to the cutting speed direction, the cross-sectional shape of the active grits should also be known. Malkin and Guo [13] reviewed numerous techniques including profilometry, imprint and scratch methods and concluded that the scratch method provides the most detailed and accurate picture of the cross-sectional shape of the cutting point. The cross section of the grit must be known and considered in the kinematic-geometrical model to simulate the workpiece surface topography. The grit trajectory equations obtained in section 2-2 are a 2D path of single point on the grit. The cross-sectional shape of the grit is assigned to this path to represent the geometrical part of the model. Based on various experimental works, a trapezoidal cross-sectional shape with the base width of 2 μm and the semi-included angle of 60^0 were obtained as the average values and used in this thesis to calculate the surface roughness perpendicular to the cutting speed direction.

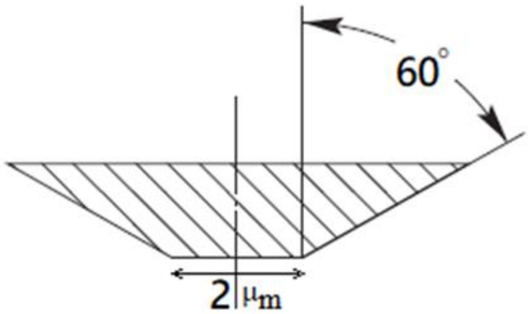

Figure 2-7 Cross-section of the grit with average parametric values

The topography of the generated workpiece surface is simulated through a MATLAB code which simulates surface finish parallel and perpendicular directions to cutting.

The trajectories of the grits are calculated based on equations 2-4 and 2-5 and the ground workpiece surface is generated considering the critical chip thickness as well. Grit properties and grinding conditions are the main inputs of the model. Grit height distribution, cutting angles, size and edge radius are all influential parameters that should be known or measured beforehand. The measurement results are discussed in detail in chapter 5. Figure 2-7 shows the algorithm used for the surface simulations.

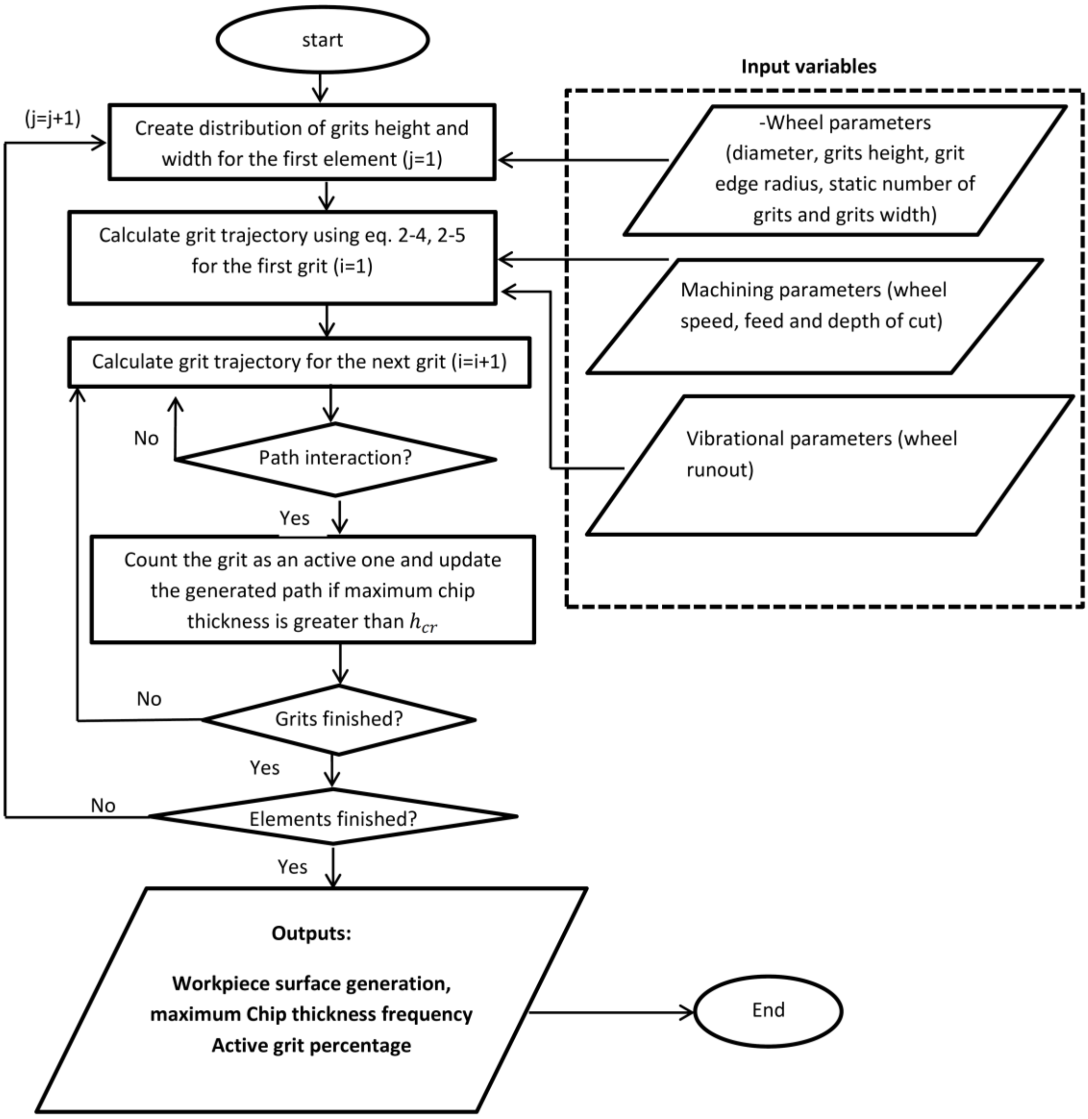

Figure 2-8 Algorithm of simulation code for workpiece surface generation

As it is shown in Figure 2.7, grit properties, grinding conditions and wheel run out are the input parameters. Active number of grits, chip thickness frequency and workpiece surface topography are the outputs of the simulations. Chip thickness frequency is a term is used in this thesis to indicate the fact that each active grit generates a different chip thickness. In other words, instead of a constant maximum chip thickness there is a spectrum of maximum chip thickness. There are three fundamental properties of grits i.e. height, width of cut (w_c) and C number (number of grits in unit area) that are measured and a specific grit height distribution based on the wheel conditions (whether the wheel is new, worn or trued) is developed. The simulation starts for the first radial element. The width of each element is equal to width of cut (w_c) which is produced by *normrnd* function in MATLAB. This function produced a normal random data based on the mean and standard deviation values calculated from experimental measurement. Equations 2-1 to 2-10 are used to create a trajectory for each grit in the first element. Active grits are identified by checking whether there is an intersection between the current grit trajectory and the previous active one. By finding the intersection point the workpiece surface is updated. When the maximum chip thickness of a particular grit is less than the critical value (h_{cr}), the surface point is updated and that grit is counted as an active one with only the ploughing effect. The simulation continues by repetition of the same approach for the next element, having a new width of cut and new grit heights until the last element.

In the end, the model computes the profile of the generated surface by calculating the active number of grits and corresponding values of chip thickness. As a result, instead of having a constant chip thickness, each active grit has a different chip thickness. Having all values of maximum chip thickness provides construction of a frequency distribution of maximum chip thickness values which is referred to maximum undeformed chip thickness frequency in this thesis. Having the maximum chip thickness frequency provides a wise evaluation of the input grinding parameters. As an example of force analysis, if a large number of grits had a maximum chip thickness less than the critical undeformed chip thickness, the ploughing force would account for the greater portion of the total force which in turn would result in increasing specific energy. On the other hand, if a large number of grits had a very high maximum chip thickness, it would cause rapid wheel wear causing grit pullout or grit macro fracture. Figure 2-8 and 2-9 shows a sample of the output results. In figure 2-8 the grit trajectory is shown and in figure 2-9 corresponding maximum chip thickness frequency is illustrated.

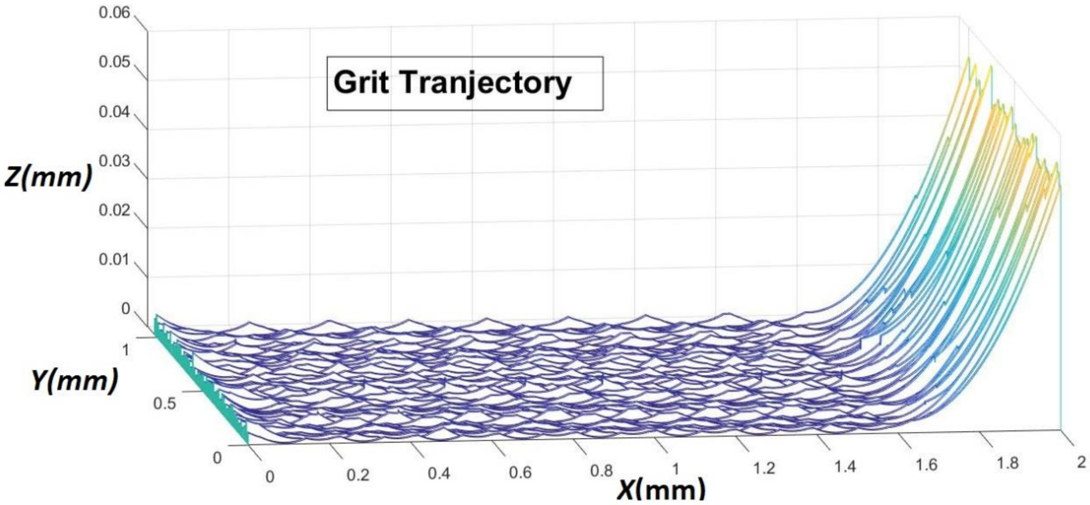

Figure 2-9 Grit trajectory) at feed 0.25 mm/rev, depth of cut 0.08 mm

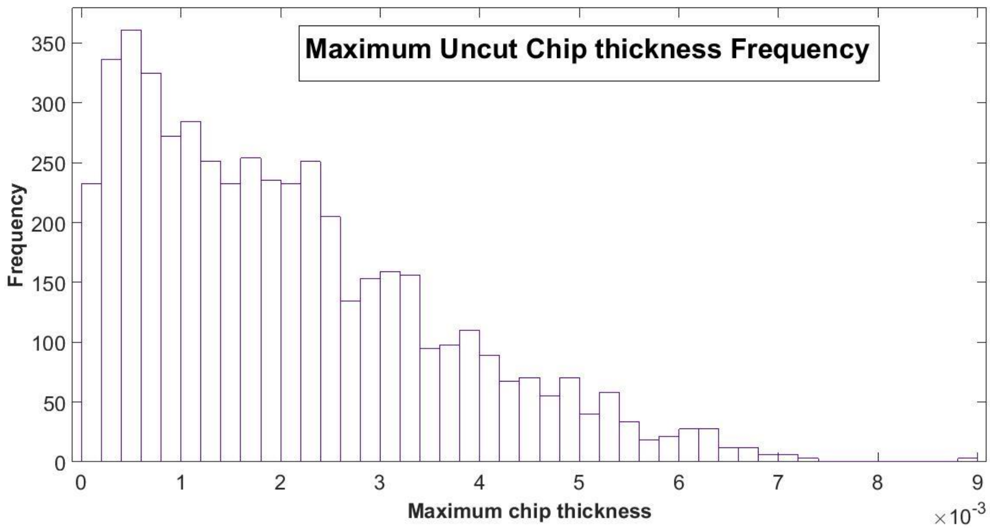

Figure 2-10 chip thickness frequency at feed 0.25 mm/rev, depth of cut 0.08 mm

3 FORCE MODEL

Grinding force is an important parameter that affects the productivity and quality of industrial products. The very high negative rake angles of the grits play an important role in the material removal mechanism resulting in the formation of a stagnant area ahead of the grits called the dead metal zone (DMZ). In addition, as it was discussed in the previous chapter, ploughing force also comes into effect when the undeformed chip thickness is comparable with the cutting edge radius of the active grits. Based on these facts, in this chapter, a new model is proposed to predict the grinding forces and understand the material removal mechanism. This is achieved by modeling the grit-workpiece micro-interaction and geometry of the grinding wheel, enabling the engaged grits and undeformed chip thickness to be defined. An analytical kinematic-geometrical force model considering dead metal zone and ploughing, as well as practical conditions such as run out and wheel wear has been developed. The input parameters of the model are grinding conditions, workpiece material and wheel properties, and sliding coefficient of friction between wheel-workpiece pair. Based on the proposed model, the grinding force is composed of three portions including ploughing, cutting and formation of DMZ. The influential parameters on each force portion are analyzed. Considering the physical mechanisms involved in the grinding process, the model provides more in-depth knowledge about the grinding forces which can be used for finding the optimum conditions. This model is also able to explain some inherent characteristics of grinding forces such as the high ratio of normal to tangential force and high specific grinding energy in low feed rates and depth of cuts.

In the present model, it is assumed that the material removal is done through chip formation and shearing process. Because of the edge radius of the grits, edge or ploughing forces exist and can account for a considerable portion of the total grinding force if the undeformed chip thickness is comparable with the critical value. Furthermore, a stagnant region called the dead metal zone (DMZ) is formed ahead of the tip of those grits having high negative rake angles when the chip is formed and creates some force as a result of having contact with the workpiece surface. The total force consists of three portions including the ploughing, the formation of DMZ and the cutting. In this chapter, the force equations are derived for each part and the algorithm required to calculate the total grinding force is explained.

3.1 Cutting Force

When the undeformed chip thickness is greater than the critical value, h_{cr} the chip is formed. The cutting force is calculated as the product of the force coefficient and the chip cross-sectional area. This portion of the grinding force calculation is similar to the calculation of the milling force. However, the cross section of the grit, active grits and corresponding undeformed chip thickness should be known before calculation of the cutting force. Accordingly, the output of the kinematic-geometrical model discussed in Chapter 2 is used in this section. As it was discussed earlier the cross section of the grits can be assumed to be triangular shape [13]. Figure 3-1 shows a sample of workpiece surface confirming the triangular cross section assumption.

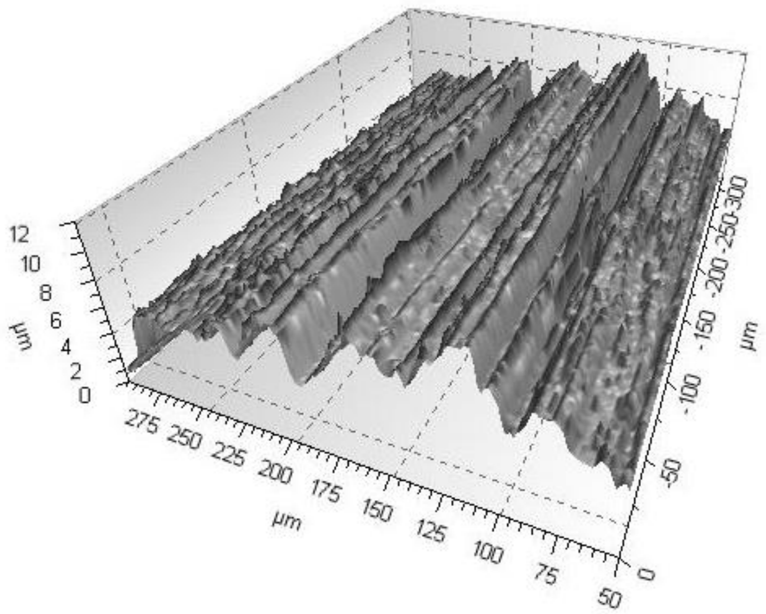

Figure 3-1- surface of the ground surface captured by Nano focus microscope showing the trangular shape of the cross section of the grit.

Figure 3-2 shows a schematic of cutting forces acting on a single grit.

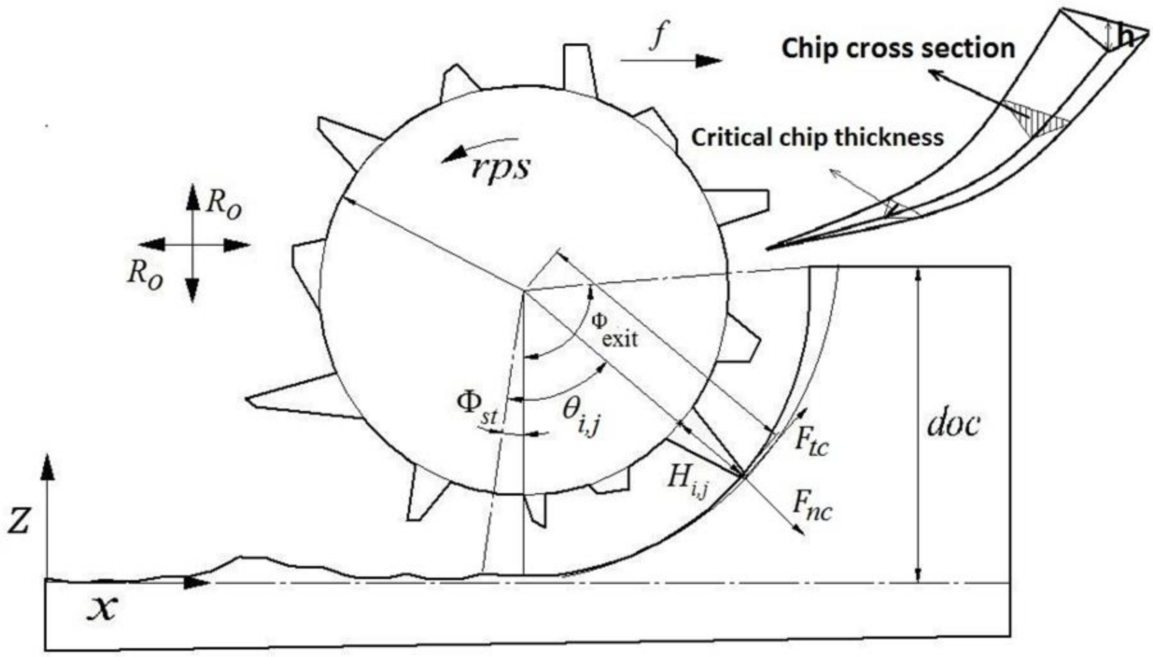

Figure 3-2 cutting force for a single grit

Tangential and normal cutting forces showing in the Figure 3-2 for a single grit are expressed as follows:

$$F_{tc} = A_c.K_{tc} = \frac{1}{2}w_c.K_{tc}.h\left(\theta_{i,j}\right) \tag{3-1}$$

$$F_{nc} = A_c\,K_{nc} = \frac{1}{2}w_c.K_{nc}.h\left(\theta_{i,j}\right) \tag{3-2}$$

Where, A_c is the area of the chip cross section, w_c is the width of cutting edge, $h(\theta_{i,j})$ is the instantaneous chip thickness, K_{tc} and K_{nc} are tangential cutting and feed force coefficients respectively. These coefficients can be obtained analytically considering the oblique cutting theory by the following equations [108]:

$$K_{tc} = \frac{\tau_s}{sinsin\varphi_n}\frac{cos(\beta_n - \alpha_n) + tanitan\eta sin\beta_n}{\sqrt{cos^2(\varphi_n + \beta_n - \alpha_n) + tan^2\eta sin^2\beta_n}} \tag{3-3}$$

$$K_{nc} = \frac{\tau_s}{sin\varphi_n cosi}\frac{sin(\beta_n - \alpha_n)}{\sqrt{cos^2(\varphi_n + \beta_n - \alpha_n) + tan^2\eta sin^2\beta_n}} \tag{3-4}$$

where τ_s is the shear stress, φ_n is the shear angle, β_n is the normal friction angle, α_n is the normal rake angle, η is the chip flow angle and i is the oblique angle. According to Stabler's rule [109] chip flow angle (η) is equal to the oblique angle (i). Oblique and rake angles are obtained experimentally by observation of the grit as it will be explained in experimental section. Ozlu et al. [104] and Budak and Ozlu [110] studied the tool-chip interface analytically by integrating the mechanics of the cutting at the primary and secondary shear zones and developed an analytical thermomechanical model to predict the cutting forces. By knowing the sliding friction coefficient (Coulomb friction) and workpiece material constants, the model is able to predict the frictional and shear angles, tool-chip contact length, shear as well as normal stress distributions along the rake face. This model is used in the current thesis to obtain shear stress; shear and friction angles required obtaining force coefficients analytically (equations 3-3 and 3-4). The detailed procedure is presented in the Appendix.

The cutting force components in the horizontal and vertical directions shown in Figure 3-2 are finally obtained as follows:

$$F_{xc} = -F_t \cos(\theta_{i,j}) - F_n \sin(\theta_{i,j}) \qquad (3-5)$$

$$F_{zc} = F_t \sin(\theta_{i,j}) - F_n \cos(\theta_{i,j}) \qquad (3-6)$$

3.2 Ploughing Force

When the undeformed chip thickness is smaller than the critical value, h_{cr}, the chip does not form, and the material is compressed beneath the machined surface generating edge or ploughing forces [111]. Budak et al. [106] studied the third deformation zone and predicted the ploughing forces using the thermo-mechanical model discussed in the previous section. Their approach is used in this thesis to obtain the ploughing force in grinding.

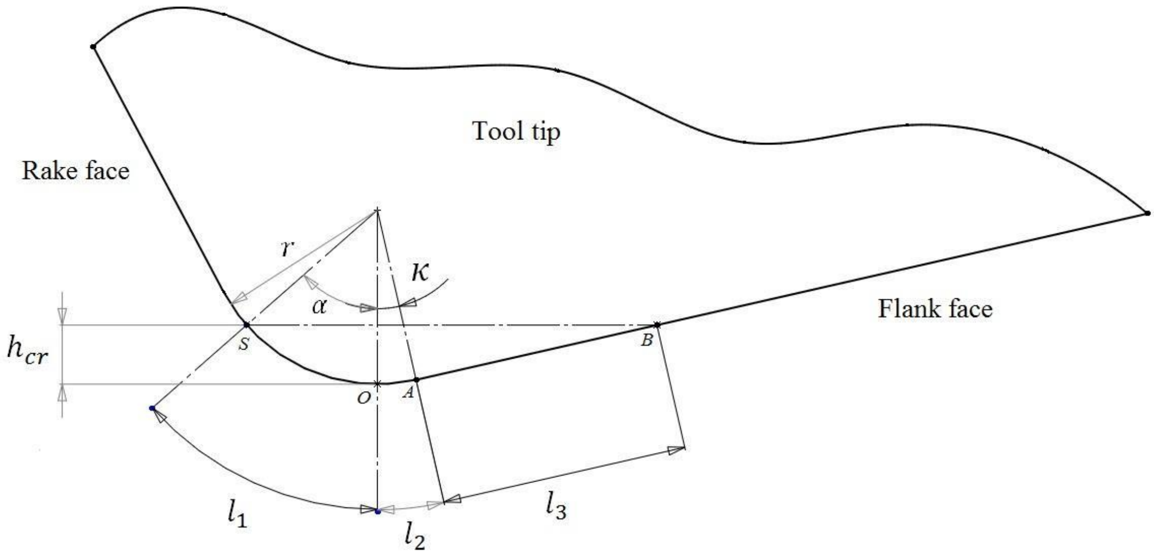

Figure 3-3 grit tip considering edge radius in the third deformation zone

Figure 3-3 shows the schematic view of the grit tip in the grinding.

The total contact length on the flank face, l_f, is measured from the stagnation point to the end of the contact on the flank face. Stagnation point separates the second and third deformations zones. The total length can be divided into three sections as illustrated in the figure and can be obtained from Equation (3-7):

$$l_f = l_1 + l_2 + l_3 \qquad (3-7)$$

where l_1 is part of the grit nose arc starting from the stagnation point (point *S* in Figure 3-3) to the point *O*, the bottom point in the arc and. This length is obtained as follows:

$$l_1 = \alpha . r \qquad (3-8)$$

where α is stagnation angle and *r* is grit edge radius.

l_2 is the rest of the arc length starting from point *O* to Point *A*, i.e. the end point of the arc, and is calculated as:

$$l_2 = \kappa . r \qquad (3-9)$$

where κ is clearance angle.

l_3 is the contact length on the clearance face starting from point *A* to point *B*, end point of grit-workpiece contact, and can be calculated as follows:

$$l_3 = r\frac{cos\kappa - cos\alpha}{sin\kappa} \qquad (3-10)$$

In derivation of the above equation it is assumed the workpiece material is pressured to the downside and recovered elastically completely.

As it was discussed in the previous chapter an average value of 55^0 could be a good approximation for the stagnation angle and will be used in this thesis. The critical chip thickness can be obtained from Figure 3-3 as [106]:

$$h_{cr} = r - r.cos(\alpha) = r.[1 - cos(\alpha)] \qquad (3-11)$$

The normal stress at the stagnation point is P_0 which is known from thermomechanical force model (see appendix); the normal stress profile is modeled as a quadratic equation on the flank face:

$$p(x) = a.x^2 + b.x + c \qquad (3-12)$$

where,

$$a = \frac{P_0}{2.l_f.l_1 - {l_f}^2} \qquad (3-13)$$

$$b = -2.a.l_1 \qquad (3-14)$$

$$c = P_0 \qquad (3-15)$$

The behavior of the normal stress is based on the physics of flank contact where the material is pressed at the stagnation point, and as a result, the normal stress increases continuously through the first region until it reaches its maximum (point *O* in Figure 3-3). After this point, it will diminish gradually and reach zero at the end contact point. This profile is shown in Figure 3-4.

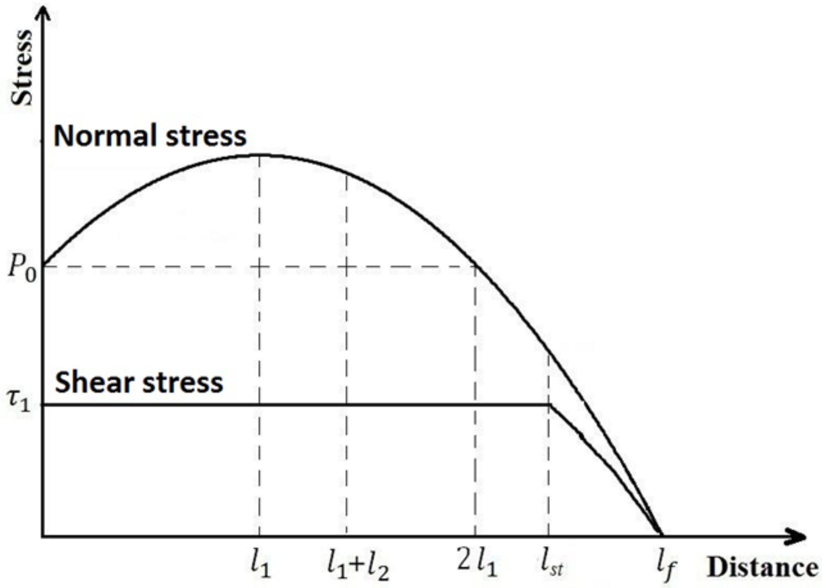

Figure 3-4 Normal and shear stress profiles on the flank face

The friction condition at the flank face is assumed to be sticking and sliding according to the following equation:

$$\begin{cases} \tau = \tau_1 & 0 \le x \le l_{st} \\ \tau = \mu P(x) & l_{st} \le x \le l_f \end{cases} \qquad (3-16)$$

The length of the sticking part is calculated by comparing $P(x)$ with τ_1. At points where $\mu P(x)$ is bigger than τ_1, the sticking condition exists, while for the rest of the contact length sliding occurs [104].

The normal force generated on the contact face is calculated based on the normal stress distributions on the flank face as:

$$F_{Ni} = -\int_{l_i}^{l_i+l_{i+1}} w_c.p(x).O(x)dx \qquad (3-17)$$

where l_i is the length of the regions, w_c is the width of cutting edge, $O(x)$ is the orientation function for the regions.

Based on the sticking or sliding conditions, the friction force is calculated as follows respectively:

$$F_{Fi} = \int_{l_i}^{l_i+l_{i+1}} w_c.\tau_1.O(x)dx \qquad (3-18)$$

where τ_1 is the shear stress at the exit of the shear plane and is obtained from the thermomechanical force model.

$$F_{Fi} = \int_{l_i}^{l_i+l_{i+1}} w_c.\mu.p(x).O(x)dx \qquad (3-19)$$

where μ is the sliding friction coefficient. The total ploughing forces in horizontal and vertical directions for a single grit are calculated as:

$$\begin{cases} F_{px} = \sum_{i=1}^{3} F_{Nix} + F_{Fix} \\ F_{pz} = \sum_{i=1}^{3} F_{Niz} + F_{Fiz} \end{cases} \qquad (3-20)$$

Regarding using the above ploughing force model in the grinding process, some critical issues should be considered. The edge radius of the grits is varied depending on the condition of the grits. Figure 3-5 shows some SEM photos of grits for a single layer CBN wheel. Generally, a fresh CBN grit has a very sharp edge and the edge radius could reach less than 1 μm (Figure 3-5 a). After some grinding passes, the grits lose their sharpness and will be dull due to micro fracture (Figure 3-5 b) and the effective edge radius is increased. A large portion of the tip may also be lost due to high force (macro fracture) and may decrease the clearance angle (Figure 3-5 c). The grit-workpiece contact area is also affected by the clearance angle in the model. Some grits have a flat surface area (Figure 3-5 d) or they will be flat (zero clearance angle) due to the attritious wear mechanism [13]. Setting the clearance angle as zero in Equation (3-10) makes l_3 approach infinity. In such a case, l_3 in equation (3-10) must be replaced by the length of the flat area. According to what has been discussed, knowing the proper geometrical properties of the grit is an important input parameter that affects the grinding force profoundly. The experimental procedure to obtain the geometrical properties of the grits required in the model is explained in detail in chapter 5. Even though modeling of different mechanisms of wear is not in the scope of this thesis the effect of worn wheel on the output parameters including the force model is considered in the model. For example, in case of attritous and pull out wear the average clearance angle and the number of grit in unit area of the grit tends to be decreased respectively. In case of micro and macro fracture, the grit edge radii and rake angle are changed. This characteristics of grit are measured by a microscope as it will be explained in details in Chapter 6.

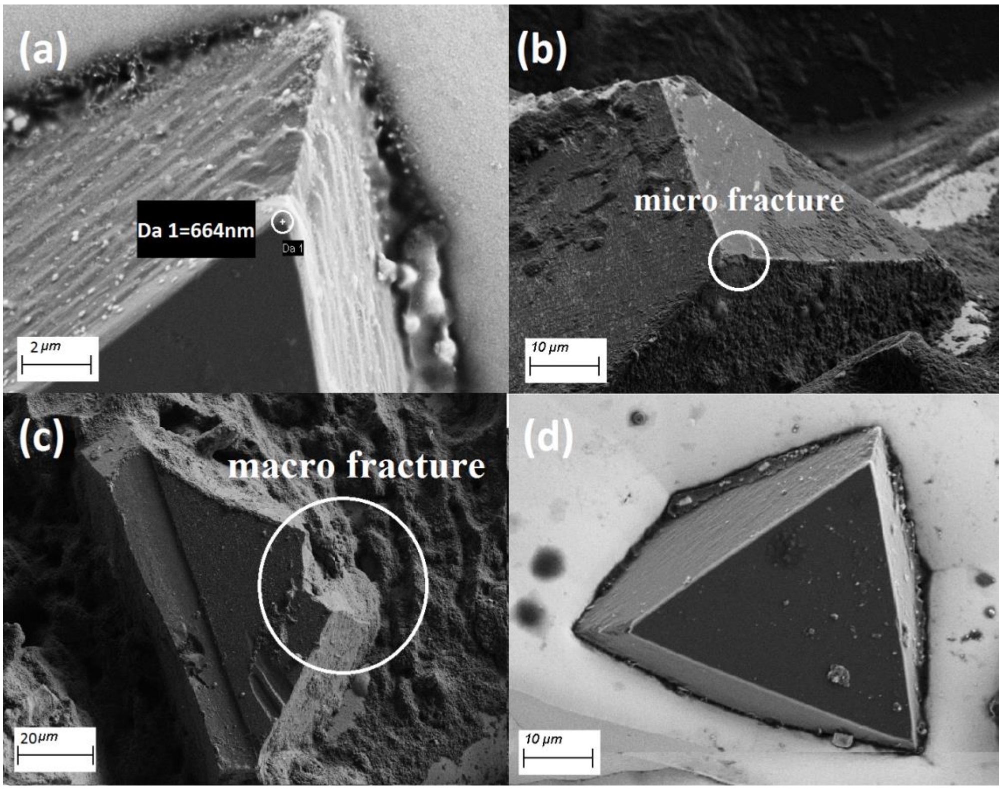

Figure 3-5 SEM photos of single CBN grits, a) a sharp grit with edge radii of 0.6 μm, b) fracture wear at the tip, c) fracture wear changing the clearance angle, d) grit with a flat surface

3.3 Formation of Dead Metal Zone

The Dead metal zone is a stagnant region which could be represented by a triangle area formed ahead of the tool having a very high negative rake angle. Direct evidence of formation of the dead metal zone in grinding is almost impossible to achieve experimentally. There are thousands of grits on a grinding wheel and only a small percentage of them are active, making it hard to identify them during or after the grinding experiment. Furthermore, the dead metal zone will form only in certain circumstances and not for all of the active grits removing the workpiece material will be accompanied by the formation of a DMZ. In spite of these difficulties, the results of the quick-stop test using a single grit grinding wheel clearly confirmed the existence and properties of a DMZ. In their study, Kita et al. [44] used the quick-stop technique to stop the material removal process at normal grinding speed using different conical grits made out of cemented carbide, diamond and aluminum oxide with rake angles varied between -50^0 to -80^0. The results indicated the existence of a DMZ ahead of the grits which varied during the cutting process and could affect the formation of chips. Lortz [45] studied cutting mechanisms in grinding using the slip-line field assuming a spherical cutting edge and confirmed the formation of the dead zone by observing a cross section of the chip-formation zone in grinding. Figure 3-6 shows a schematic model of the existence of this region.

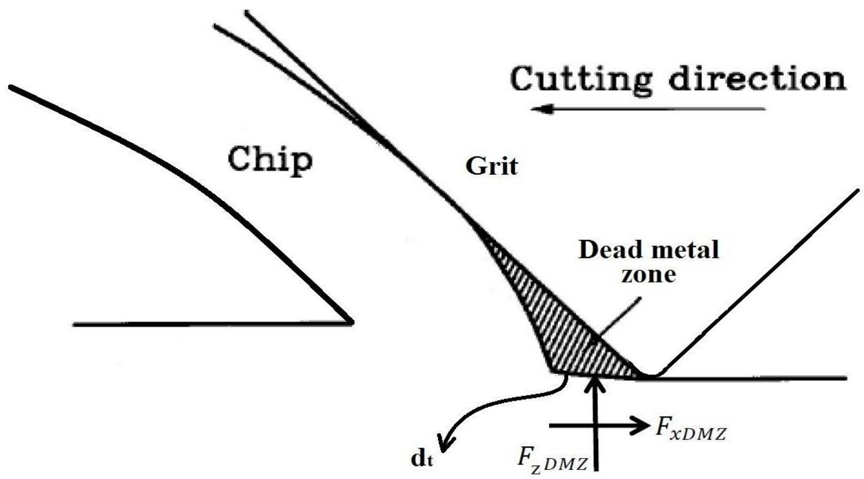

Figure 3-6 formation of the dead metal zone

Different studies show that contrary to build up edge, DMZ it is stable [112] and its size increases when the undeformed chip thickness and the absolute value of the negative rake angle increase [43]. The physical mechanism of such behavior could be explained by the fact that because of the high negative rake angle where the material was trapped ahead of the tool tip, it acted as the effective stable cutting edge [113]. By increasing the absolute value of the rake angle more (making it more negative) more material is trapped at the tip of the tool, and the region ahead of the tool will increase. Ohbuchi and Obikawa [43] also showed that models with DMZs give smaller energy required for cutting than pure shear plane models and concluded that the dead zone is stable and its size is related to the uncut chip thickness. Even though much research has been conducted to confirm the formation of the dead metal zone with tools having large negative rake angles, and there is evidence of the existence of the region in the grinding process using quick-stop device, no effort has been devoted considering its effect in the grinding force models.

In order to provide more evidence of DMZ in this thesis, grinding grits were investigated to find the trace of the dead zone in the form of stuck material on the rake faces of the grits. Figure 3-7 shows some of the grits observed under SEM after the grinding tests. The circles in the figure show the sticking material on the grits.

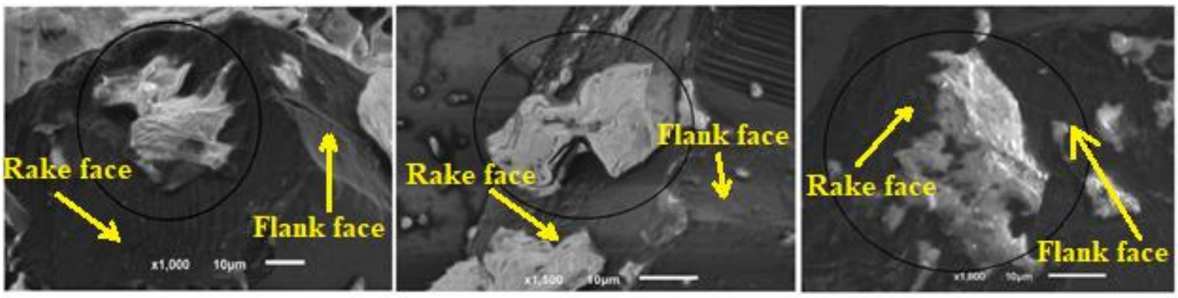

Figure 3-7 SEM photos of CBN grits with sticking material on the rake face

Based on the experimental investigation, theoretical study and the FEA [43] the following assumptions are considered on the existent conditions and properties of the dead metal zone in this thesis:

1. The formation of the dead metal zone depends on the rake angle of a grit and the undeformed chip thickness it experiences
2. It is formed when the undeformed chip thickness is greater than the critical chip thickness and the absolute rake angle is greater than 15^o, i.e. less than -15^0.
3. The size of the dead metal zone is proportional to the undeformed chip thickness and the negative rake angle of the grit.
4. The horizontal distance between the tip of the dead metal zone and the grit, d_t, is approximated as:

$$d_t = h.\tan^{1.64}(-\alpha_n) \qquad (3-21)$$

The above assumptions are based on the findings of many experimental and theoretical studies that confirming that rake angle and undeformed chip thickness were influential factors in dead metal zone. It can physically be understood that by increasing the negative rake angle the formation of chip will be more difficult and more material will be trapped as the dead metal zone. This is also the case for the undeformed chip thickness [41-43].

In this thesis, it is also assumed that constant normal pressure of P_0 occurred along d_t and shear occurs in the region due to the high normal pressure of P_0 [114]. P_0 is the maximum normal pressure at the tip of a cutting tool in dual zone model and it is reasonable to assume this pressure exist along d_t Based on these assumptions, friction and normal force (due to the existence of DMZ for a single grit) are as follows respectively:

$$F_{xDMZ} = \tau_1 . d_t . w_c \qquad (3-22)$$
$$F_{zDMZ} = P_0 . d_t . w_c$$

where w_c is the width of cutting edge, τ_1 is shear stress at the exit of shear plane and P_0 is maximum normal pressure acting on the grit tip.

3.4 Total Grinding Force

Based on the grit-workpiece interaction, the grinding force is obtained for each active grit and the summation of the forces on all the active grits results in the total grinding force.

In conclusion, depending on the chip thickness value, the grinding force for *i*th grit in *j*th element is made up of three components i.e. ploughing, cutting and DMZ:

$$\begin{cases} F_{x(i,j)} = F_{xc(i,j)} + F_{xp(i,j)} + F_{xDMZ(i,j)} \\ F_{z(i,j)} = F_{zc(i,j)} + F_{zp(i,j)} + F_{zDMZ(i,j)} \end{cases} \qquad (3-23)$$

If the uncut chip thickness for the grit is greater than the critical value, all of the above force components contribute to the total grinding force. However, for the values smaller than the critical undeformed chip thickness, only ploughing occurs.

The total grinding force is calculated by integrating the force value for all active grits and elements:

$$\begin{cases} F_{x\_total} = \sum_{j=1}^{k} \sum_{i=1}^{n} F_{x(i,j)} \\ F_{y\_total} = \sum_{j=1}^{k} \sum_{i=1}^{n} F_{y(i,j)} \end{cases} \qquad (3-24)$$

where k is the total number of elements. The flowchart of the proposed model is shown in Figure 3-8.

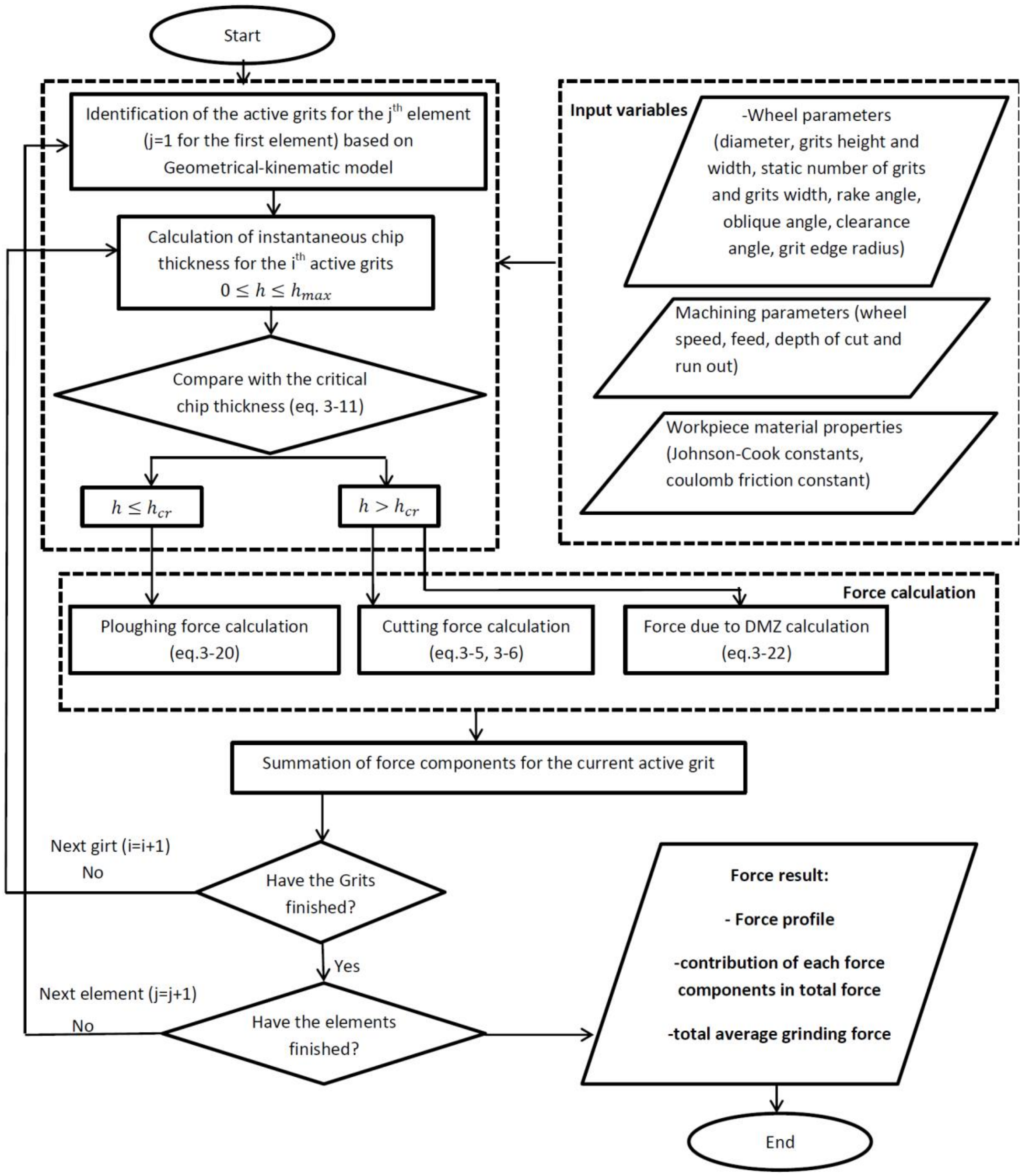

Figure 3-8 Algorithm of the grinidng force model

According to Figure 3-8, the trajectory of the grits will be calculated based on the inputs, including grit parameters, grinding conditions and active grits. By having the trajectory of the active grits, instantaneous chip thicknesses are identified accordingly (Equation 2-7). Chip thickness is compared with the critical chip thickness obtained from Equation 3-11. If the chip thickness is smaller than the critical value, ploughing is the only portion of the total force which is calculated using Equation 3-22. If the chip thickness is bigger than the critical value, the cutting force and force due to the formation of the DMZ also come into play. These force components are calculated from Equation 3-5 and 3-6, respectively. All the force components for the active grits are added and the calculation will be repeated for all the active grits in the first element. The same procedure is conducted for the entire wheel's elements and finally, the total force is obtained by adding up the elemental forces. Using this approach provides detailed information about the grinding force including the contribution of each force component to the total force, the fluctuation of the grinding force in every wheel revolution which can be used to obtain the maximum and average grinding force as well.

4 THERMAL MODELING OF GRINDING PROCESS

A general review of the current state in temperature modeling of the process was presented in the first chapter. In this chapter a new 3D temperature model is developed considering realistic assumptions. After presenting the temperature model the burn model which can predict the condition in which workpiece burn occur is presented in the next chapter.

Based on what was discussed in the literature regarding the temperature models in the grinding processes, it can be concluded that most of the analytical models developed so far are two-dimensional and the temperature field was calculated in macro-scale level where the wheel-workpiece interaction was considered as the source of the heat. As a result, a constant average value of the grinding force is used to calculate the power and heat flux. However, the grinding force as modeled in chapter 3 is the result of active grit interaction with the workpiece causing intermittent force pulse similar to that of milling processes [17]. There are even some cases where the grinding force fluctuates between zero and its maximum value as a result of wheel vibration coming from run out or the grinding force itself. Grinding of parts with single layer electroplated wheel with a long arbor is a common example of this which will be shown in Chapter 6. Other important cases are slotted, segmented and engineered wheels where the grits are positioned precisely on the wheel with a pattern [115]. In all above cases the grinding force fluctuates with different frequencies depending on the situation. Accordingly, the heat source is a function of both time and position. One may argue that heat conduction phenomenon is slower compared to force or vibration and time-dependent nature of the heat source may not have any effect on the process. This objection may be explained by this fact that heat affect in the grinding zone is limited to a small region called heat affected zone and any rapid change in heat source can be sensed in that region. However, the heat source fluctuation effect will be faded far from the position of the heat source. This physical effect will be study in this chapter. Apart from the heat source distribution, boundary conditions especially in wet grinding in analytical models have not been fully considered i.e. the heat convection from the side walls has been neglected. In this chapter, the aim is to take these factors into account through developing an analytical 3D temperature model with a time dependent heat source which considers more realistic boundary conditions in wet and dry grinding. The proposed model is able to provide detailed information of the temperature distribution in the workpiece analytically without much computational time and effort compared to FEM solutions. Another advantage of the model is its ease of use in production applications. The maximum temperature of the workpiece can be predicted analytically and used in selection of grinding conditions to achieve maximum productivity (MRR) without causing any thermal damage to the parts. The temperature profile in the workpiece may be obtained from the model and be used in CCT and TTT diagrams to observe any microstructure change, phase transformation or surface burn in the workpiece.

First background information useful to better understanding the temperature model is given.

4.1 Background information

The differential equation of conduction of heat in an isotropic solid is as follow:

$$\frac{\partial^2 T}{\partial x^2}+\frac{\partial^2 T}{\partial y^2}+\frac{\partial^2 T}{\partial z^2}=\frac{1}{\alpha}\frac{\partial T}{\partial t} \qquad (4-1)$$

where α is thermal conductivity:

$$\alpha=\frac{k}{\rho c}$$

Where k is thermal conductivity, ρ is the density and c is specific heat capacity of the solid.

The solution of equation 4-1 in case of a point heat source moving with the velocity of f along the x direction in an infinite body can be obtained as [52]:

$$\mathrm{T(x,y,z,t)}=\frac{q_w}{8\rho c\sqrt{(\pi\alpha)^3}}\int_0^{\tau}\frac{dt}{\sqrt{(\tau-t)^3}}e^{-\frac{\left(x-f(\tau-t)\right)^2+\left(y-y'\right)^2+(z-z')^2}{4\alpha(\tau-t)}} \qquad (4-2)$$

where q_w is the strength of heat source, τ is time, y' and z' are the coordinates of the heat source position in y and z directions, ,respectively. α is the thermal diffusivity defined as:

$$\alpha = \frac{k}{\rho c}$$

where k is the thermal conductivity, ρ is the density and c is the specific heat capacity of the solid.

Jaeger [52] calculated the heat conduction in a semi-infinite solid ($z < 0$) where there is no loss of heat in the surface of $z = 0$ due to a rectangular moving heat source with sides $2l$ and $2b$ in x and y direction respectively. The heat source is moving with the velocity of f along the x axis as shown in Figure 4-1. The temperature at any point in the solid with coordinate of (x, y, z) after τ second is given as [52]:

$$T(x,y,z,\tau) = \frac{q_w \alpha}{4k\sqrt{(\pi\alpha)^3}} \int_0^{\tau} \frac{dt}{\sqrt{(\tau - t)^3}} \int_{-l}^{l} dx' \int_{-b}^{b} e^{-\frac{\left(x-x'+f(\tau-t)\right)^2+\left(y-y'\right)^2+z^2}{4\alpha(\tau-t)}} dy' \qquad (4-3)$$

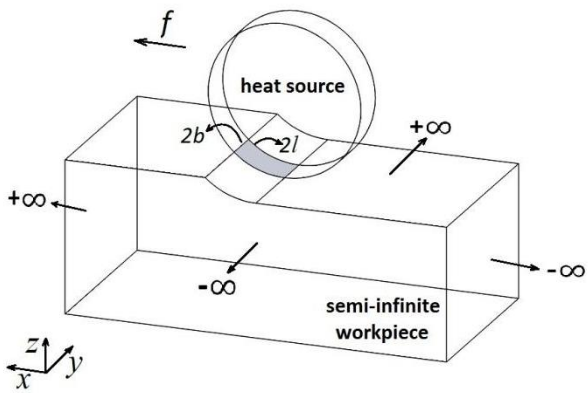

Figure 4-1 rectangular heat source in semi-infinite workpiece in grinding

When the wheel engages with the workpiece the temperature in the workpiece material rises rapidly first and after a few wheel revolutions the steady state temperature is reached. This can be considered mathematically in the above equation by setting τ=∞. Even though equation 4-3 can easily be solved numerically it can be further simplified by taking the integrals respect to x' and y'. By following changing of variables, equation 4-4 will be obtained:

$X = \frac{fx}{2\alpha}, Y = \frac{fy}{2\alpha}, Z = \frac{fz}{2\alpha}, L = \frac{fl}{2\alpha}, B = \frac{fb}{2\alpha}, u = \frac{f^2(\tau - t)}{2\alpha}$

$$T(x, y, z, \tau) = \frac{q_w \alpha}{2Kf\sqrt{2\pi}} \int_0^{f^2\tau/2\alpha} e^{-\frac{Z^2}{2u}} \frac{du}{\sqrt{u}} \left[\mathrm{erf}\left(\frac{Y+B}{\sqrt{2u}}\right) - \mathrm{erf}\left(\frac{Y-B}{\sqrt{2u}}\right)\right] \left[\mathrm{erf}\left(\frac{X+L+u}{\sqrt{2u}}\right) - \mathrm{erf}\left(\frac{X-L+u}{\sqrt{2u}}\right)\right] \quad (4-4)$$

where $\mathrm{erf}(x) = \frac{2}{\sqrt{\pi}} \int_0^x e^{-t^2} dt$ is the error function. If the heat source is a function of the position along x axis, which is the case in grinding, q_w in Equation 4-4 should be inside the integral. Assuming a triangle heat source of $q_w = q_{av}(1 + \frac{x}{l})$ in Equation 4-4 the following equation is obtained:

$$T(x, y, z, \tau) = \frac{q_{av} \alpha}{2Kf\sqrt{2\pi}} \int_0^{f^2\tau/2\alpha} \frac{du}{\sqrt{u}} e^{-Z^2/2u} \left[\mathrm{erf}\left(\frac{Y+B}{\sqrt{2u}}\right) - \mathrm{erf}\left(\frac{Y-B}{\sqrt{2u}}\right)\right] \left[\left(1 + \frac{X+u}{L}\right)\left(\mathrm{erf}\left(\frac{X+L+u}{\sqrt{2u}}\right) - \mathrm{erf}\left(\frac{X-L+u}{\sqrt{2u}}\right)\right) + \frac{\sqrt{2u}}{\sqrt{\pi}L}\left(e^{-\frac{(X+u+L)^2}{2u}} - e^{-\frac{(X+u-L)^2}{2u}}\right)\right] \quad (4-5)$$

where q_{av} is the average heat flux.

Equation 4-4 or 4-5 cannot be used to predict the temperature of a workpiece with a finite width. In previous analytical models, moving a band heat source has been used to predict the temperature of a workpiece where its width is quite long [75,76] It should be mentioned that the band heat source equation can be obtained from Equation 4-4 and 4-5 when the width of cut goes to infinity. Infinite width in here can be used when the width of workpiece is quite long. In the case of a constant heat source the famous solution of moving band heat source in the steady state condition can be obtained from Equation 4-4 where τ and B go to infinity:

$$T(x, z) = \frac{q_w}{\pi K} \int_{-l}^{l} e^{-\frac{f(x-u)}{2\alpha}} K_0 \left\{\frac{f}{2\alpha} \sqrt{[(x-u)^2 + z^2]}\right\} du \quad (4-6)$$

where $K_0(x)$ is the modified Bessel function of the second kind of order zero.

For a triangular heat source, the solution is obtained as [116]:

$$T(x, y, z, \tau) = \frac{q_{av} \alpha}{Kf\sqrt{2\pi}} \int_0^{f^2\tau/2\alpha} \frac{du}{\sqrt{u}} e^{-Z^2/2u} \left[\left(1 + \frac{X+u}{L}\right)\left(\mathrm{erf}\left(\frac{X+L+u}{\sqrt{2u}}\right) - \mathrm{erf}\left(\frac{X-L+u}{\sqrt{2u}}\right)\right) + \frac{\sqrt{2u}}{\sqrt{\pi}L}\left(e^{-\frac{(X+u+L)^2}{2u}} - e^{-\frac{(X+u-L)^2}{2u}}\right)\right] \quad (4-7)$$

In the equations above the effect of convection due to the coolant has not been considered. Des Ruisseaux and Zerkle [59] developed a 2D formula for the temperature rise in a semi-infinite body due to a rectangular heat source where there is a convective boundary condition on the top surface of the body:

$$T(x,z) = \frac{2q_{av}\alpha}{\pi K f}\int_{X-L}^{X+L} e^{-u}K_0\left\{[Z^2+u^2]^{\frac{1}{2}}\right\}du - \pi H e^{HZ}\int_0^{\infty}\tau e^{H^2\tau^2}\mathrm{erfc}\left(H\tau+\frac{Z}{2\tau}\right)\left\{\mathrm{erf}\left(\tau+\frac{X+L}{2\tau}\right) - \mathrm{erf}\left(\tau+\frac{X-L}{2\tau}\right)\right\}d\tau \qquad (4-8)$$

where $erfc(x) = 1 - erf\ (x)$ and H is dimensionless convective heat transfer coefficient defined as:

$$H = \frac{2\alpha h}{kf}$$

where h is convective heat transfer coefficient or convective factor of the coolant which can be calculated by using the laminar flow model which is based on the boundary layer theory of laminar flow passing a flat surface [50]:

$$h = \frac{4}{9}{k_f}^{2/3}{\rho_f}^{1/2}{c_f}^{1/3}{\eta_f}^{-1/6}\sqrt{\frac{V_c}{l_c}} \qquad (4-9)$$

where k_f is thermal conductivity of fluid, ρ_f, c_f and η_f are the density, specific heat capacity and dynamic viscosity of the coolant, respectively.

The solution of Des Ruisseaux and Zerkle model for a triangular heat source with a same boundary condition can be obtained as [116]:

$$T(x,y,z,\tau) = \frac{q_{av}\alpha}{Kf\sqrt{2\pi}}\int_0^{\frac{f^2\tau}{2\alpha}}\frac{1}{\sqrt{u}}e^{-\frac{Z^2}{2u}}\left\{\left(1+\frac{X+u}{L}\right)\left(\mathrm{erf}\left(\frac{X+L+u}{\sqrt{2u}}\right)-\mathrm{erf}\left(\frac{X-L+u}{\sqrt{2u}}\right)\right)+\frac{\sqrt{2u}}{\sqrt{\pi}L}\left(e^{-\frac{(X+u+L)^2}{2u}}-e^{-\frac{(X+u-L)^2}{2u}}\right)\right\} - H\sqrt{\frac{\pi u}{2}}\ erfc\left(\frac{Z}{\sqrt{2u}}+H\sqrt{\frac{u}{2}}\right)\ e^{\left(\frac{uH^2}{2}+ZH\right)}du \qquad (4-10)$$

4.2 Three-dimensional Thermal Model

In this section, a three-dimensional analytical thermal model considering different boundary conditions representing dry and wet grinding is proposed. Taking the micro-interaction of the grit-workpiece into account, a rectangular time-dependent heat source model with a width of $2b$ equal to the width of the wheel (Figure 4-2a) is used. First, different boundary conditions are considered for a constant heat source, then the effect of having a time dependent heat source is applied to obtain the ultimate solution.

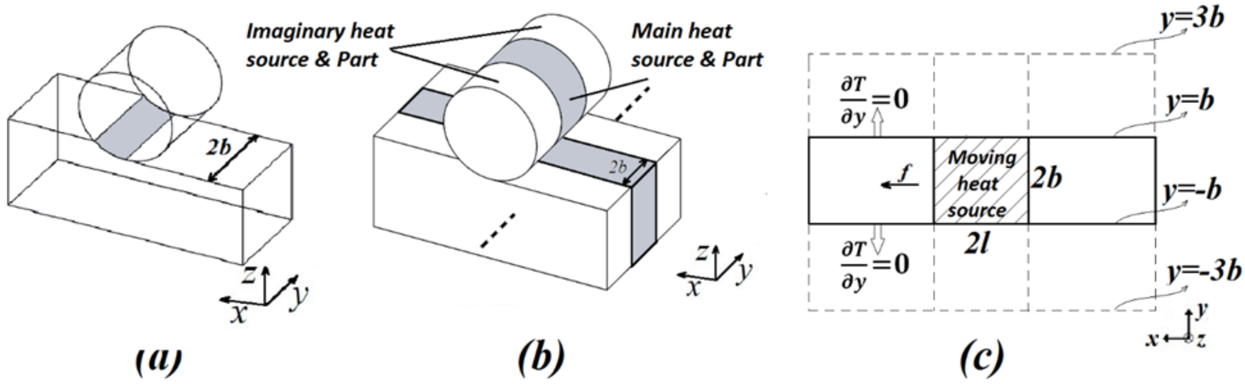

*Figure 4-2 **a)** Rectangular heat source on a body with a finite width b) main and imaginary heat source and workpiece c) 2D view of the workpiece*

4.2.1 Applying Boundary conditions

4.2.1.1 Dry condition

Compared to the heat conduction in metal solids, heat radiation to the surrounding environment via air can be negligible. As a result, an adiabatic boundary condition can be applied on all the free surfaces of the workpiece as

$$\frac{\partial T}{\partial y} = 0 \text{ at surfaces: } y = b, y = -b \text{ and } \frac{\partial T}{\partial z} = 0 \text{ at } z = 0$$

The method of images is used to solve the problem of heat conduction where the solid is bounded by planes [52]. Based on this method it is assumed that the solid is continued in all directions, and then by applying imaginary heat or sink sources on the imaginary parts, the boundary conditions will be considered (Figure 4-2b). It is assumed that the workpiece is continuous along the y axis. This can be done by imagining infinitive bodies at the same width as the original body (dashed lines in Figure 4-2c). Since there is no heat exchange at planes of $y = b$ and $y = -b$ there should be an imaginary heat source at imaginary bodies so that adiabatic boundary condition can be satisfied. The same imaginary heat sources should be applied on other surfaces of $y = 3b$,$y = -3b$, $y = 5b$, $y = -5b$ and so on. As a result, the temperature at any point with the coordinate of (x, y, z) in the bounded solid is due to the heat source at the original body and n imaginary heat source applied along the y axis. If a point element of the heat source is considered in the body between $y = b$ and$y = -b$, the image of this element heat source respect to $y = b$ and$y = -b$ plane causes no heat loss at the boundaries. The same approach should be adopted for$(2n + 1)b$. Accordingly, heat sources exist at points $(2n + 1)2b - y'$ and $(2n)2b + y'$.

$$T(x, y, z, \tau) =$$

$$\frac{q_w \alpha}{4\sqrt{(\pi\alpha)^3}} \int_0^\tau \frac{dt}{\sqrt{(\tau-t)^3}} \int_{-l}^{l} dx' \int_{-b}^{b} dy' \sum_{n=0}^{+\infty} \mathrm{e}^{-\frac{\left(x-x'+f(\tau-t)\right)^2+\left(y\pm(2n+1)(2b)+y'\right)^2+z^2}{4\alpha(\tau-t)}} +$$

$$\frac{q_w \alpha}{4\sqrt{(\pi\alpha)^3}} \int_0^\tau \frac{dt}{\sqrt{(\tau-t)^3}} \int_{-l}^{l} dx' \int_{-b}^{b} dy' \sum_{n=0}^{+\infty} e^{-\frac{\left(x-x'+f(\tau-t)\right)^2+\left(y\pm(2n)(2b)-y'\right)^2+z^2}{4\alpha(\tau-t)}}$$

Or in a more compact form:

$$T(x, y, z, \tau) =$$

$$\frac{q_w \alpha}{4\sqrt{(\pi\alpha)^3}} \int_0^\tau \frac{dt}{\sqrt{(\tau-t)^3}} \int_{-l}^{l} dx' e^{-\frac{\left(x-x'+f(\tau-t)\right)^2+z^2}{4\alpha(\tau-t)}} \left[\int_{-b}^{b} dy' \sum_{n=0}^{+\infty} e^{-\frac{\left(y\pm 4nb\pm 2b+y'\right)^2}{4\alpha(\tau-t)}} + \sum_{n=0}^{+\infty} e^{-\frac{\left(y\pm 4nb-y'\right)^2}{4\alpha(\tau-t)}}\right]$$

Considering a triangular heat source and taking the above integral respect to x' and y', analytical solution of grinding temperature for a slab workpiece with adiabatic boundary solutions is obtained as:

$$T(x, y, z, \tau) = \frac{q_{av}\alpha}{2Kf\sqrt{2\pi}} \int_0^{f^2\tau/2\alpha} \frac{du}{\sqrt{u}} e^{-Z^2/2u} \left[\operatorname{erf}\left(\frac{Y+nB}{\sqrt{2u}}\right) - \operatorname{erf}\left(\frac{Y-nB}{\sqrt{2u}}\right)\right] \left[\left(1 + \frac{X+u}{L}\right)\left(\operatorname{erf}\left(\frac{X+L+u}{\sqrt{2u}}\right) - \operatorname{erf}\left(\frac{X-L+u}{\sqrt{2u}}\right)\right) + \frac{\sqrt{2u}}{\sqrt{\pi}L}\left(e^{-\frac{(X+u+L)^2}{2u}} - e^{-\frac{(X+u-L)^2}{2u}}\right)\right] \quad (4-11)$$

When n goes to infinity the term $\left(\frac{Y+nB}{\sqrt{2u}}\right) - \left(\frac{Y-nB}{\sqrt{2u}}\right)$ is equal to 2 and the results are the same as the semi-infinite problem (equation 4-7). In another word, adiabatic boundary condition applied on the side walls causes no temperature variation in y direction and the 2D solution is valid and can be used in dry condition.

4.2.1.2 Wet Condition

In this subsection grinding temperature equations in case of using coolant on a slab with width of b will be considered.

The effect of convective boundary condition on the sides of the slab is considered in this subsection. In this case convective boundary condition exists on the three surfaces of slab i.e. $z = 0, y = 0, y = b$ as follows (figure 4-3):

$$hT(x, y, 0, t) = k\frac{\partial T}{\partial z}(x, y, 0, t);$$

$$hT(x, 0, z, t) = hT(x, b, z, t) = k\frac{\partial T}{\partial y}(x, 0, z, t) = k\frac{\partial T}{\partial y}(x, b, z, t)$$

where h is the convection coefficient.

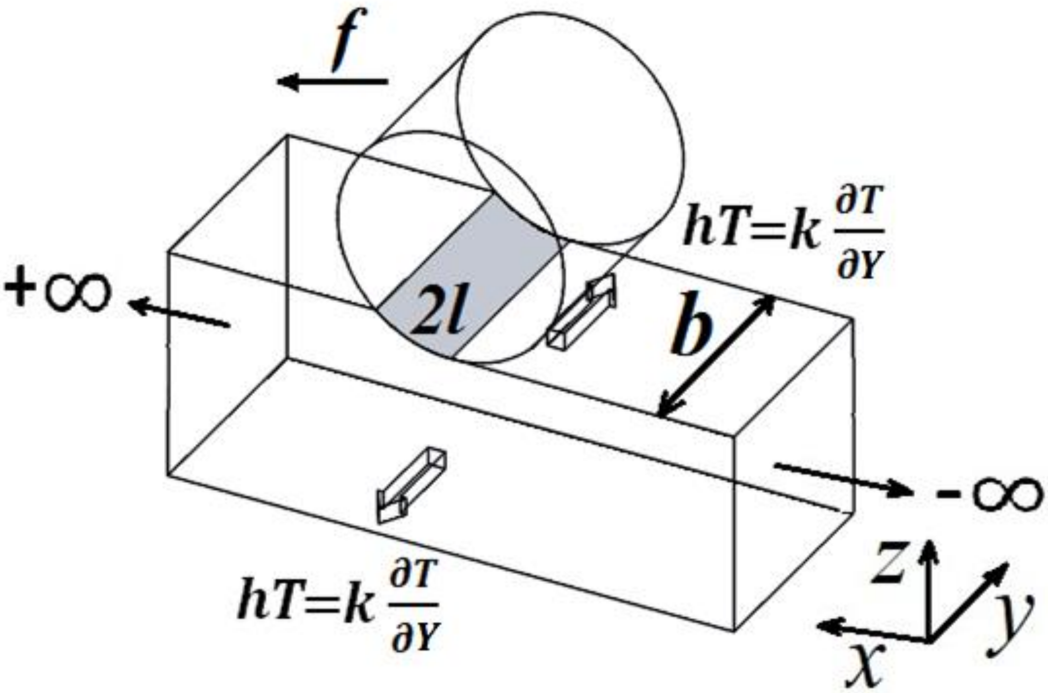

Figure 4-3 Boundary conditions in case of wet grinding of a slab

It can be shown that [52] the solution for the heat conduction equation in three dimensions is the product of the solutions of three one-variable problems. This approach is used to build the equation of heat conduction with convective boundary conditions here.

The solution of heat conduction for a unit instantaneous source and convective boundary condition in $z = 0$ is [52]:

$$T_1(z,t) = \frac{1}{2\sqrt{\pi\alpha t}}\left\{e^{-\frac{(z-z')^2}{4\alpha t}} + e^{-\frac{(z+z')^2}{4\alpha t}} - \frac{2h}{k}\int_0^\infty e^{-(\frac{h\gamma}{k}+\frac{(z+z'+\gamma)^2}{4\alpha t})}d\gamma\right\}$$

$$= \frac{1}{2\sqrt{\pi\alpha t}}\left[e^{-\frac{(z-z')^2}{4\alpha t}} + e^{-\frac{(z+z')^2}{4\alpha t}} - \frac{2h}{k}\sqrt{\pi\alpha t}\, erfc\left(\frac{z+z'}{2\sqrt{\alpha t}} + \frac{h}{k}\sqrt{\alpha t}\right)e^{\alpha t\frac{h^2}{k^2}+\frac{h}{k}(z+z')}\right] \qquad (4-12)$$

The solution of heat conduction for a unit instantaneous plane source and convective boundary condition in $y = 0, b$ is [52]:

$$T_2(y,t) = 2\sum_{n=1}^{\infty} e^{-\alpha.\beta_n{}^2 t} \frac{(\beta_n \cos\beta_n y + \frac{h}{k} sin\beta_n y)(\beta_n \cos\beta_n y' + \frac{h}{k} sin\beta_n y')}{b\left(\beta_n{}^2 + \frac{h^2}{k^2}\right) + \frac{2h}{k}} \quad (4-13)$$

where β_n is the positive roots of:

$$tan\ tan\ (\beta b) = \frac{2\beta \frac{h}{k}}{\beta^2 - \frac{h^2}{k^2}}$$

The solution of heat conduction for a unit instantaneous plane source is [52]:

$$T_3(x,t) = \frac{1}{2\sqrt{\pi\alpha t}} e^{-\frac{(x-x')^2}{4\alpha t}} \quad (4-14)$$

Finally, the solution for the equation of heat in a semi-finite slab with the convective boundary conditions is the product of the above equations [52]:

$$T(x,y,z,t) = T_1(z,t) * T_2(y,t) * T_3(x,t)$$

Accordingly, the following equations are obtained:

$$T(x,y,z,t) = \frac{1}{2\sqrt{\pi\alpha t}}\left[e^{-\frac{(z-z')^2}{4\alpha t}} + e^{-\frac{(z+z')^2}{4\alpha t}} - \frac{2h}{k}\sqrt{\pi\alpha t}\ erfc\left(\frac{z+z'}{2\sqrt{\alpha t}} + \frac{h}{k}\sqrt{\alpha t}\right) e^{\alpha t\frac{h^2}{k^2} + \frac{h}{k}(z+z')}\right] \times$$
$$\left[2\sum_{n=1}^{\infty} e^{-\alpha.\beta_n{}^2 t} \frac{(\beta_n \cos\beta_n y + \frac{h}{k} sin\beta_n y)(\beta_n \cos\beta_n y' + \frac{h}{k} sin\beta_n y')}{b\left(\beta_n{}^2 + \frac{h^2}{k^2}\right) + \frac{2h}{k}}\right] \frac{1}{2\sqrt{\pi\alpha t}} e^{-\frac{(x-x')^2}{4\alpha t}} \quad (4-15)$$

which can be simplified as:

$$T(x,y,z,t) = \frac{1}{4\pi\alpha t}\left[e^{-\frac{(x-x')^2+(z-z')^2}{4\alpha t}} + e^{-\frac{(x-x')^2+(z+z')^2}{4\alpha t}} - 2\frac{h}{k}\sqrt{\pi\alpha t}\, erfc\left(\frac{z+z'}{2\sqrt{\alpha t}} + \frac{h}{k}\sqrt{\alpha t}\right) e^{\alpha t\frac{h^2}{k^2}+\frac{h}{k}(z+z')-\frac{(x-x')^2}{4\alpha t}}\right] \times \left[2\sum_{n=1}^{\infty} e^{-\alpha.\beta_n{}^2 t}\frac{(\beta_n \cos\beta_n y + \frac{h}{k} sin\beta_n y)(\beta_n \cos\beta_n y' + \frac{h}{k} sin\beta_n y')}{b\left(\beta_n{}^2 + \frac{h^2}{k^2}\right) + \frac{2h}{k}}\right] \quad (4-16)$$

The solution due to a moving triangular heat source at plane z ($z' = 0$) with the length of $2l$ on a slab with the length of b moving along x axis is obtained by integration of equation 4-16 and changing the variables as before:

$$T(X,Y,Z,\tau) = \frac{2q_{av}\alpha}{fk\sqrt{2\pi\alpha}}\int_0^{f^2\tau/2\alpha}\frac{du}{\sqrt{2u}}\left[\left(1+\frac{X+u}{L}\right)\left(\mathrm{erf}\left(\frac{X+L+u}{\sqrt{2u}}\right) - \mathrm{erf}\left(\frac{X-L+u}{\sqrt{2u}}\right)\right) + \frac{\sqrt{2u}}{\sqrt{\pi}L}\left(e^{-\frac{(X+u+L)^2}{2u}} - e^{-\frac{(X+u-L)^2}{2u}}\right)\right]\left[e^{-\frac{Z^2}{2u}} - H\sqrt{\frac{\pi u}{2\alpha}}\, erfc\left(\frac{Z}{\sqrt{2u}} + H\sqrt{\frac{\pi u}{2\alpha}}\right) e^{\frac{uH^2}{2}+ZH} \times \sum_{n=1}^{\infty} e^{\frac{-2\alpha^2 u.\beta_n{}^2}{f^2}}\frac{(\beta_n \cos\beta_n y + \frac{Hf}{2\alpha} sin\beta_n y)(\sin\beta_n b + \frac{Hf}{2\alpha\beta_n}(1-cos\beta_n b))}{b\left(\beta_n{}^2 + \left(\frac{Hf}{2\alpha}\right)^2\right) + \frac{Hf}{\alpha}}\right] \quad (4-17)$$

4.2.2 Time Dependent Heat Source

The grinding force in tangential direction must be known to drive the heat flux transferred to the workpiece. In this section the dynamic nature of the grinding force is discussed and used in the temperature model. In previous models the average grinding force were used to drive the heat source strength as:

$$q_{av} = \frac{\varepsilon F_t . V_c}{2L_c . b} \qquad (4-18)$$

where F_t is average tangential grinding force, V_c is wheel speed, L_c is wheel-workpiece contact length and b is half of wheel width. Equations 4-11 and 4-17 derived in the previous section are the solution of the moving heat source for a slab in dry and wet conditions respectively where the average heat flux has been considered. In those equations the heat source was a function of position and a triangular heat source distribution was used to drive the solution. However, the strength of the heat source is proportional to the tangential force which is the result of many micro-interactions of the active grits with the workpiece as it modeled and discussed in detail in chapter 3. Summation of these micro-interactions produces a force profile which is repeated for each wheel revolution. Accordingly, the dynamic nature of the grinding force should be included in the heat flux equation. The analytical grinding force model developed in chapter 3 is utilized in here to build the time dependent heat source model. The grinding force in x direction is summation of micro force created by all active grits in all elements as follow:

$$F_x(t) = \sum_{j=1}^{k} \sum_{i=1}^{n} F_{xc(i,j)} + F_{xp(i,j)} + F_{xDMZ(i,j)} \qquad (4-19)$$

where k and n represent the number of wheel elements and number of active grits in each element, respectively.

Two common sample cases of the grinding force have been simulated by the force model and shown in Figure 4-4 and 4-5 to emphasize the importance of the dynamic part of the force. Figure 4-4 shows the horizontal grinding force when a single layer CBN electroplated wheel with 5 µm eccentricity is used while Figure 4-5 shows the force when a conventional grinding wheel used assuming the wheel is dressed and there is no any vibration in the system. The average grinding force has been reported in the figures to compare with the force range as an indicator of force fluctuation. As it can be seen in Figure 4-4, major force fluctuation is due to wheel run out and the frequency of vibration is related to wheel rotational speed. Generally, when a single layer wheel is used some amount of run out exists and cannot be eliminated since the wheel cannot be dressed. In this case, because of the wheel run out the dynamic radius of the grits change and active grits concentrate in a same position on the wheel for the all elements. In another word, the active grits interact with the workpiece when the wheel is in a specific rotational position. The force fluctuation also exists for the case where the wheel has no vibration (Figure 4-5) though it is smaller than the previous case. The force fluctuation in this case is attributed to the stochastic nature of grits on the wheel specifically grit width and height distribution. When the wheel is free of any vibration, the active grits are randomly distributed on the wheel (red dot in Figure 4-6). As the wheel rotates, some active grits in an element create force pulse while the positions of the active grits are completely random for the next element. In other words, while the wheel is rotated the position of the cutting edges are completely random in axial direction. In addition, the width of the each element (w_c) which is some portion of grit width has a random characteristic. These stochastic parameters make the grinding force having a random value (depending on the position of the active grits and their width) as the wheel rotates. This is the reason of the force fluctuation in Figure 4-5.

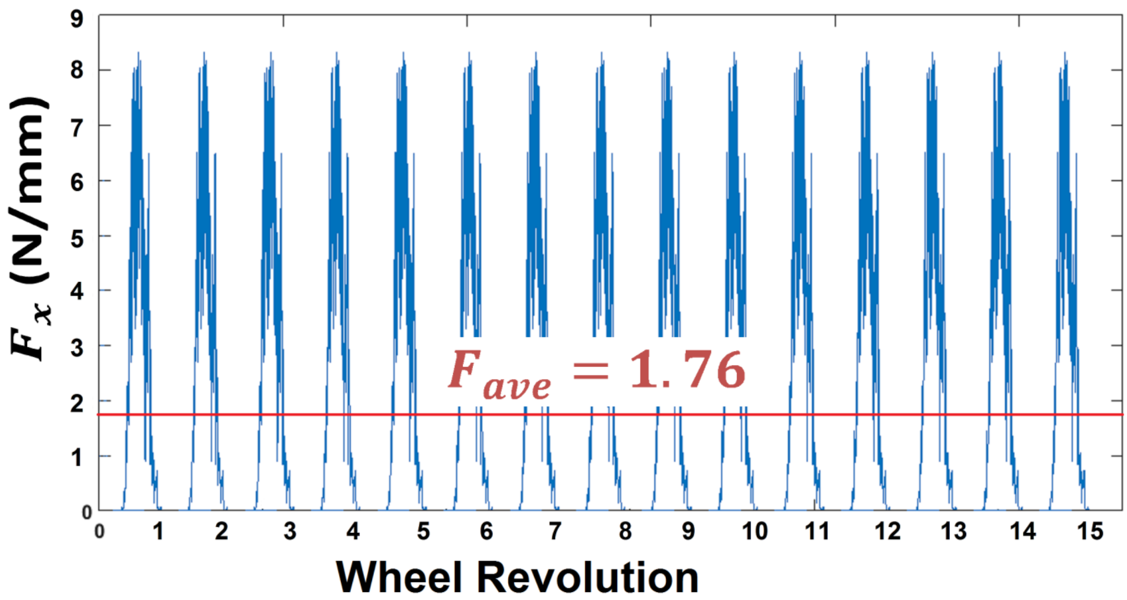

Figure 4-4 Horizontal grinding force per unit width for a CBN single layer wheel, run out 5 µm, wheel diameter 20mm, wheel rpm 12000, feed 2000 mm/min, depth of cut 0.04mm, workpiece material: bearing steel, grit height standard deviation 10 µm, grit width of cut standard deviation 3 µm

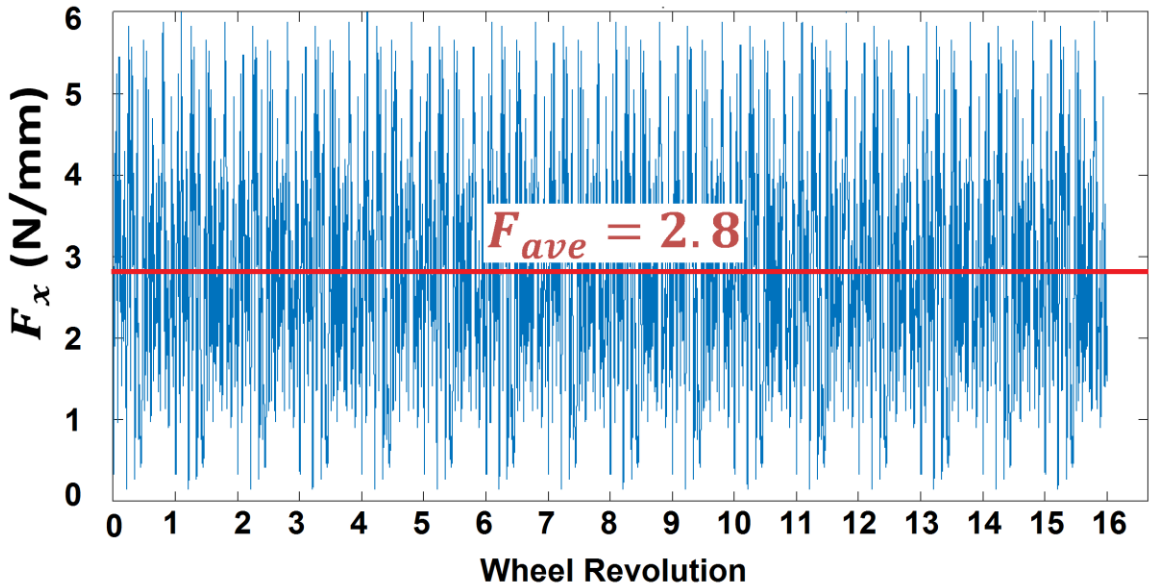

Figure 4-5 Horizontal grinding force per unit width for a dressed aluminum wheel, wheel diameter 40mm, wheel rpm 6000, feed 1000 mm/min, depth of cut 0.06 mm, workpiece material: bearing steel, grit height standard deviation 8 µm, grit width of cut standard deviation 4 µm

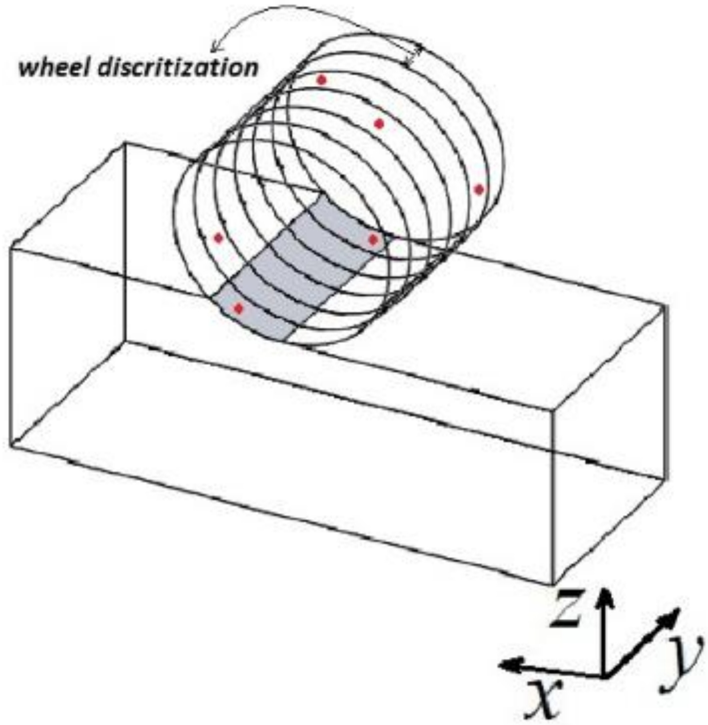

Figure 4-6 wheel discritization and position of the active grits

Experimental investigations of the grinding force reported in the literature confirm above results indicating the force fluctuation is considerable. Data reported in [35] show that the grinding force amplitude is approximately 40% of the average value when a conventional dressed wheel is used to cut steel. This ratio was approximately 50% in the experimental grinding force measurement reported in [17] where a vitrified aluminum dressed wheel was used.

Based on what has been discussed above, the heat source has a dynamic nature and is a function of both position and time. By considering a triangle distribution of heat source along the contact length, and the dynamic nature of the grinding force, the heat flux can be modeled as:

$$q_w(x,t) = q_t(t).q_x(x) = \left(\frac{\varepsilon F_x(t).V_c}{2L_c.b}\right).\left(1+\frac{2x}{L_c}\right) \qquad (4-20)$$

where $q_t(t) = \frac{\varepsilon F_x(t).V_c}{2l_c.b}$ is a time function representing the time-dependent nature of the heat source, $q_x(x) = 1 + \frac{2x}{L_c}$ is the function that represent the position-dependent nature of the heat source, $L_c = \sqrt{d.D}$ is wheel-workpiece contact length, d is depth of cut, D is the wheel diameter and x is the position ranging from $-L_c/2$ to $L_c/2$. ε is the partition of the heat that goes to the workpiece known as the partition ratio and is defined as:

$$\varepsilon = \frac{q_w}{q_{total}} \quad (4-21)$$

The total heat produced in the process (q_{total}) is dissipated through four sinks i.e. chip (q_{ch}), workpiece (q_w), wheel (q_s) and coolant (q_f):

$$q_{total} = q_{ch} + q_w + q_s + q_f \quad (4-22)$$

The amount of heat dissipated by the coolant fluid is defined as:

$$q_f = h\Delta T \quad (4-23)$$

where ΔT is the maximum temperature rise in the contact area which is identified by iteration. It should be noted that if the maximum temperature exceeds the burn-out temperature of the fluid used as the coolant, calculation for the heat partition ratio must be repeated by setting the convective coefficient factor to zero. For example, assume that the workpiece maximum temperature predicted by the model is 250 ^{0}C when a water based coolant with the boiling temperature of 130 ^{0}C has been used. In this case, since the maximum temperature predicted by the model exceeds the coolant boiling temperature the amount of heat dissipation by coolant should be considered as zero. The heat carried away by the chip is calculated as:

$$q_{ch} = \frac{\mathrm{d}.f.\rho_w.c_w.T_{ch}}{L_c} \quad (4-24)$$

According to Rowe heat partition model [50], the portion of heat transferred to the workpiece is calculated as:

$$q_w = R_{ws}(q_{total} - q_{ch}) - q_f \quad (4-25)$$

where R_{ws} is wheel-workpiece fraction which is defined as:

$$R_{ws} = \frac{1}{\left(1 + \frac{k_g}{\sqrt{k_w.\rho_w.c_w.r_0.V_c}}.\frac{1}{F}\right)} \quad (4-26)$$

where k_w, ρ_w, c_w are thermal conductivity, specific heat capacity and density of workpiece material respectively, k_g is thermal conductivity of grit V_c is wheel speed, r_0

is the effective grit radius and F is a parameter reflecting the steady state condition defined as:

$$F = 1 - e^{-\frac{\varphi}{1.2}} \qquad (4-27)$$

where,

$$\varphi = \sqrt{(\alpha_g . L_c)/(r_0{}^2 . f)}$$

where α_g is the thermal diffusivity of the grain.

Ultimately, using equation 4-20 in equations 4-11 and 4-17 provides the final solution of heat conduction in a slab workpiece due to a time-dependent heat source in dry and wet grinding conditions, respectively, as follows:

$$T(x,y,z,\tau) = \frac{\alpha}{Kf\sqrt{2\pi}} \int_0^{f^2\tau/2\alpha} \frac{q_t(u)du}{\sqrt{u}} e^{-Z^2/2u} \left\{ \left(1 + \frac{X+u}{L}\right) \left(\operatorname{erf}\left(\frac{X+L+u}{\sqrt{2u}}\right) - \operatorname{erf}\left(\frac{X-L+u}{\sqrt{2u}}\right)\right) + \frac{\sqrt{2u}}{\sqrt{\pi}L}\left(e^{-\frac{(X+u+L)^2}{2u}} - e^{-\frac{(X+u-L)^2}{2u}}\right)\right\} \qquad (4-28)$$

$$T(x,y,z,\tau) = \frac{2\alpha}{fk\sqrt{2\pi\alpha}} \int_0^{f^2\tau/2\alpha} \frac{q_t(u)du}{\sqrt{2u}} \left\{ \left(1 + \frac{X+u}{L}\right) \left(\operatorname{erf}\left(\frac{X+L+u}{\sqrt{2u}}\right) - \operatorname{erf}\left(\frac{X-L+u}{\sqrt{2u}}\right)\right) + \frac{\sqrt{2u}}{\sqrt{\pi}L}\left(e^{-\frac{(X+u+L)^2}{2u}} - e^{-\frac{(X+u-L)^2}{2u}}\right)\right\} \left\{ e^{-\frac{Z^2}{2u}} - H\sqrt{\frac{\pi u}{2\alpha}}\, erfc\left(\frac{Z}{\sqrt{2u}} + H\sqrt{\frac{\pi u}{2\alpha}}\right) e^{\frac{uH^2}{2}+ZH} \times \sum_{n=1}^{\infty} e^{\frac{-2\alpha^2 u.\beta_n{}^2}{f^2}} \frac{(\beta_n \cos\beta_n y + \frac{Hf}{2\alpha} sin\beta_n y)(\sin\beta_n b + \frac{Hf}{2\alpha\beta_n}(1 - cos\beta_n b))}{b\left(\beta_n{}^2 + \left(\frac{Hf}{2\alpha}\right)^2\right) + \frac{Hf}{\alpha}} \right\} \qquad (4-29)$$

To the best knowledge of the author there is no analytical solution for the integrals in equations 4-28 and 4-29. MATLAB software was used to compute these integrals numerically.

4.3 Theoretical Results

4.3.1 Temperature Profile in Dry and Wet Condition

In this section, the theoretical temperature solution results of different cases are introduced. Figure 4-7 provides an overview of the 3D temperature profile of the slab at different conditions. Figure 4-7 (a) shows the profile of the temperature in dry condition considering a constant heat source, while Figure 4-7(b) shows the temperature considering a periodic heat source. In both figures temperature is constant along the width of the workpiece indicating the solution is 2D in dry condition. Figure 4-7(c) and (d) show the temperature profile in wet condition considering a constant and periodic heat source, respectively. All the other grinding parameters were kept constant compared to the result obtained for the dry condition. As it can be seen the temperatures near the sides are lower than in the ones close to the center in wet condition. This is due to heat dissipation from the sides of the slab by applying convective boundary conditions in the current model.

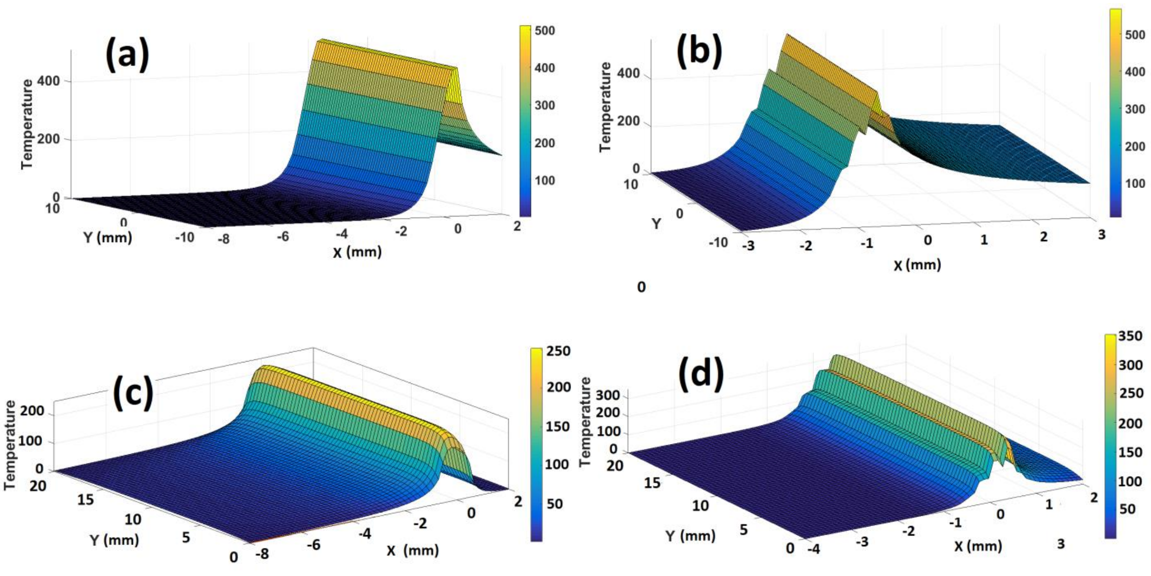

Figure 4-7 3D temperature profile of the workpiece in different cases: a) constant heat source in dry condition (adiabatic boundary conditions at walls) b) periodic heat source in dry condition c) constant heat source in wet condition (convective boundary condition at walls) d) periodic heat source in wet condition

It is also clear from the figure that considering a periodic heat source resulted in temperature profile with oscillating nature. The maximum temperature in case of using the periodic heat source was also higher compared to using a constant heat source both in dry and wet conditions. The rest of this section explains these results and discusses the influential parameters.

In order to compare the effect of the time-dependent heat source and boundary conditions the maximum temperature in a dimensionless form ($\frac{T_{max}}{T_{max\_2D}}$) on the vertical axis has been plotted against the cross-sectional position of the workpiece on the horizontal axis in Figure 4-7 a periodic triangular heat source was defined as $q_w(x,t) = \left(q_{qve} + 0.8 q_{ave} sin\,(2\pi(\omega)t\,)\right)\,\left(1 + \frac{2x}{lc}\right)$ to investigate the effect of heat source strength fluctuations. ω is the wheel revolution per second, and q_{qve} is the average of heat source strength which can be defined as:

$$q_{qve} = \frac{\varepsilon F_x . V_c}{2 l_c . b}$$

where F_x is the average grinding force in the feed direction.

$T_{max\ \_2D}$ in Figure 4-8 represents the simple 2D solution of the problem for a triangular heat source moving constantly in a semi-infinite workpiece which is commonly used in the literature for surface grinding. As it can be seen from Figure 4-8, the ratio of maximum temperature is equal to one in case of using a constant triangular heat source in dry condition where adiabatic boundary condition exists in all surfaces for the slab workpiece (brown line in the figure corresponding to equation 4-11). Furthermore, the maximum temperature is constant along the cross section implying that the 2D solution is valid and can be used without any difference from the 3D solution. Considering the time-dependent heat source and adiabatic boundary condition (blue line in the figure corresponding to equation 4-28), the maximum temperature is 7% higher than in the case with constant heat source. The model of Des Ruisseaux and Zerkle with a triangular heat source [116] (yellow line in the figure corresponding to equation 4-10) which considers the coolant convection effect on the top surface of the workpiece resulted in a maximum temperature equal to $0.37 T_{max\ \_2D}$. The solution is also 2D since the convection effect on the side walls of the slab has not been considered. When the convection effect from the side walls for a constant heat source is taken into account (green curve in the figure corresponding to equation 4-17), the maximum temperature near the sides are lower compared to the middle of the slab. However, the effect of cooling from the sides fades gradually while moving to the middle of the slab until there is no difference between maximum temperature at the middle of the slab and the maximum temperature developed by Des Ruisseaux and Zerkle [59]. The most accurate and comprehensive model is achieved by using the periodic heat source with convection from all surfaces of the workpiece (violet curve in the figure corresponding to equation 4-29) which results in a higher maximum temperature compared to the constant heat source model.

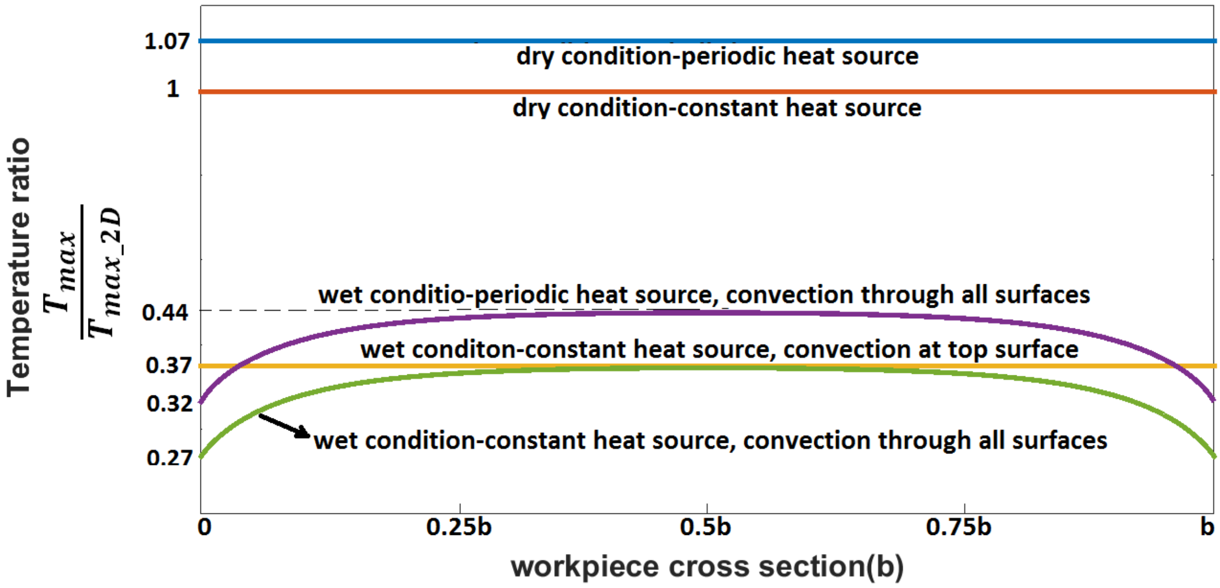

Figure 4-8 maximum temperature of the workpiece along the cross section of the workpiece considering different boundary conditions and different heat source for a bearing hardened steel workpiece material, coolant convective factor h=0.07 W/mm²K, b=10mm, L=0.23

Figure 4-9 shows the 2D temperature profiles of the slab in feed direction along the middle of the slab at different depth below surface (z) considering a constant and periodic heat source. The red curve represents the temperature profile of the slab for a constant heat source at surface($z = 0$) while the other curves show the temperature profile for a periodic heat source at different depths below the surface. As it can be seen from the figure, the temperature fluctuations at the workpiece surface are strong near the heat source and faded far from the heat source indicating both constant and periodic heat source provide the same solution at points far from the heat source position (see red and blue curves in the figure). Fading in the temperature fluctuation can also be seen by moving away from the workpiece surface. This can be explained by considering thermal time constant. Generally, depending on the thermal properties of the workpiece material and its geometry, some time is required for the heat to reach a position that has a distance from the heat source. Accordingly, as the distance from the heat source is increased the fluctuations are sensed weaker until far from the heat source the effect of heat fluctuation is completely faded.

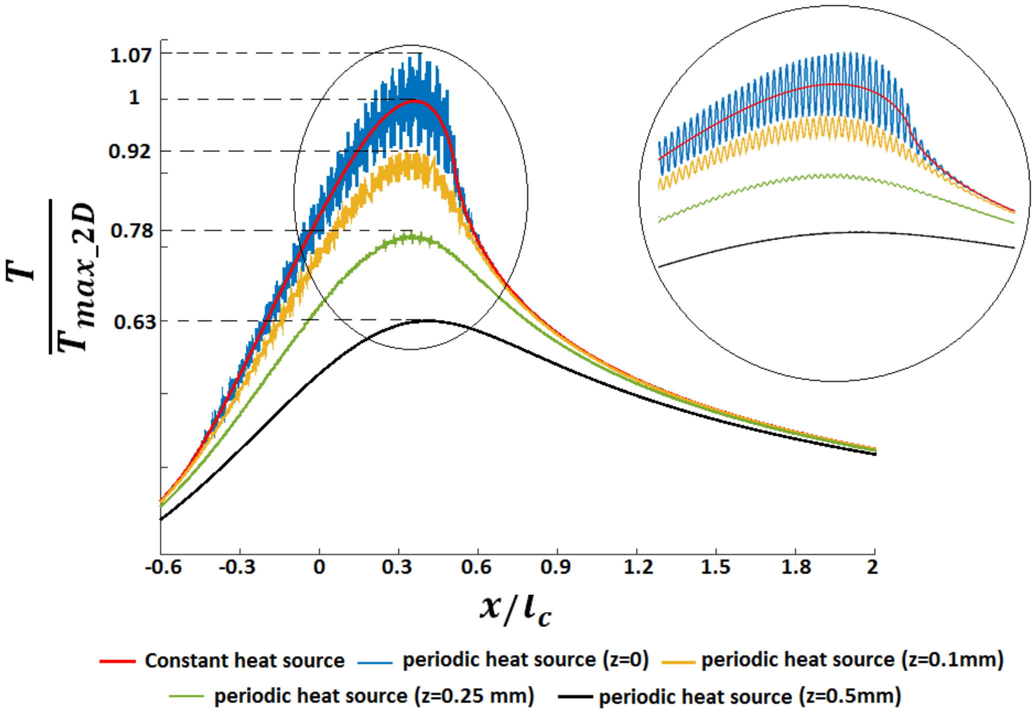

Figure 4-9 temperature profiles of the slab in feed direction along the middle of slab considering different heat sources for a bearing hardened steel workpiece material at different z levels

Based on the results obtained here, it can be concluded that considering a time-dependent heat source resulted in higher maximum workpiece temperature compared to a constant heat source. The magnitude of the increase directly depends on the amplitude of grinding force fluctuations. To investigate this factor, four heat sources with different amplitudes but a same average strength were considered as follows:

$$q_w(t) = (q_{ave} + aq_{ave}sin\,(2\pi(\omega)t\,)) \qquad (4-30)$$

where, a represents the fluctuation of the heat flux being set as 0, 0.3, 0.6 and 1 respectively. Figure 4-10a shows the corresponding heat flux in one wheel's revolution and in Figure 4-10b the effect of these heat fluxes on the maximum temperature has been shown. T_{max} in Figure 4-9b corresponds to the maximum temperature for the constant heat source ($a = 0$). As it can be seen from the figure, by increasing the amplitude of heat flux vibration the maximum temperature increases, too.

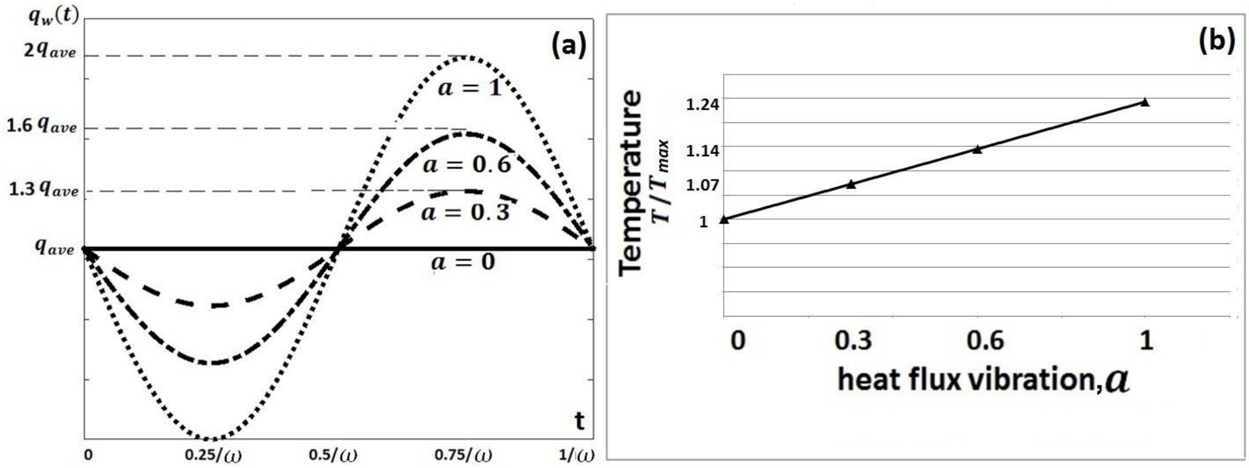

Figure 4-10 Effect of heat source fluctuation on the maximum temperature a) heat source profile for 1 wheel revolution, b) maximum temperature corresponding to each heat source at wet grinding condition, h=0.07 W/mm²K, L=1.4

4.3.2 Effect of Workpiece Width

The length of the workpiece width is an influential parameter that can distinguish the 3D solution from the 2D one. Generally, the effect of convective boundary conditions from the workpiece sides is faded by moving towards the center. In a slab workpiece with a long width, both 2D and 3D solutions provide approximately the same maximum temperature in the center. However, for a workpiece with small width, the 3D solution should be considered. This effect is illustrated in Figure 4-11 using the thermal properties of bearing steel material as the workpiece and a water-based coolant (h=0.07 W/mm^{2}K). The vertical axis shows the temperature respect to the maximum temperature in the 2D case. As it can be seen for a slab workpiece having 2mm width, the maximum temperature in the center is approximately 89% of that in the 2D condition. This value increases to around 99% when the width increases to 8mm. Accordingly, the 2D solution can be used to predict the maximum temperature of the workpiece with very good approximation when the width of the workpiece is more than 8mm for this material and coolant pair.

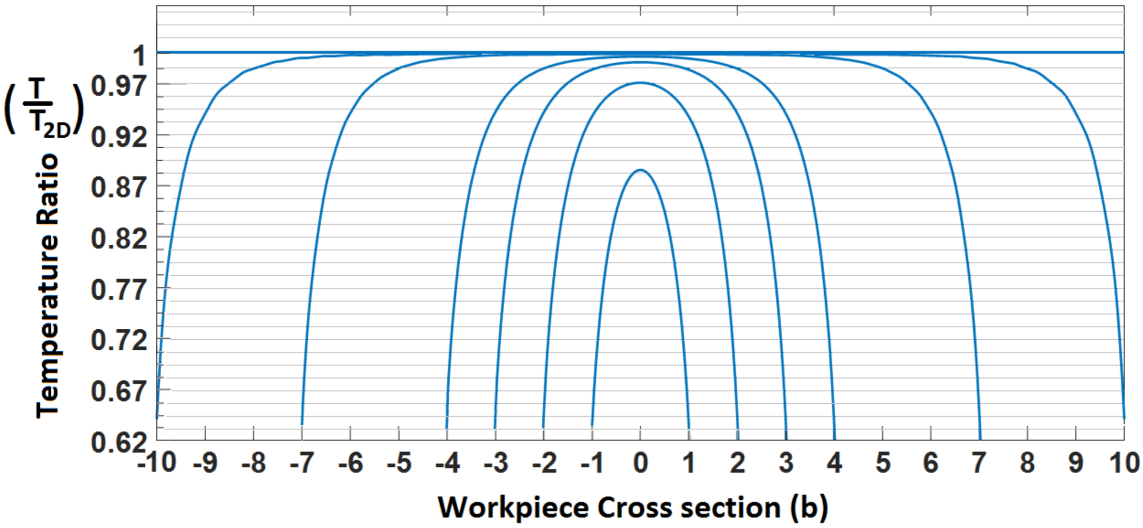

Figure 4-11 Temperature distribution along the cross section of the workpiece considering different workpiece width considering bearing hardened steel workpiece material, coolant convective factor h=0.07 W/mm²K, L=0.97

4.3.3 Coolant effect

The effects of using different coolants on the maximum temperature can be investigated by the model as well. The convection coefficient of the coolant is one of the important parameters for the maximum workpiece temperature in wet condition. Thermal and physical properties of the coolant, wheel-workpiece contact length and wheel speed affect the convection coefficient [2]. Nozzle shape, fluid speed and pressure are also influential parameters to deliver the coolant effectively in the grinding zone. Accordingly, a wide range of experimentally identified convection coefficients have been reported in the literature [2]. Figure 4-12 shows the cooling effect of the dimensionless convective heat transfer coefficient (H) on the temperature distribution along the width of the workpiece .The vertical axis shows the temperature relative to the dry condition (T_{dry}). As can be seen from the graph, a higher convective coefficient resulted in a larger temperature drop in the workpiece material. Using a coolant corresponding to $H = 0.125$ resulted in maximum workpiece temperature approximately 0.57 T_{dry}, while using a coolant with $H = 1$ resulted in temperature equal to 0.28 T_{dry}. In regards to using the model in wet condition, it should be noted that the maximum temperature should not exceed the boiling temperature of the coolant, otherwise the convective coefficient factor should be considered as zero and the calculation must be repeated in accordance with dry condition [30].

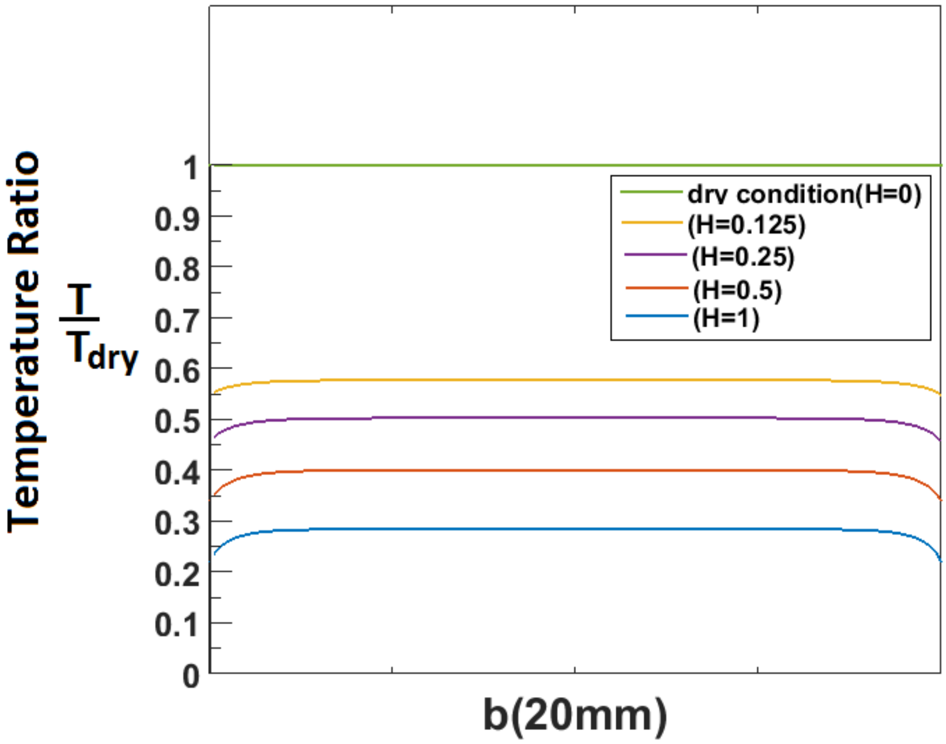

Figure 4-12 Effect of cooling convection factor on temperature of the bearing steel workpiece slab, L=0.98,

4.3.4 Effect of the Grinding Wheel and Grit Properties

Grinding wheel properties and grit characteristics have a great effect on workpiece temperature, too. More power is required to cut a specific volume of the workpiece material when a worn wheel is used. This can be explained by considering the grit characteristics and the active number of grits. In order to see these effects a specific grinding wheel was considered and the maximum workpiece temperature at its different life stages can be predicted. Figure 4-13 shows the tangential grinding force and temperture for a specific CBN electroplated wheel when it is fresh, trued and worn. As it can be seen in Figure 4-13, the workpiece temperature increases when the fresh wheel is dressed or worn. The rate of increase in the workpiece temperature is proportional to the rate of increase in the tangential force. In other words, contribution of grinding wheel and grit properties on the workpiece temperature is through the heat source (changing the tangential force). Dressing and wheel wear change the properties of the grit. The dressing process makes the grit height distribution smoother and more grits will be active. Similarly, the active number of grits increases further in the case of a worn wheel. Increasing the active number of grits resulted in higher grinding force. In case of the worn wheel due to attritious wear the clearance angle tends to be decreased making high ploughing and rubbing forces. As a result, the tangential force incresese considerably compared to using fresh or dressed wheel.

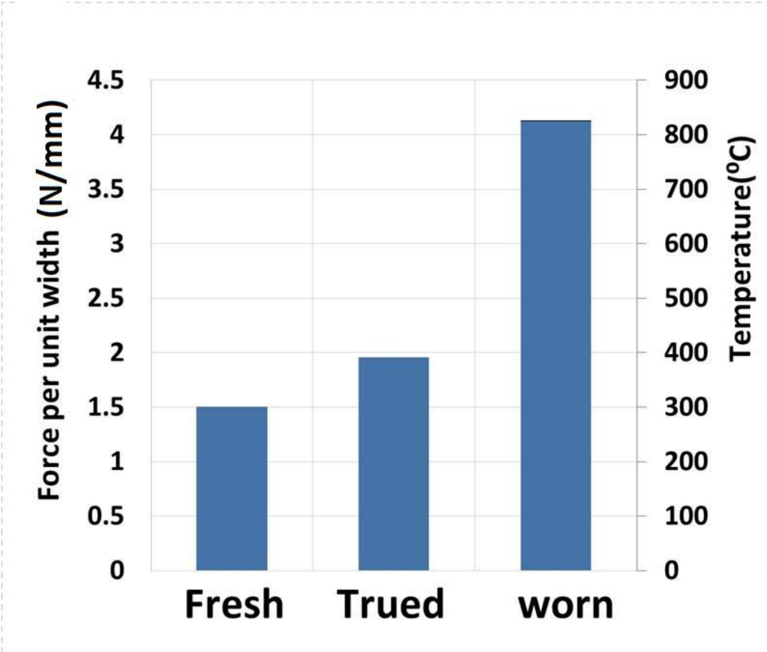

Figure 4-13 Tangential Grinding force per unit width and Temperature for Inconel 718 workpiece material using a CBN electroplated wheel in fresh, trued and worn conditions, depth of cut 20 µm, feed rate 2800 mm/min, cutting speed 15m/sec ,run out 10 µm

5 Surface Burn Model

5.1.1 An Introduction of Surface Burn in Grinding

Surface burn is a very important concept in grinding processes and different studies concentrated to study different aspect of this problem. Based on what has been discussed mostly in the literature survey in the first chapter, the conditions for burn occurrence mostly studied for steel alloys. In addition, there is not a single burn criterion which directly targets the main cause of the surface burn i.e. oxidation process. Furthermore, considering eutectoid temperature as the burn threshold is a high estimate, on the other hand, tempering temperature as an underestimate value is not constant since temperature and time are interdependent variables in the tempering process [89]. Accordingly, the temper burn cannot be related to a specific critical temperature. Above all, considering a critical temperature to avoid surface burn is not an accurate approach. As it was discussed, the surface burn occurs as a result of the oxidation process and theory of metal oxidation at high temperature in which both temperature and time are influential parameters should be employed to understand the burn behavior in the abrasive processes. It is worth mentioning that, the thickness of the surface burn layer cannot be obtained by using current thermal models in which a constant temperature threshold is defined as the burn limit.

In this thesis the aim is to increase the current knowledge on the surface burn by developing a burn model applicable for all workpiece materials. Not only the occurrence of the burn can be predicted but also the thickness of the burn layer will be obtained in this model. Knowing the depth of the oxide layer is a matter of great importance in industrial production since it gives the production and quality control engineers an insight to evaluate the quality of the products more properly. A few microns of surface burn may be removed at the end of the grinding cycle or in the polishing process provided that other surface defects are absent.

5.1.2 Burn Model

Any interaction between grits on the grinding wheel with the workpiece creates a force pulse and summation of those pulses creates the total grinding force. Almost all of the required energy to remove the material in grinding converts to heat where significant portion of it goes to the workpiece. While the temperature model in the literature can predict the workpiece temperature during heating and cooling, maximum workpiece temperature have been used as a critical temperature to prevent surface burn. The original contribution of the current burn model is considering the temperature profile of the workpiece instead of a single point temperature (maximum temperature). The developed temperature model in this thesis is used as part of the burn model since it considers the time-dependent feature of the heat source and provides temperature profile of the workpiece during heating and cooling. In addition, the maximum workpiece temperature can be obtained more precisely.

As it was mentioned in the literature survey the surface burn refers to many thermal damages which are not necessarily surface burn. If it is defines as the chemical reaction between oxygen the metal (oxidation), theory of oxidation at high temperature must be implemented to study this phenomenon. When the temperature in the workpiece rises, the metal oxidation accelerates where the oxidation rate depends on the oxidation temperature and time. Accordingly both maximum temperature and the period in which the metal expose to the oxygen at high temperature come into play to study surface burn. The most common way to investigate the oxidation rete is measuring the weight of metal samples during oxidation process [117] and by knowing the density of metal and metal oxide the thickness of the oxide scale can be found[118].

Finding the rate of oxidation is very important to understand the burn behavior in grinding. There are different oxide rate growth including linear, parabolic and logarithmic laws observed experimentally and explained by different oxidation mechanisms [119]. Generally, after formation of a very thin layer of metal oxide in nano scale on the surface of the metals under logarithmic law, the oxide layer starts to grow linearly proportional to the time independent of the scale thickness. In this case, the oxidation takes place by surface or phase boundary reactions [119]. After formation of a thick layer of oxide (0.4 to 0.5 mm), the rate of oxidation reduces and follows a parabolic law in which the rate of the oxide formation depends on the thickness of the scale[118]. Based on these oxidation rates, it can be assumed that the surface burn in grinding process follows a linear law since the metal oxidation is at initial stage and the burn layer is in micro scale. Accordingly:

$$\frac{dh}{dt} = k \qquad (5-1)$$

where h is the thickness of burn layer, t is the time of oxidation. k is constant rate which is dependent to temperature and can be empirically stated by Arrhenius equation:

$$k = Aexp\left(\frac{-Q}{RT}\right) \qquad (5-2)$$

where A is a constant, Q is activation energy and R is the gas constant.

Considering the temperature profile of the workpiece which is varying with time, the depth of the burn layer is calculated as:

$$h = \int_0^t k.\,dt \; = \int_0^t Aexp\left(\frac{-Q}{RT}\right)dt \qquad (5-3)$$

t is the exposure time defined as the period between the start of the workpiece temperature rise and dropping back to the room temperature. T is the workpiece temperature obtained from equation 4-28.

It should be mentioned that workpiece temperature across the burn layer at a specific time is not constant. Maximum temperature occurs at the workpiece surface and decreases exponentially with z level according to equation 4-28. However, considering the fact that the thickness of the burn layer is in micro scale and the maximum temperature change is negligible across the layer, surface temperature can represent the temperature profile of the workpiece across the burn layer. If the temperature gradient was not negligible for very thick burn layer, upper band and lower band solutions approach can be used instead. These situations have been shown in Figure 5-1. As it has been mentioned in real situation (Figure 5-1 a) there is a temperature gradient across the burn layer and the temperature at the top surface of the workpiece is higher than the temperature at the bottom surface (T_{h_real}). If this temperature gradient is not negligible upper band and lower band solutions are suggested. Upper band solution is a solution in which the predicted burn thickness is bigger than the burn layer in real situation. In the upper band solution, it is assumed that the temperatures beneath the workpiece surface are the same as the surface temperature (Figure 5-1 b). The burn layer thickness obtained by this assumption is the overestimate solution. The lower band solution is a solution in which the predicted burn thickness is lower than the burn layer in real situation (Figure 5-1 c). In the lower band solution, the temperature value at the burn depth, obtained from the upper band solution, is calculated from equation 4-28. The temperature at burn depth is lower than the temperature at the workpiece surface and the burn depth is calculated corresponding to this new temperature. The lower band solution gives the underestimate solution of the burn depth. The real burn thickness is between the lower band and upper band solutions.

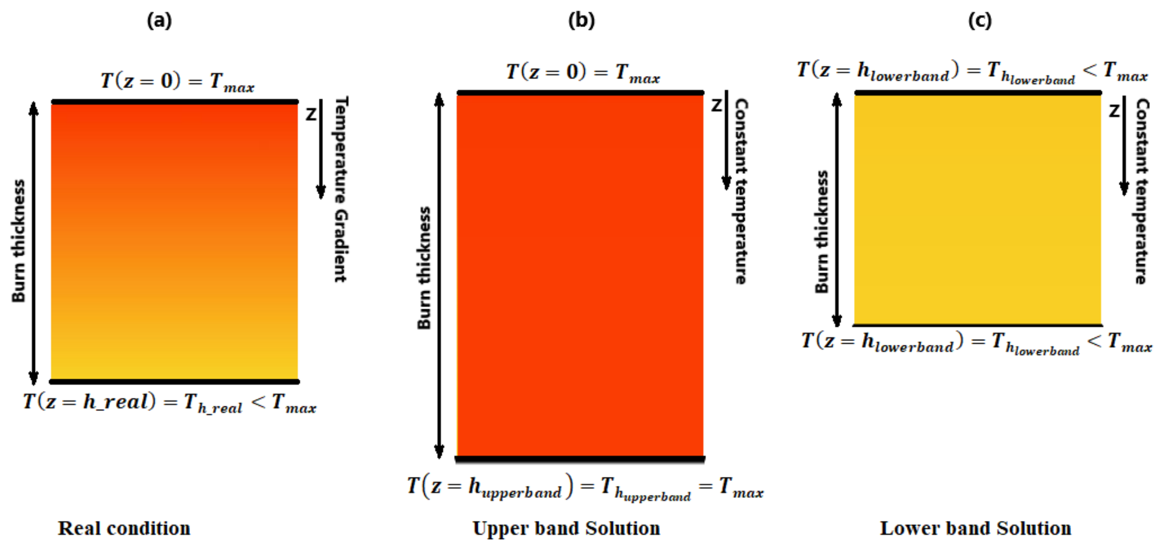

Figure 5-1 Upper band and lower band solutions in case of not negligible temperatrue gradient

Oxidation rate coefficients i.e. A and Q in equation 5-3 should be known in this solution. These data can be obtained experimentally in an oxidation test where the scale grows linearly. However, most of the published data have concentrated on iron-based alloys as the work material and more attention was placed on the last stage of the oxidation where the oxide scale starts to grow based on the parabolic law. Furthermore, the laboratory experiments were carried out under stagnant gas at lower oxygen concentration compared to air [118]. However, increased air velocity on the surface of the workpiece due to the wheel rotation can accelerate the oxidation process profoundly[120]. In order to find the proper constants, the approach used in [120] which included the oxygen concentration and air velocity in the model and experiments was adapted in this study. Considering the wheel rotational speed in grinding as the air velocity and oxygen concentration (21% at room temperature), Q and A were considered as 17 KJ and 1.85 µm/sec, respectively in this thesis.

.

The procedure to obtain the burn thickness starts with the calculation of the workpiece temperature. Wheel and workpiece thermal properties, grinding conditions and heat source strength are some of the inputs required to calculate the workpiece temperature during heating and cooling in equation 4-28. By knowing the workpiece temperature during heating and cooling periods, and the oxidation constants, the depth of burn layer is calculated numerically from equation 5-3. According to the equation 5-3 two parameters i.e., both the exposure time *p*, and the workpiece temperature affect the thickness of the burn layer. Long exposure time and high workpiece temperature increase the risk of surface burn according to Figure 5-2. Burn thickness increases linearly with exposure time as can be seen from figure 5-2. The growth rate also increases with the maximum temperature.

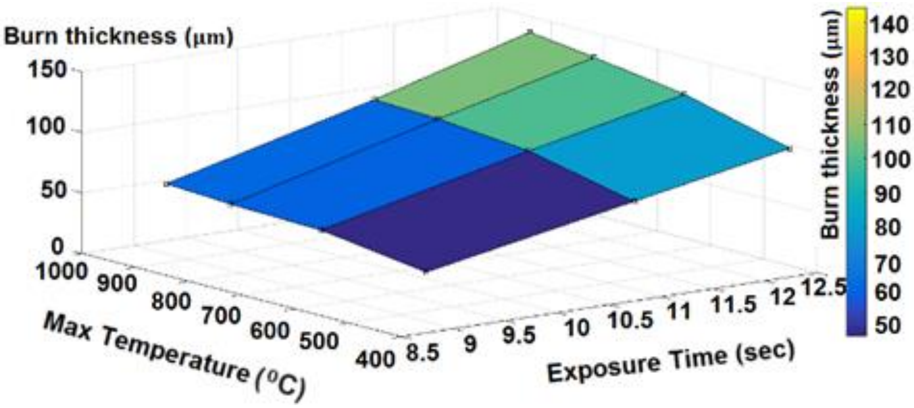

Figure 5-2 Burn thickness vs. exposure time and maximum temperature for AISI 52100 workpiece material and aluminum oxide wheel.

Experimental setup, procedures and validation of burn model has been presented in the next two chapters.

6 EXPERIMENTAL VERIFICATIONS OF THE PROPOSED MODELS

In this chapter, different experimental setups, procedures, methods and devices that have been used in this thesis to validate the proposed models is presented. Identification of the characteristics of the grinding grits is a must for developing every grinding model. Unlike the other cutting tools that the geometry of the cutter is completely known, the grinding wheel composed of many grits that randomly distributed on the wheel with different geometrical shape. In chapter 2, the method of discretization was developed and based on the grit height, width and other properties the grinding wheel was modeled. According to the geometrical-kinematic model, grit height distribution, cutting angles, size and edge radius are all influential parameters that should be known or measured beforehand. The experimental measurements and the modeling method are discussed in this chapter.

By developing the kinematic equation, grits trajectories were identified and based on the method developed in Chapter 2 the workpiece surface topography weas predicted. Workpiece surface roughness has been measured and compared with the model prediction to serve as the validation of the kinematic-geometrical model.

Grinding force was modeled in Chapter 3 whereas in this chapter the experimental setup and data are presented to validate the force model.

Finally, the temperature and burn model are validated by using embedded foil thermocouple and investigation of the cross section of the ground samples.

6.1 Surface roughness measurement

A 3D confocal microscope (μsurf NanoFocus) was used to identify the wheel properties and the workpiece surface after the grinding operation in order to verify the geometrical-kinematic model. Through the use of light scanning and taking a very high resolution image at different focal heights and reconstructing those images by its software, the microscope produces an exact three-dimensional image of the sample surface. The grit properties such as grit width, height and width of cut were measured by µsoft analysis software (https://www.nanofocus.com/products/usoft/analysis/). Figure 6-1 shows the microscope and the apparatus providing 360° access to the wheel without unloading the wheel. SEM microscope also was used in different occasions to see the grit in more detail to measure the edge radius of the grit or sticking material as dead metal zone.

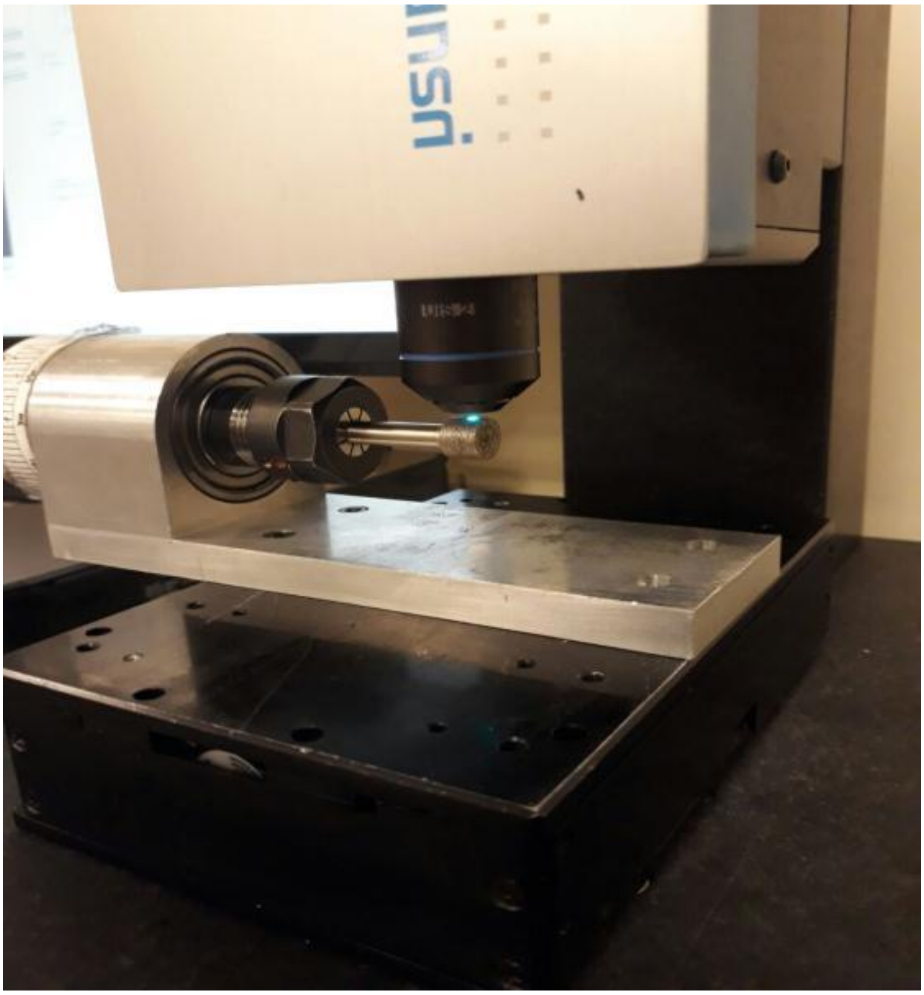

Figure 6-1 µsurf NanoFocus microscope and apparatus enable 360 ° access to the wheel

Required parameters i.e. height, width of grits and width of cut were measured with the microscope. The parameters were obtained by measuring a large number of individual grits for each specific wheel (see Figure 6-2). C Number (number of grits in 1 mm^2) was obtained by counting the number of the grit and dividing it to the area provided by a 20x magnifier lens. More than 100 areas were selected randomly to measure this number. Other parameters including width of grit, width of cut and grit height were measured with 50x magnifier lens. Figure 6-3 shows the lenses used in this thesis.

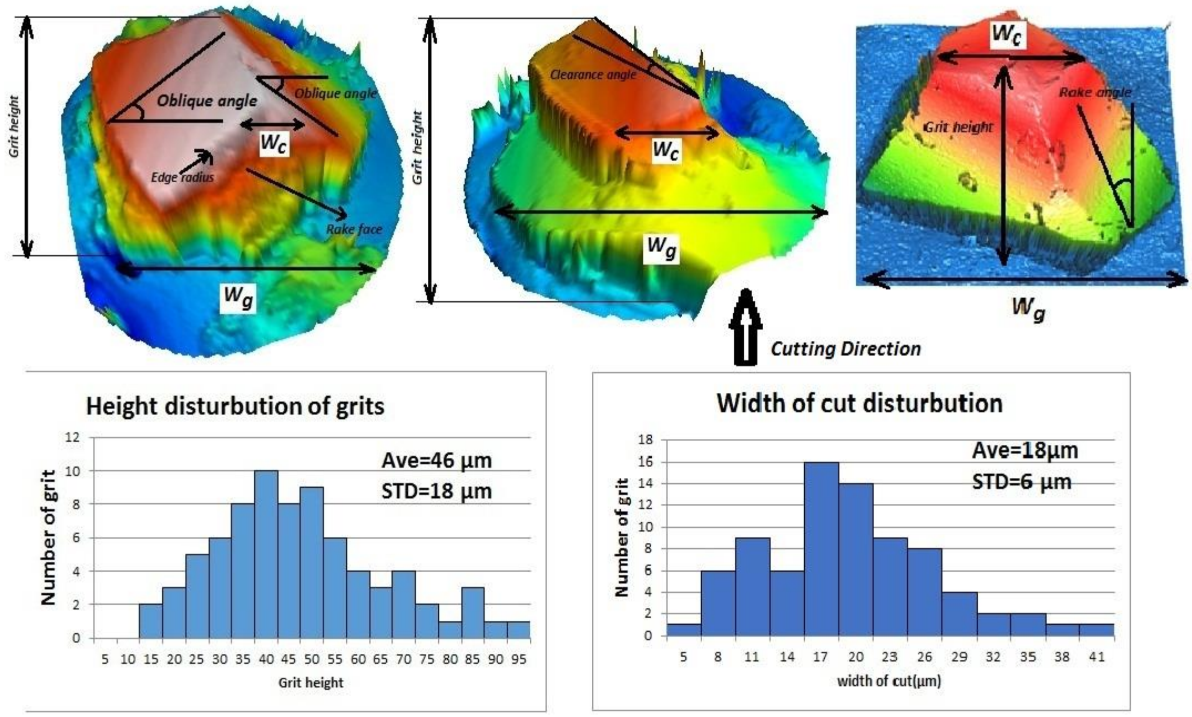

Figure 6-2 some grit picture and relevent geometric parameters along with hight and width of cut distribution as two main parameters for kinematic-geometrical model

Figure 6-3- 50x and 20x Olympus lens to extract grit geometrical properties

After measuring grit heights and width of cutting edges, the average and standard deviation of those variables are calculated. In previous studies, a normal distribution was used for simulation purposes.

Different CBN wheels were measured in this manner to obtain the required data for the model. It should be noted that wheel measurement is a tedious and time-consuming task and the measurements should be done accurately. This fact is one of disadvantages and limitation of the model which should be modified or improved in later studies.

Figure 6-4 to 6-8 show some sample grit measurements along with the parameters required in the model and workpiece surface after grinding.

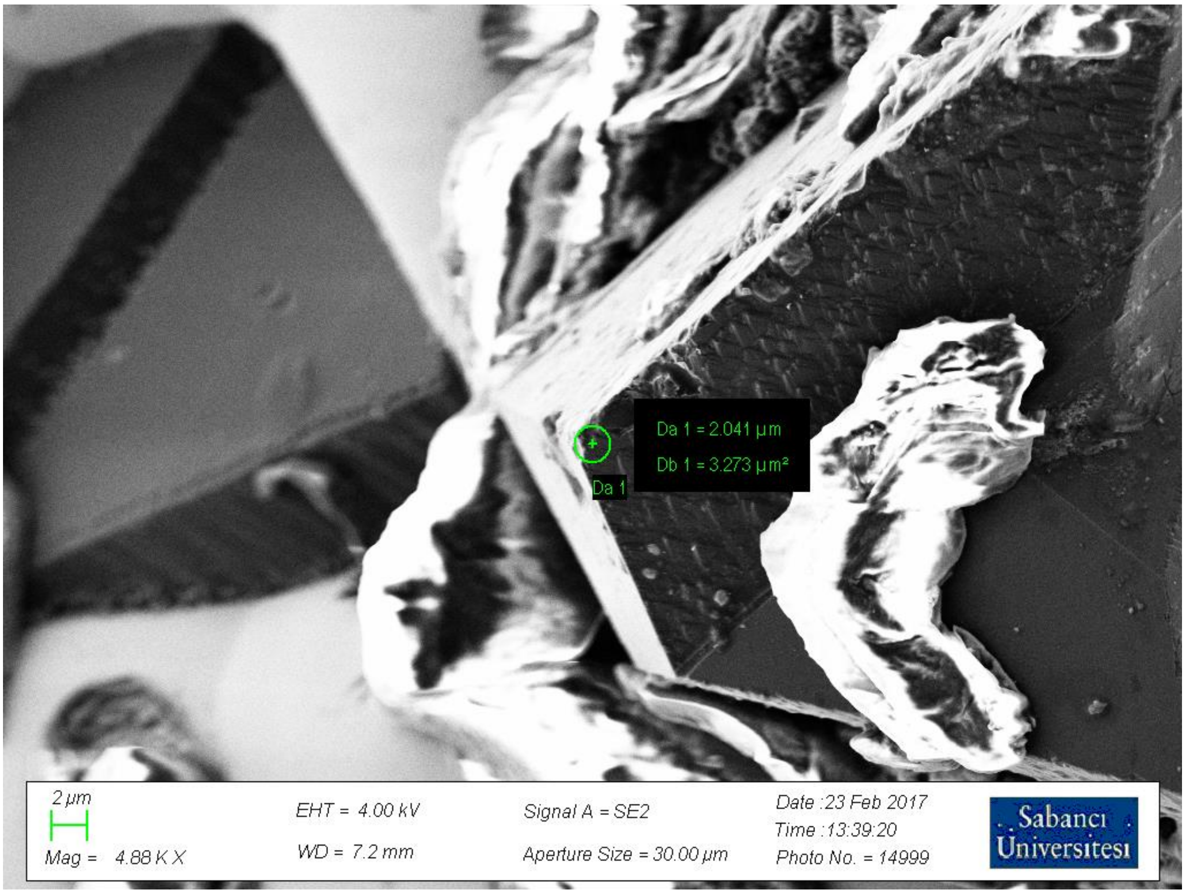

Figure 6-4 SEM photo of a grit showing the edge radius

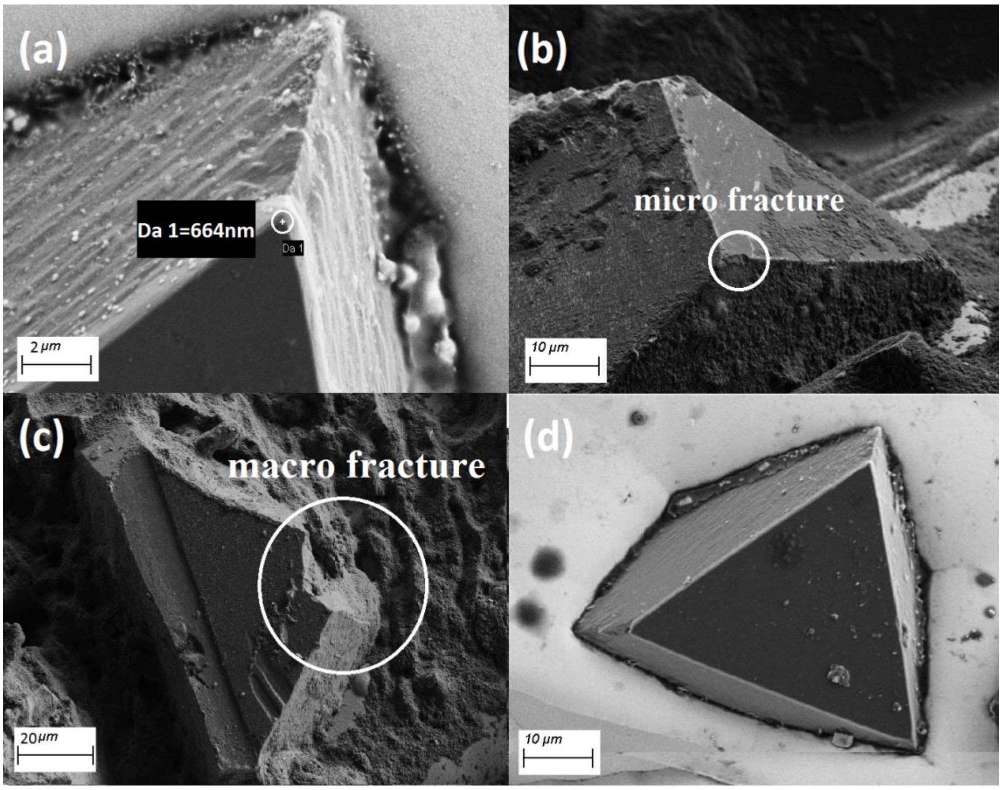

Figure 6-5 SEM photos of single CBN grits, a) a sharp grit with edge radii of 0.6 µm, b) fracture wear at the tip, c) fracture wear changing the clearance angle, d) grit with a flat surface

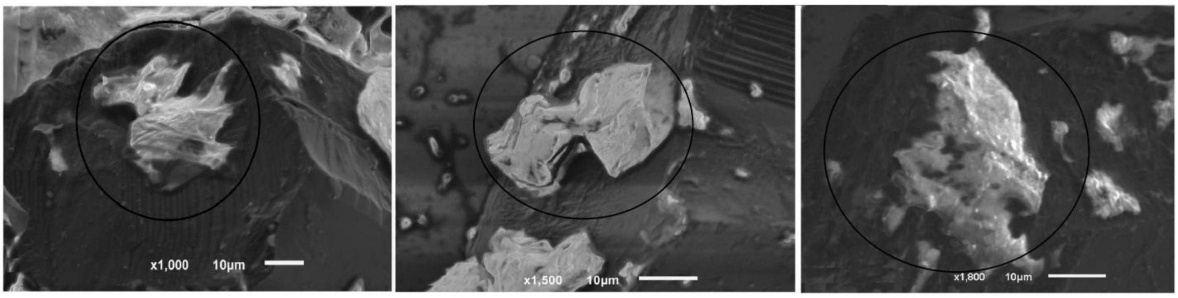

Figure 6-6 SEM photos of CBN grits with sticking material on the rake face

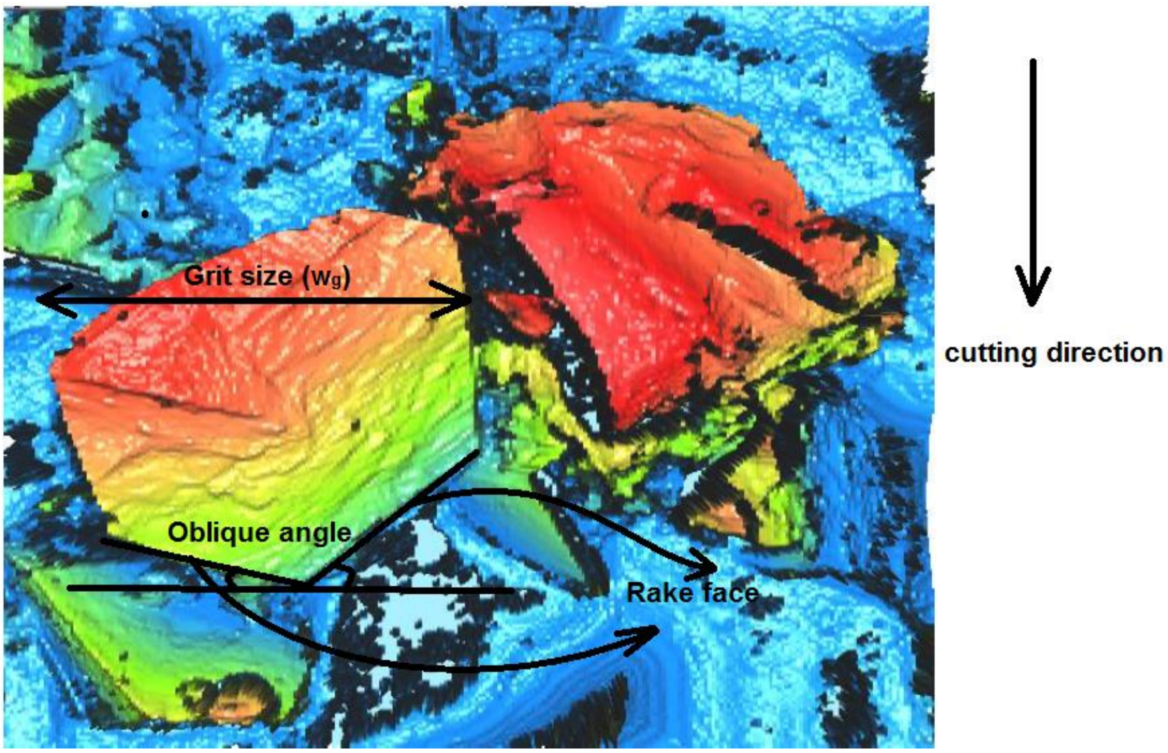

Figure 6-7 2D veiw of the grit (top view) grit size and oblique angles can be identified easily from this veiw

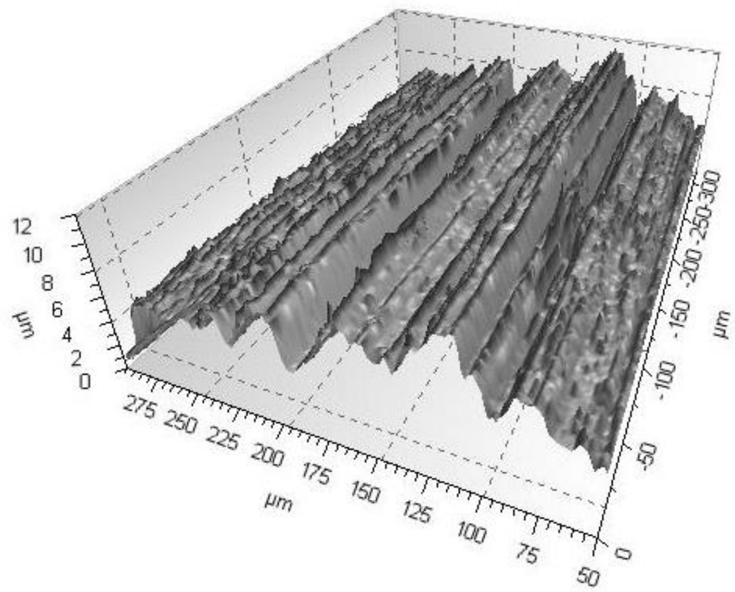

Figure 6-8 workpiece surface after grinding

Table 6-1 shows the results of grit analysis for 5 different CBN wheels. The information extract from grit measurement is used as an important input in the models.

Table 6-1 Wheels characterization

Wheel number	1	2	3	4	5
General description	CBN electroplated	CBN electroplated	CBN electroplated	Trued CBN electroplated	Worn CBN electroplated
Diameter (cm)	10	5	30	10	10
Static number of grits	33	97	23	33	31
Grit width (µm)	65	41	73	67	39
Grit size(µm)	126	64	151	126	126
Average girt edge radius (µm)	1.15	1	1.07	1	1.37
Mean and standard deviation of girts height (µm)	46 & 18	30 & 11	88 & 17	37 & 8	25 & 3.2
Mean and standard deviation of width of cuts (µm)	18 & 6	9 & 4	23 & 11	17 & 7	16 & 7

6.2 Force Measurement

Surface grinding experiments were performed on a Chevalier-Smart-H/B818 type Grinding CNC machine (https://www.chevalierusa.com/conversational-cnc-surface-profile-grinder-SMART-H-B818.html)to validate the force model. A Kistler 9129AA table type 3-axis dynamometer was used to measure the grinding forces. Wide ranges of grinding conditions and wheels listed in Table 6-1 were chosen to evaluate the model validity and accuracy. The wheel run out was measured for each wheel with a dial indicator having 1 µm precision. Inconel 718 and bearing steel (AISI52100) were two workpiece material used in this thesis in force and temperature model. Figure 6-9 shows the experimental setup for evaluation the force model.

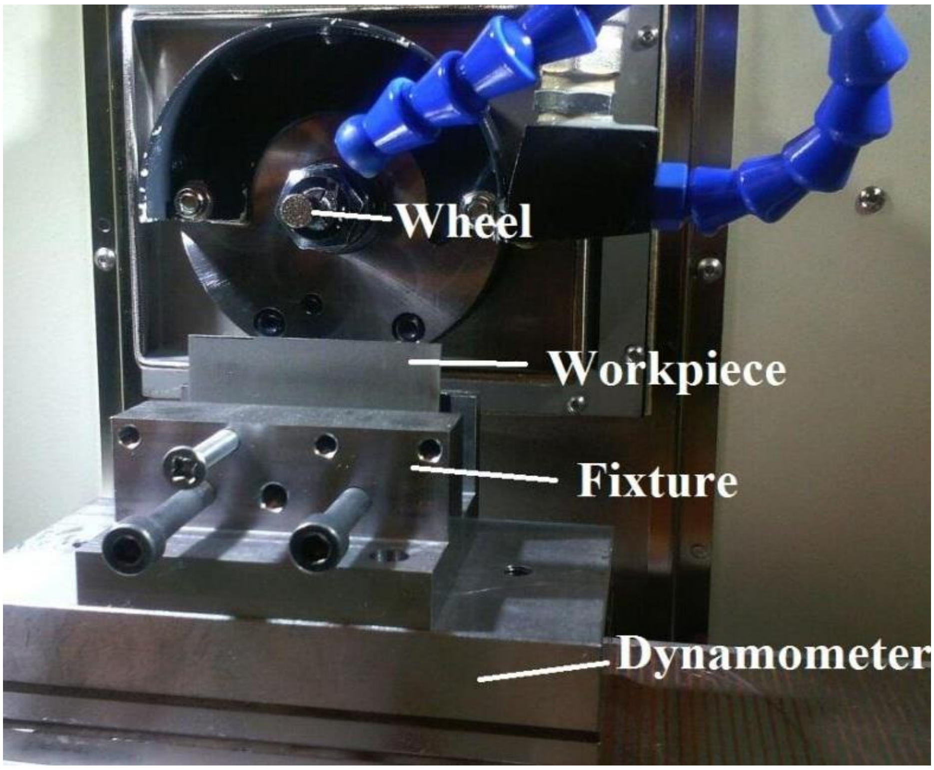

Figure 6-9 Experimental setup for force model verification

The Johnson-Cook constant parameters for the Inconel-718 workpiece material used in this study have been reported in Table 6-2 according [121]

Table 6-2 Johnson-Cook material model constants for Inconel 718

Johnson-Cook constants	A	B	C	n	m
Value	1485	904	0.015	0.777	1.689

Aside from the workpiece's material properties, the sliding friction coefficient between CBN grits and workpiece material as a function of chip velocity is required in force calculation. The sliding friction coefficient was obtained experimentally at different cutting speeds by measuring the rubbing and normal force. The ratio of the rubbing to the normal force was recorded as the sliding friction coefficient after the grinding wheel approached vertically to the workpiece surface and touched the surface. Figure 6-10 shows the relation between the cutting speed and the ratio of sliding to normal force. The following linear equation was obtained and used as the behavior of friction coefficient in this study:

$\mu = 0.148 + 0.0061V_c$

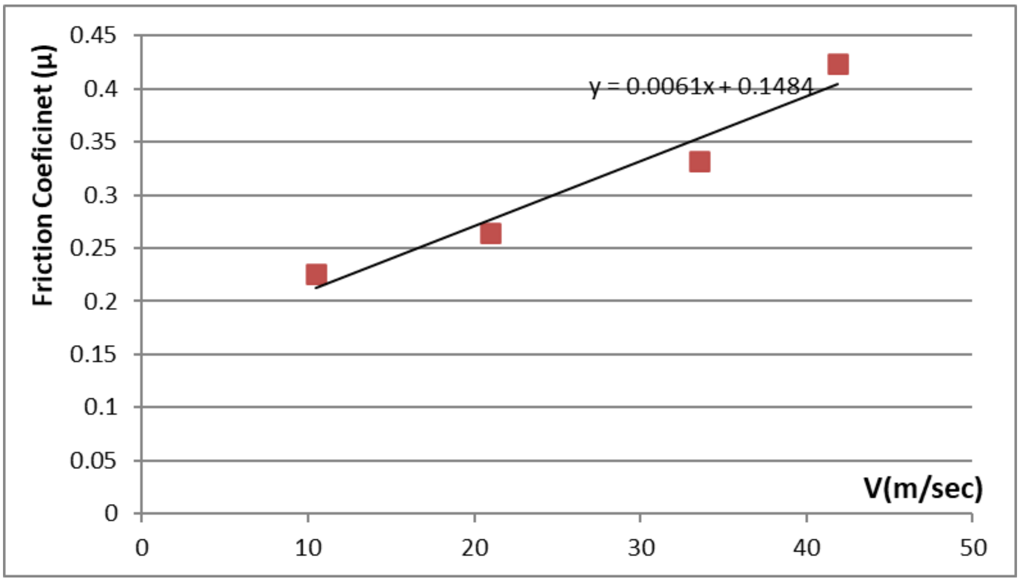

Figure 6-10 Relation between sliding coeficient of friction and cutting speed

6.3 Temperature Measurement

Different methods have been employed in literature to measure the workpiece temperature including optical techniques using a thermal camera [61], infrared detector [72] and different thermocouple techniques [122]. Batako et al. [123] reviewed these methods and showed that using foil thermocouples in a split workpiece provides the most accurate and reliable signal. This method was adopted in this thesis by using a double-pole, K-type foil thermocouple (OMEGA 88309k) with the initial thickness of 100 µm. This specific model was selected since K type thermocouple provides a reliable and accurate signal in a wide range of temperatures and it had the minimum available thickness among other available thermocouples. In order to obtain a better signal quality, the thermocouple pole tip was split apart and every pole was rubbed to reduce the thickness down to as small as 10-15µm where both poles were positioned over each other and fixed between two polished surfaces of the split workpiece. Figure 5-9 shows the experimental setup and devices. It is worth mentioning that the grinding force can be predicted according to the force model; however, in order to evaluate the effect of considering the periodic heat source instead of a constant heat source and compare the results with the experimental data, the grinding force was measured experimentally to be used in the thermal model to evaluate the temperature model itself. A data acquisition device from Measurement Computing Corporation (DT9805) having the frequency of 50 KHz coupled with QuickDAQ software was used to collect temperature data. As it can be seen in Figure 5-9 a jaw was used to create a longitudinal preload force to assure full contact between the workpiece and the thermocouple. The full contact can be seen in Figure 6-11 where the thermocouple junction has been shown in a larger magnification view. Both dry and wet grinding tests using water-based coolant with 5% oil were performed in different conditions to validate the model. The thermal properties of the coolant, the wheel and the workpiece are listed in Table 6-3 to 6-5.

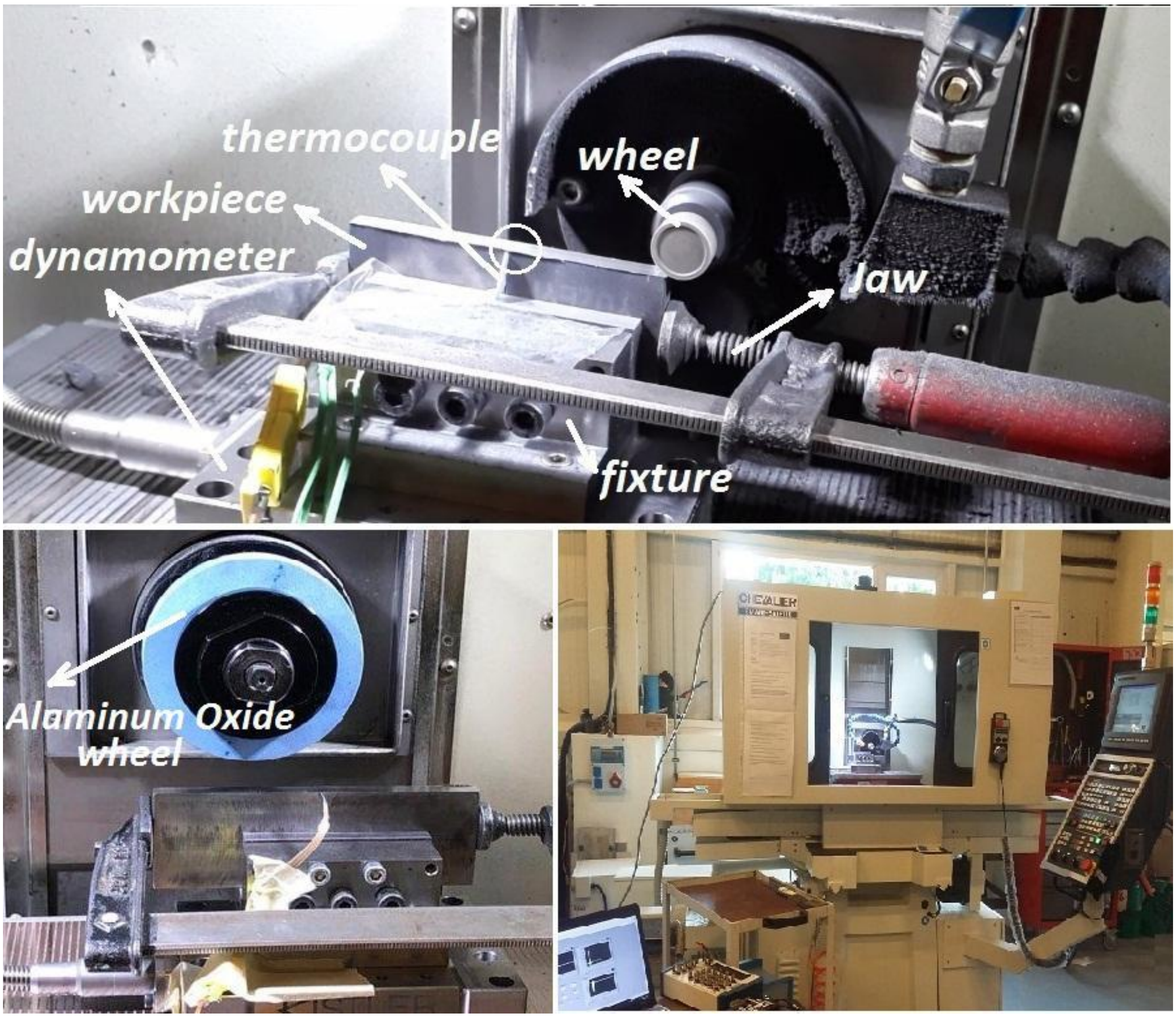

Figure 6-11 Experimental setup and devices for temperature model verification

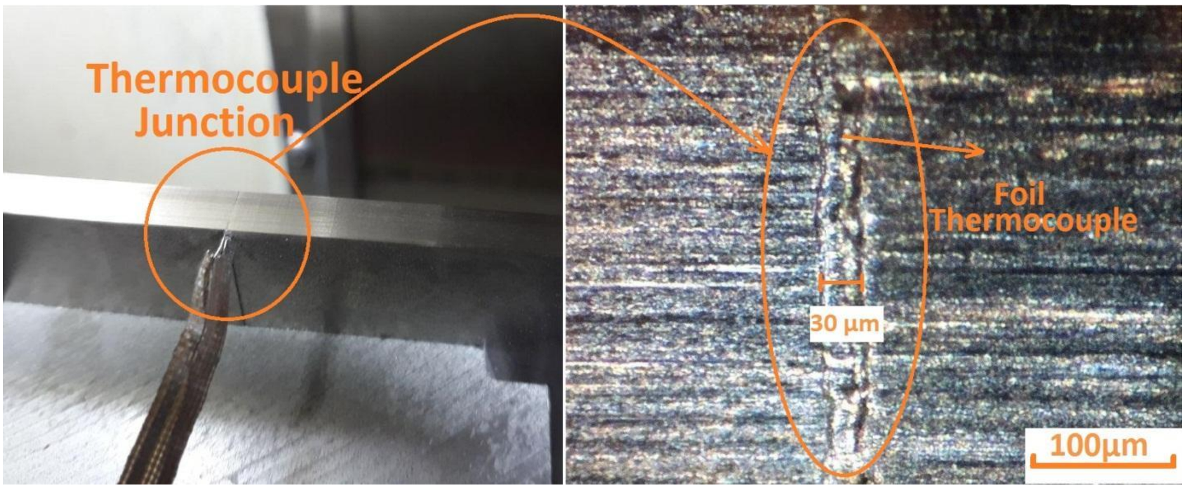

Figure 6-12 Thermocouple junction

Table 6-3 Thermal and physical properties of the coolant

coolant	ρ_f (Kg/mm^3)	k_f (W/mm K)	η_f(N s/m^2)	c_f (J/Kg K)
Water-based 5% oil	$1*10^{-6}$	$0.56*10^{-3}$	0.001	4200

Table 6-4 Thermal and geometrical properties of the wheel

Wheel type	Diameter (mm)	r_0 (µm)	k_g (W/mm K)	c_g (J/Kg K)	ρ_g (Kg/mm^3)
Electroplated CBN	20	0.023	240×10^{-3}	506	3.48×10^{-6}
Aluminum Oxide	100	0.037	35×10^{-3}	765	3.98×10^{-6}

Table 6-5 Thermal and physical properties of the workpiece material

Workpiece material	Hardness (HRC)	k_w (W/mm K)	c_w (J/Kg K)	ρ_w (Kg/mm^3)
52100 Bearing steel	60	$46.6*10^{-3}$	475	$7.81*10^{-6}$

6.4 Surface Burn Measurement Experiment

In order to verify the model, grinding tests were carried on a Chevalier-Smart-H/B818 type Grinding CNC machine using an aluminum oxide wheel with a diameter of 100mm (550A-120-I-10-165-V). Tests performed on hardened bearing steel (AISI52100) at different depth of cuts and feed rates while grinding force and temperature were monitored using a Kistler 9129AA table type 3-axis dynamometer and K-type foil thermocouple (OMEGA 88309k), respectively. Figure 5-11 shows the setup used in the experiments. Data acquisition device (DT9805) and QuickDAQ software were used to observe the temperature profile of the workpiece.

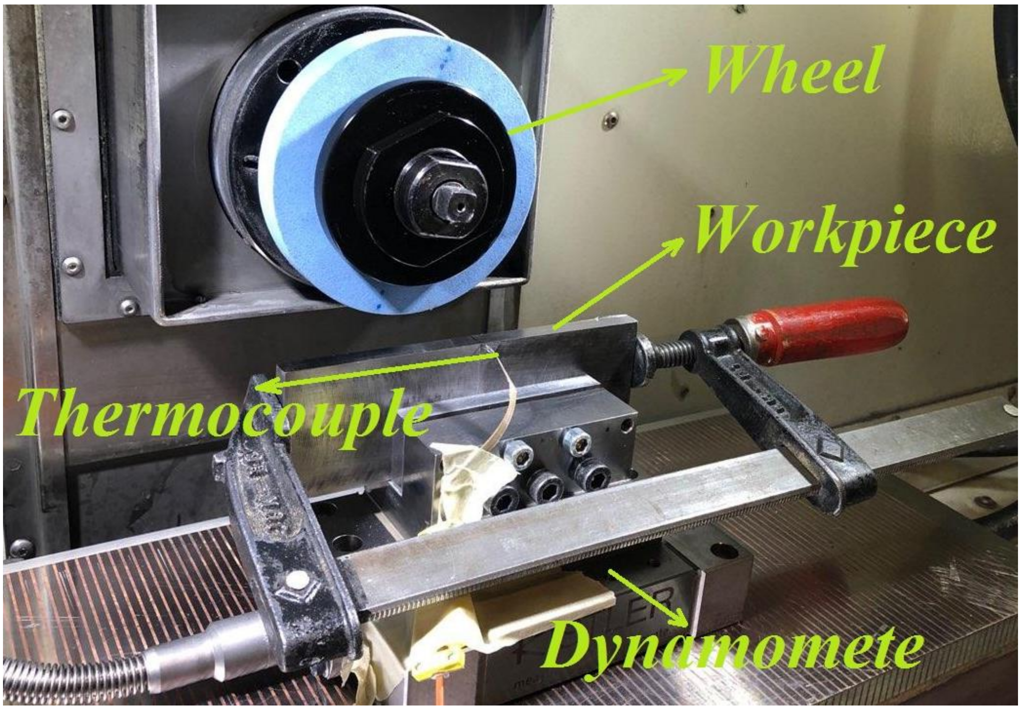

Figure 6-13 setup of the experiment for burn tests

The results of experiments are presented and discussed in Chapter 6.

7 RESULTS AND DISCUSSIONS

In this chapter the results of the experiments are presented. The distribution of the grit properties at different wheel conditions is presented. Surface roughness, force and temperature data are discussed in detail, and the comparisons with the models are provided.

7.1 Distribution of Grit properties

Among properties, the grit height distribution is the most important factor affecting the workpiece surface roughness, the grinding force and consequently the grinding temperature. Generally, the stochastic nature of the grit height was modeled in the literature by assuming a normal distribution as it was discussed in Chapter 5. However, the data should be examined statistically to check whether the data follow a normal distribution or not. There are different procedures known as normality tests to check whether the data has a normal distribution [124]. Considering the sample size of the data [125], and the accuracy of the tests [126], Kolmogorov-Smirnov and Shapiro-Wilk [124]tests are used to check the normality of different wheels used in this thesis. The results of the tests revealed that a normal distribution can be a good fit for the grit height of a fresh wheel while a worn or trued wheel does not show such a normal distribution. This can be explained by the fact that as the wheel starts to wear the grits with high heights lose their peaks through various wear mechanisms, i.e. pull out, attritious and fracture, where heights of non-active grits will remain unchanged. This phenomenon causes a distribution with negative skewness which can be fitted with a generalized extreme value distribution properly [127].

List of the wheels used in this thesis reported in Table 6-1 and presented again in Table 7-1 with related parameters required to be known for the force model in here.

The height distributions of 5 wheels listed in Table 7-1 are shown in Figure 7-1 to 7-5.

Table 7-1 list of wheels

Wheel number	1	2	3	4	5
Properties	CBN electroplated (fresh)	CBN electroplated (fresh)	CBN electroplated (fresh)	CBN electroplated (trued)	CBN electroplated (worn)
Diameter(mm)	10	5	30	10	10
Static number of grits	33	97	23	33	31
Grit width(μm)	65	41	73	67	39
Average girt edge radius (μm)	1.15	1	1.07	1	1.37
Mean and standard deviation of girts height(μm)	46 & 18	30 & 11	88 & 17	37 & 8	25 & 3.2
Mean and standard deviation of width of cuts(μm)	18 & 6	9 & 4	23 & 11	17 & 7	16 & 7
Average rake angle	-52	-50	-49	-52	-53
Average oblique angle	24	39	27	46	30
Mean and standard deviation clearance angle	4.1 &1.9	3.5 &2.1	4.5 &2.3	3 &1.9	1.5 &1.1

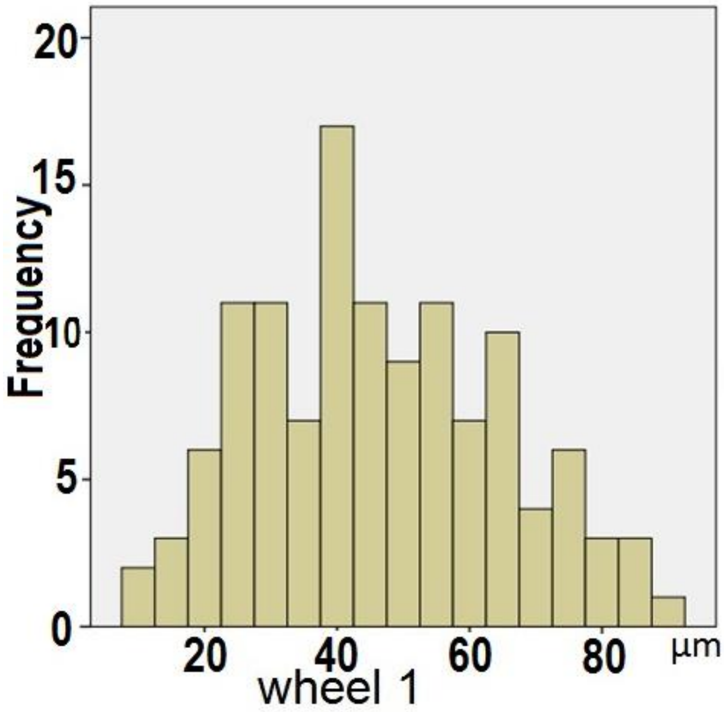

Figure 7-1 height distribution of the grit for wheel 1

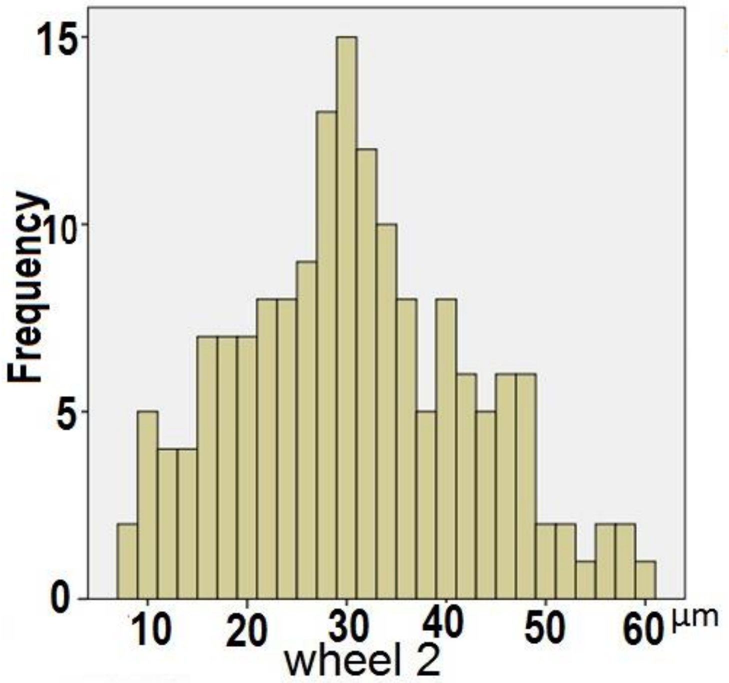

Figure 7-2 height distribution of the grit for wheel 2

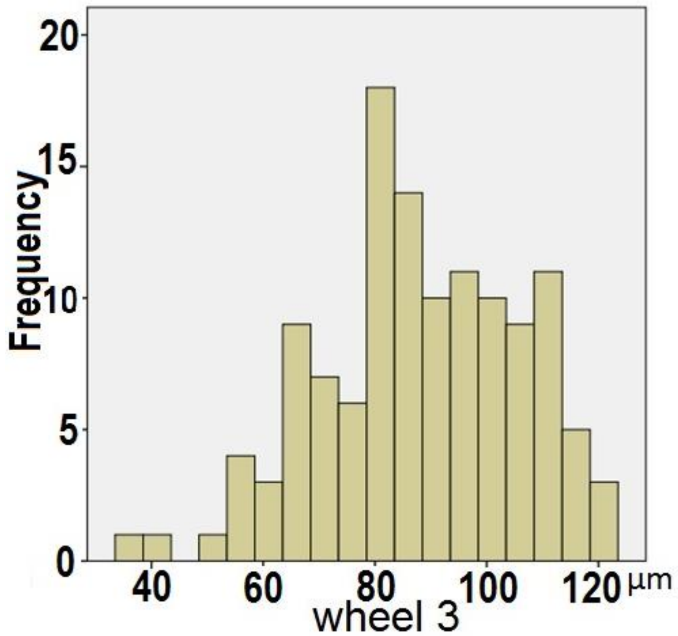

Figure 7-3 height distribution of the grit for wheel 3

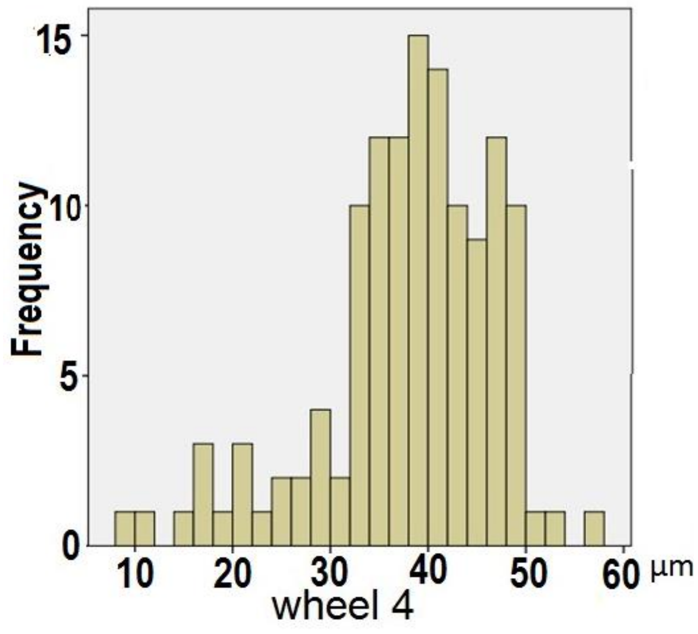

Figure 7-4 height distribution of the grit for wheel 4

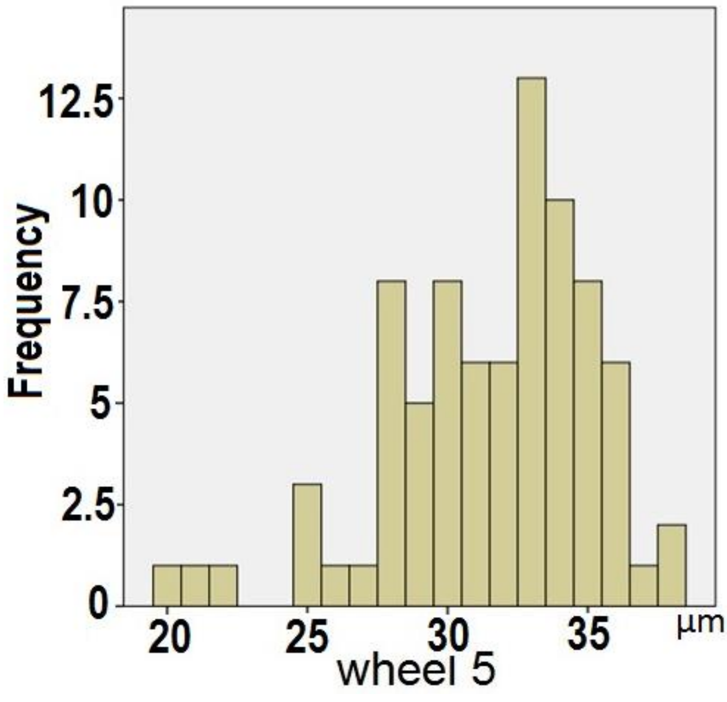

Figure 7-5 height distribution of the grit for wheel 5

As was mentioned, the data should be examined statistically (analysis of normality) to see whether it follows a normal distribution. Kolmogorov-Smirnov and Shapiro-Wilk tests were used in this thesis to check the distribution of grit heights on the measured wheels [124]. The tests of normality on the data were done by SPSS software (https://www.ibm.com/analytics/spss-statistics-software) for the wheels and the results have been reported in Table 6-2. The tests examine the null hypothesis. Null hypothesis in here assumes sample data are not significantly different than the normal data. They compare data with a normal population with the same mean and standard deviation of the sample data. The output of the tests is a number (p_0) which is the probability of finding results when the null hypothesis is true. p_0 is compared with a threshold usually taken as 0.05. If the value of p_0 for both tests is greater than 0.05, it is concluded that the data are normally distributed; if not it indicates a non-normal distribution [125].

Table 7-2 Results of Tests of Normality

	Kolmogorov-Smirnov		Shapiro-Wilk	
	Sample size	p_0	Sample size	p_0
Wheel 1	122	0.200	122	0.093
Wheel 2	165	0.200	165	0.069
Wheel 3	123	0.200	123	0.071
Wheel 4	128	0.000	128	0.000
Wheel 5	81	0.000	81	0.001

As it can be seen from Table 7-2, the first three fresh wheels have a $p_0$value of higher than 0.05 for both Kolmogorov-Smirnov and Shapiro-Wilk tests indicating a normal distribution of grits height, while for the trued and worn wheel the values are less than 0.05 implying a normal distribution did not exist. Based on the experimental results a generalized extreme value distribution was fitted for the trued and the worn wheels. Figure 7-6 and 7-7 show probability density functions of wheel 4 and 5 respectively along with fitted curve by the generalized extreme value functions. Distribution parameters of each function are reported in Figures 7-6 and 7-7, as well.

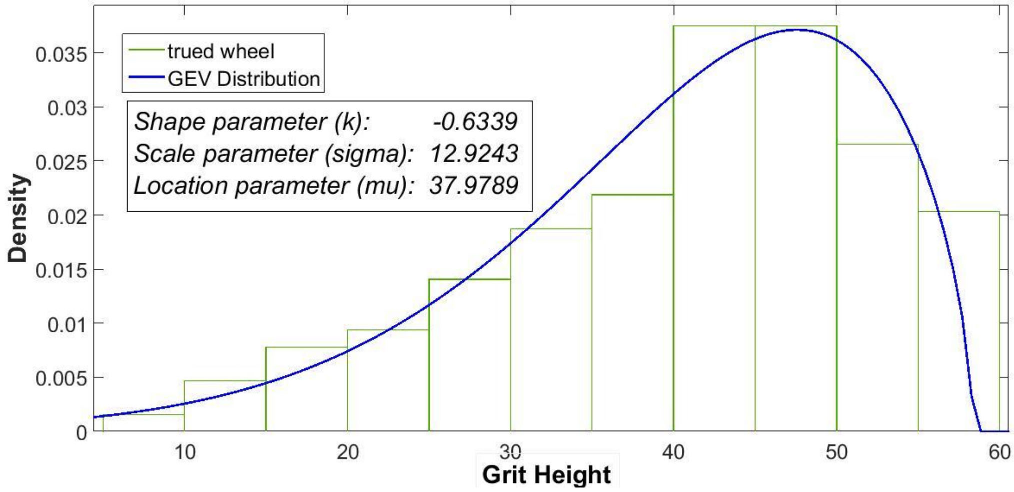

Figure 7-6 Probability density function of grit height for the trued wheel (wheel 4)

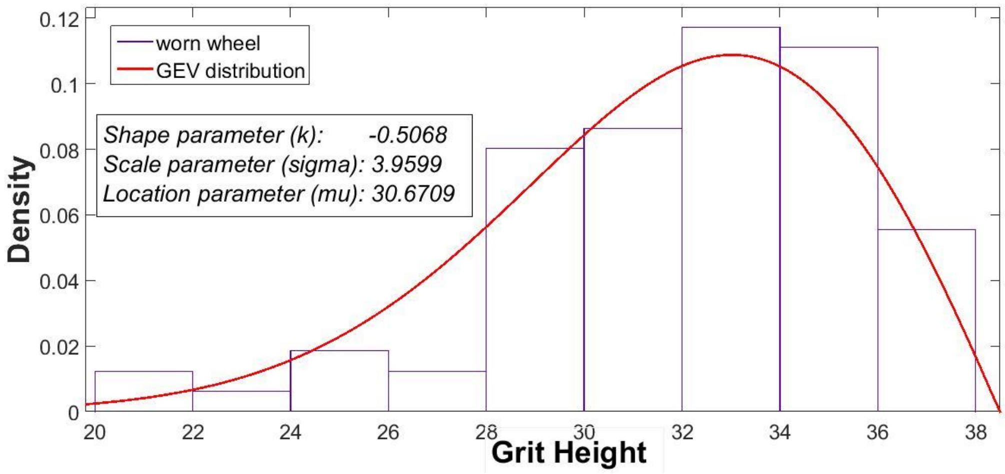

Figure 7-7 Probability density function of grit height for the worn wheel (wheel 5)

These results imply that using a normal distribution for grits height is not appropriate when a trueing operation has been done for this kind of wheels or when the wheel is worn. According to the results obtained from these analyses normal and generalized extreme value distribution are used for grit height distribution of the fresh wheels and non-fresh wheels, respectively. The parameters of such distributions should be obtained by measuring the grinding wheel.

7.2 Validation of Kinematic-Geometrical Model

Workpiece surface roughness perpendicular and parallel to the cutting direction was measured and compared with the surface roughness obtained by model. Active Number of grits can be validated indirectly by comparing the surface roughness in the cutting direction.

Figure 7-8 show the surface roughness of the workpiece in terms of R_a created by the wheels for different cutting conditions perpendicular to the cutting direction. The standard deviation of the grits height of the wheels varies from 18 µm to 3.2µm. The wheels with higher standard deviation (wheel 1 and 3) created a rougher surface and the best finished surface was created by the worn wheel which had the lowest standard height distribution (see table 6-1). The average discrepancy between the predicted values and the experimental results is 6.6%. Among all of the grinding conditions and the wheel parameters, the grit height standard deviation is the predominant factor affecting the roughness value perpendicular to the cutting direction. It is due to this fact that the radial depth is different in each element and directly depends on the standard deviation of grit height. Furthermore, the feed marks are in nano scale where wheel eccentricity and vibration effects on the surface roughness cannot be seen perpendicular to the cutting direction since their effects are same on all elements. This result indicates that any kinematic model which has been validated only by comparing the surface roughness in this direction is incomplete. Accordingly, in this thesis surface roughness has been compared in the cutting direction as well.

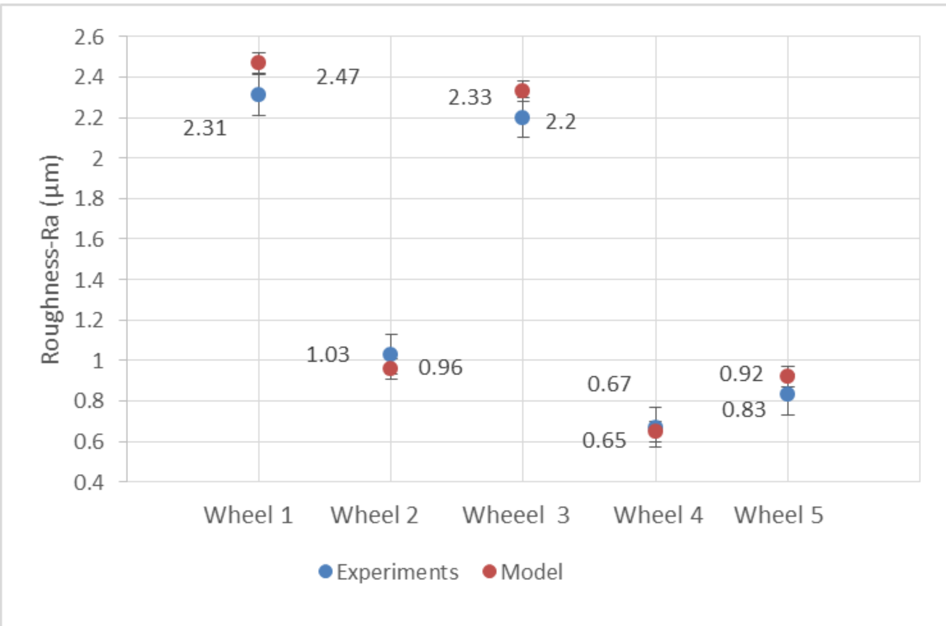

Figure 7-8 Surface roughness value (R_a) perpendicular to the cutting direction for wheel 1 to 5 at different feed rates(0.01 to 0.1 mm/rev) and depth of cuts (0.02 to 0.1 mm)

Figure 7-9 and 7-10 illustrate the surface roughness of the workpiece parallel to the cutting direction for wheels 1 and 4 at different feed rates.

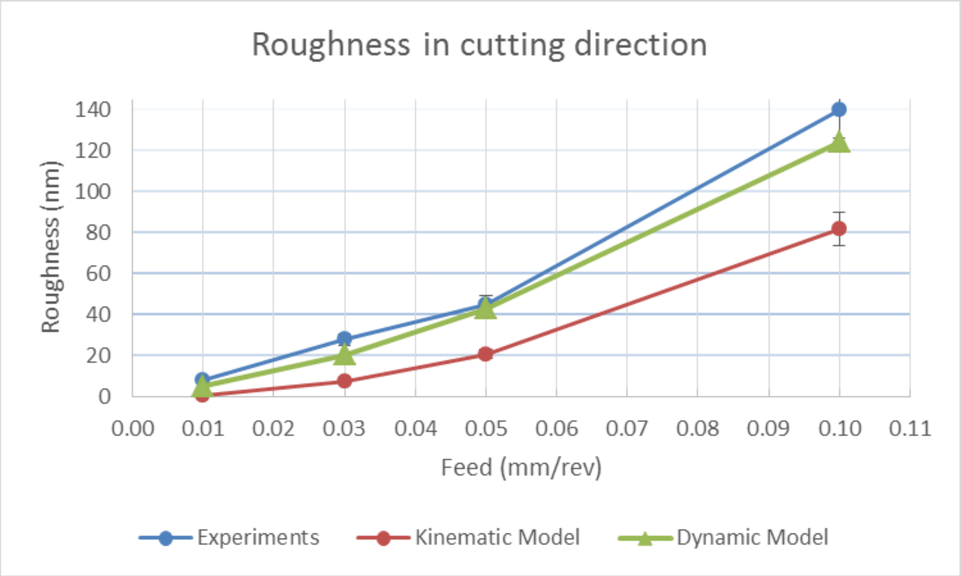

Figure 7-9 Surface roughness values parallel to the cutting direction for wheel 1 at different feed rates, 10 micron wheel run out, 40 micron depth of cut

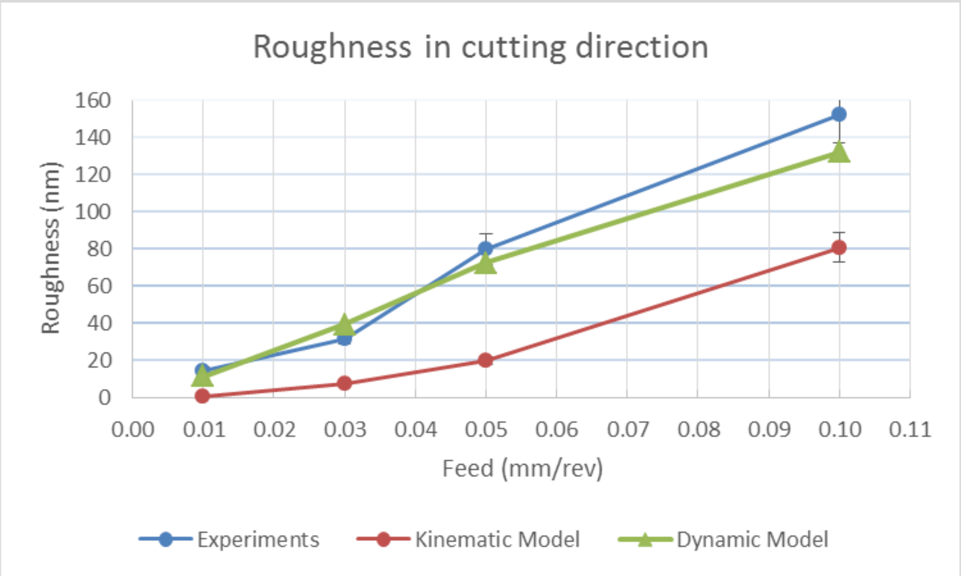

Figure 7-10 Surface roughness values parallel to the cutting direction for wheel 4 at different feed rates, 10 micron wheel run out, 40 micron depth of cut

As it can be seen from Figures 7-9 and 7-10, increasing feed rate resulted in higher surface roughness. The kinematic model values were obtained by neglecting the dynamic displacements of the wheel. As it can be seen from figures 7-9 and 7-10, including the vibration effect has improved the accuracy of the model prediction. The discrepancy between the dynamic model and the experiments was obtained as 19% and 16.5% for wheel 1 and 4, respectively. Including vibration effects, improved model accuracy by approximately 40% and 53% for wheels 1 and 4, respectively.

The effect of the depth of cut on the surface roughness is shown in Figure 7-11 to further examine the accuracy and validity of the model. Similar to the previous figures, in the kinematic model the effect of vibration was neglected, while it is included in the dynamic model. Based on this figure, neglecting the vibrations can greatly affect the prediction accuracy of the surface roughness. Due to the kinematic model, increasing depth of cut resulted in a small improvement on the surface roughness. This could be explained by the fact that, increasing depth of cut, while keeping other grinding conditions constant, caused an increase in the active number of grits. Increasing active number of grits while the feed per revolution is fixed resulted in decreasing feed per each active grit which resulted in decreased surface roughness. However, experimental results in the figure show an opposite trend i.e. increasing the surface roughness with increasing depth of cut. This trend can be explained and predicted by considering the dynamic aspect of the process. Increased depth of cut results in increased force which caused more wheel vibration which in turn increased the surface roughness. The dynamic model proposed in this paper predicted the surface roughness with good accuracy compared with the experimental results. Furthermore, consideration of vibration effects improved the model prediction accuracy approximately by 51% for this wheel.

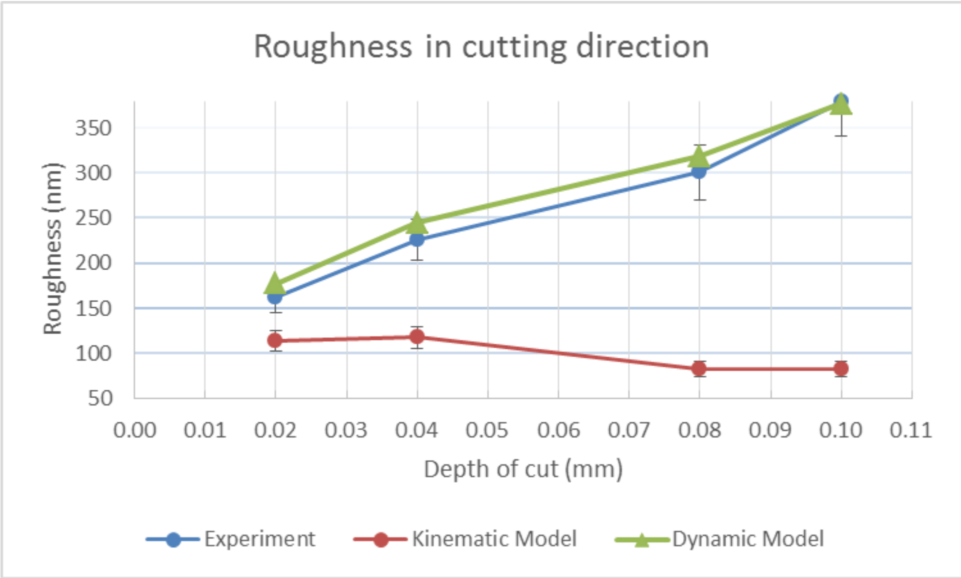

Figure 7-11 Surface roughness values parallel to the cutting direction for wheel 5 at different depth of cut, 10 micron wheel run out, 0.1 mm/rev feed rate

Another validity test was conducted by including the effects of wheel eccentricity on the kinematic-geometrical model. Different amounts of eccentricity were added to wheel number 2 by deflecting its arbor to examine the effect of run out on the surface roughness (Figure 7-12). The wheel run-out was measured by a high precision dial indicator with the accuracy of 1 µm. The surface roughness was measured for 2µm, 13µm, 35µm and 70µm wheel run outs. As expected, increasing run-out resulted in increased surface roughness in the cutting direction. However, for run out of higher than 35µm, the surface roughness was approximately fixed, both in the model and experimental data. This is due to the fact that increasing run-out causes a decrease in the active number of grits and at a particular wheel run-out the active number of grits reaches its minimum value where further wheel eccentricity will not decrease the active number of grits. Based on the data in Figure 14, it can be concluded that a reasonable agreement can be achieved between the model and experimental results (19.5 percent discrepancy).

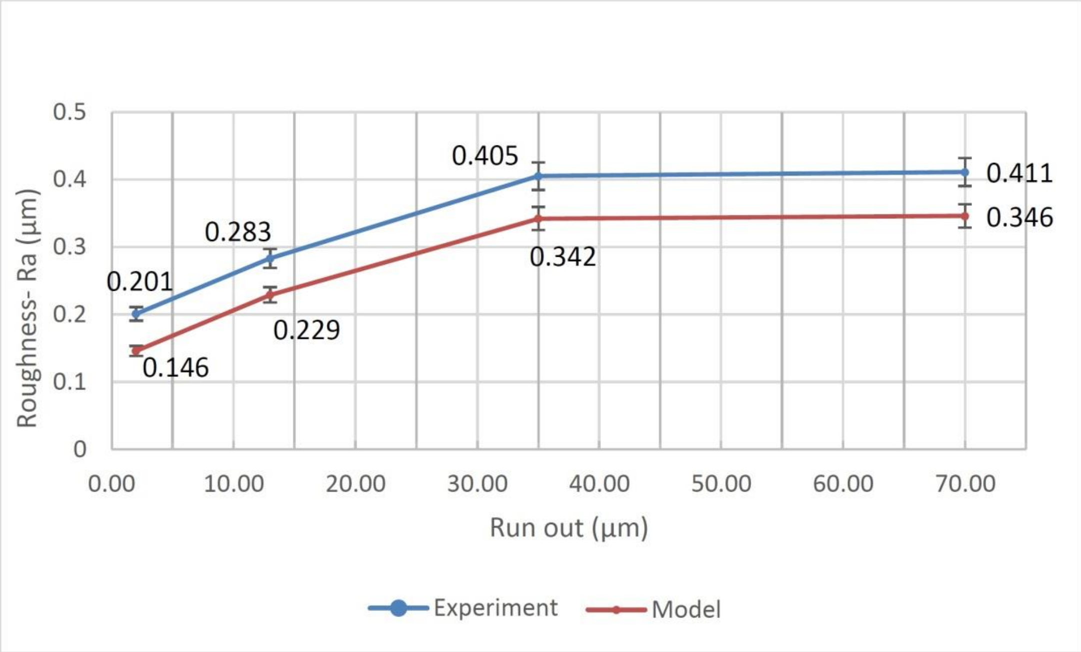

Figure 7-12 Surface roughness values parallel to the cutting direction for wheel 2 at different run out, feed rate 0.14mm/rev, depth of cut 0.08 mm

7.3 Effect of the Active Number of Grits on Chip thickness

According to the proposed model in this study, due to the height distribution of the wheels, active grits create different chip thicknesses. As a result, instead of having a unique maximum chip thickness, there is a frequency of maximum chip thickness. Increasing the active number of grits while keeping the grinding conditions fixed causes decrease in the maximum chip thickness. At the same time, grinding force is a function of both the active number of grits and the chip thickness, therefore implying an inverse relationship. As a result, the final effect of the active number of grits on the grinding force must be evaluated by using the kinematic-geometrical model. Figure 7-13 shows the probability density function of the maximum chip thickness for three different wheels (wheel 1, 4 and 5). The grinding conditions were the same for all wheels. The average values of maximum chip thickness and the active number of grits (in percentage) are also reported in Figure 6-13 to make a clear comparison between the wheels. As it can be seen from this figure, the worn wheel had the highest percentage of active numbers of grits (29.5%), in contrast to the trued or fresh wheel having 19.5% and 11.5%, respectively. Furthermore, a wheel with more active numbers of grits had a smaller average of maximum chip thickness.

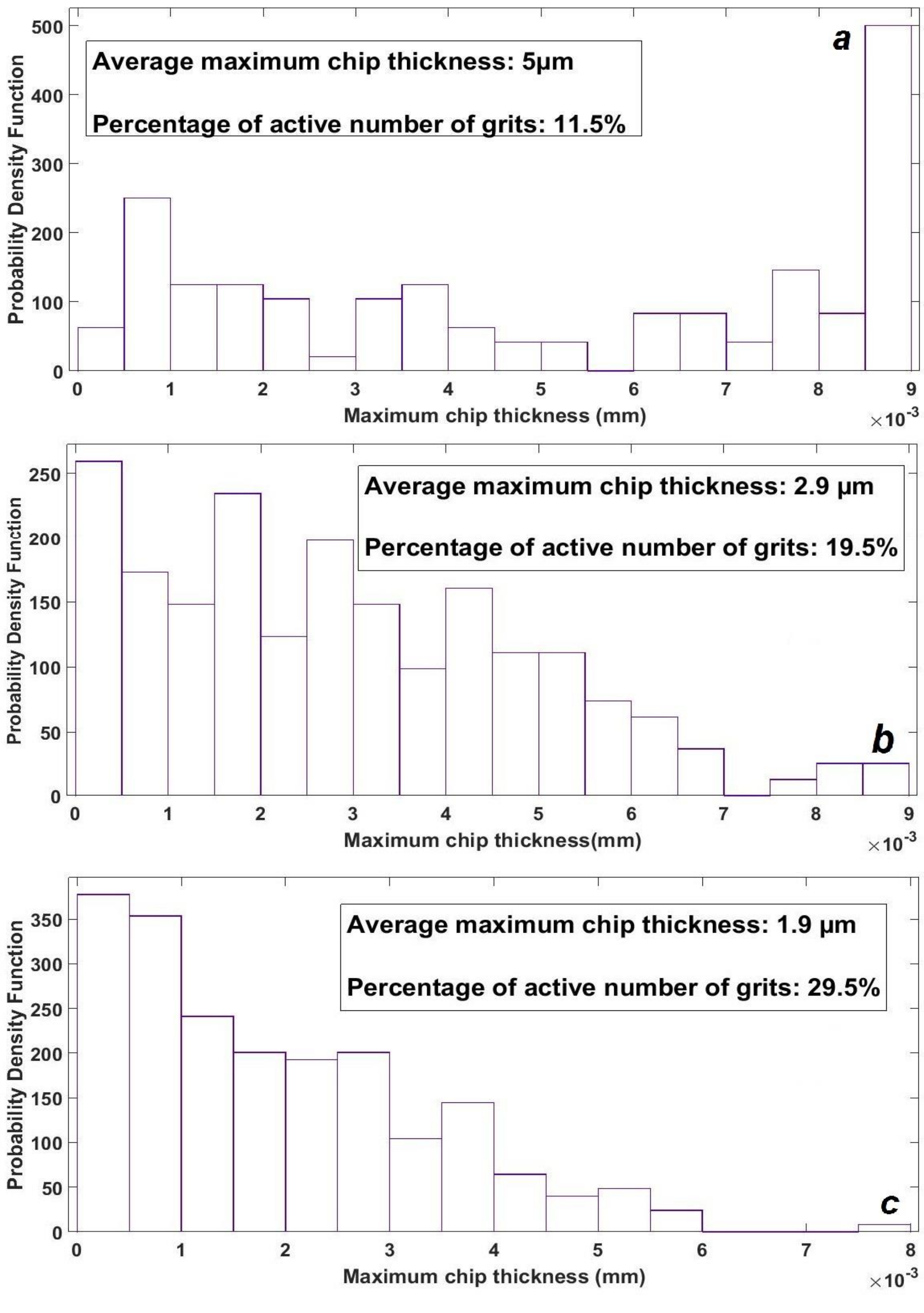

Figure 7-13 Probability density function of maximum chip thickness, depth of cut 0.08mm, feed rate 0.05 mm/rev for wheel 1 (a), wheel 4 (b) and wheel 5 (c)

7.4 Verification of the Force Model

Figure 7-14 shows a sample of force model prediction along with experiment data for wheel 2. The kinematic-geometrical force model considering micro interaction of grit-workpiece provides not only the average grinding force but also the profile of the force pulse. The profile of the force according to the proposed model is the summation of the force created by the interaction of each active grit with the workpiece in all radial elements. As can be seen, the model predicted the force pulse with good accuracy (normal and feed force in the positive and negative direction respectively). Furthermore, the average value of the force and the contribution of each force portion namely, ploughing, cutting and DMZ, have been calculated by the MATLAB code and shown in Figure 7-14. Each force portion can be calculated according to the proposed model by comparing the instantaneous chip thickness with the critical chip thickness. When the chip thickness is less than the critical chip thickness, the ploughing portion of the force is determined by using equation 3-20. However, if the chip thickness exceeds the critical chip thickness, the cutting portion, and the force due to the formation of the dead metal zone are calculated from equations 3-22 and 3-5, 3-6 respectively.

Direction	F_total	F_plough	F_dmz	F_cutting
Cutting (x)	-3.285	-0.161	-0.833	-2.291
Normal (z)	13.561	1.084	7.539	4.938

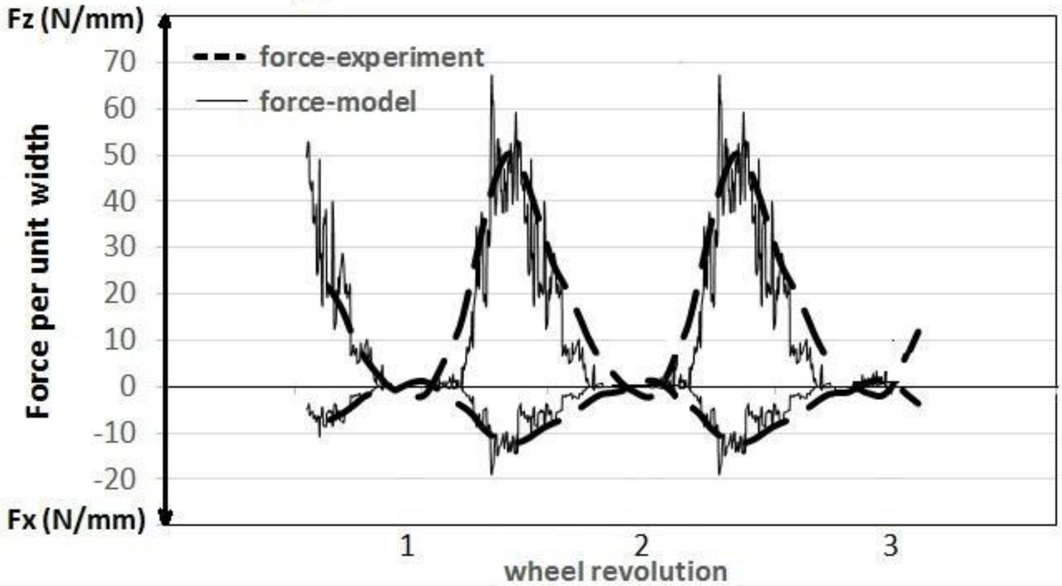

Figure 7-14 Grinding force per unit width in the cutting and normal direction for wheel 1, depth of cut 80 μm, feed 0.1 mm/rev, run out 10 μm

Figure 7-15 shows the grinding force per unit length for wheel 1 at different feed rates and 80 µm depth of cut. As it can be seen from this figure, the model can predict the force with good accuracy. The average discrepancies between the model and experiments in cutting and normal directions are 11% and 12%, respectively. As it can be seen, increasing the feed resulted in increased force in both directions; however, the rate of force growth has slowed down. The force per unit length has increased 4.1 times (2.6 to 10.7 N/mm) in the normal direction and 5.1 times in the cutting direction (0.72 N/mm to 3.7) while increasing the feed rate 10 times (0.01 mm/rev to 0.1 mm/rev), respectively. In other words, the specific energy of grinding is decreased by increasing the feed rate. The reason for this behavior can be explained by taking the contribution of each force portion into account. Generally, it is possible that at low feed rates the maximum chip thickness corresponding to each active grit is smaller than the critical chip thickness. Accordingly, many of those active grits only create pure ploughing force and do not result in material removal action increasing the specific energy. By increasing the feed rate, the maximum chip thickness increases and many of those grits participate in the material removal process which causes a decrease in the specific energy.

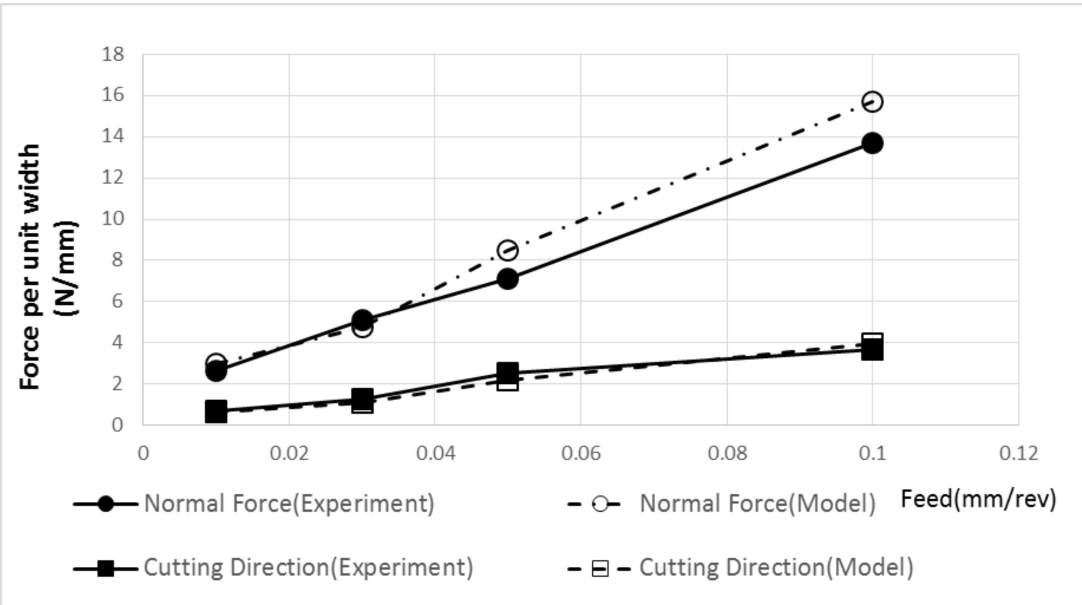

Figure 7-15 Grinding force per unit width in the cutting and normal direction for wheel 1, depth of cut 80 µm, run out 10 µm

To clarify further, the contributions of each force portion are shown in Figure 7-16. As can clearly be seen from the percentages, the ploughing force amounts to the largest portion of the total force at very low feed rates (49% and 53% in the cutting and normal directions, respectively, when feed is 0.01 mm/rev) while the contribution of cutting and DMZ increases with the feed. The high percentage of the ploughing force at low feed rates is the main reason for the high specific energy required in grinding at low feed rate based on what has been discussed. By increasing the feed rate, maximum chip thickness also increases, and thus the respective contributions of cutting and DMZ portions also increase.

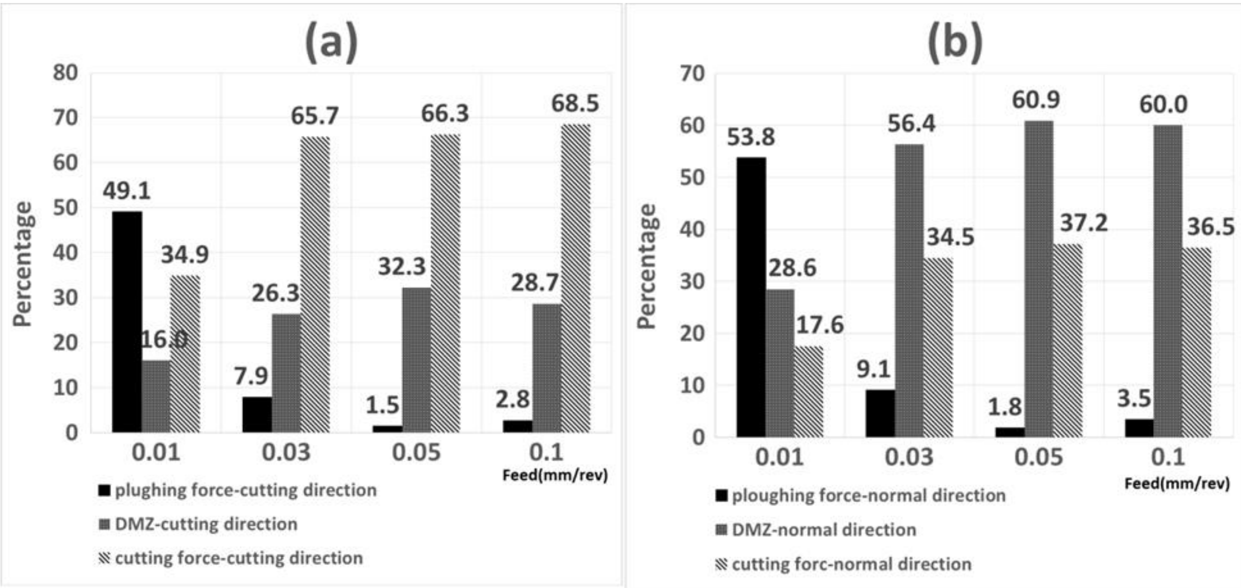

Figure 7-16 Contribution of force parts in the cutting direction (a) and normal direction (b) for wheel 1 at different feed rate, depth of cut 0.08 µm, run out 10 µm

The effect of depth of cut on the total force is shown in Figures 7-17 and 7-18 for wheels 1 and 2, respectively, when the feed rate was fixed at a low value of 0.01 mm/rev. The experimental results were obtained by setting the feed rate fixed and changing the depth of cut from 20 µm to 100 µm. The grinding conditions and the wheel properties were set in the MATLAB code, and the results have been compared in terms of the average grinding force. The average discrepancies in the cutting and normal direction are 11% and 10% for wheel 1, and 12% and 11% for wheel 2, respectively. The contribution of each force component to the total force is also calculated by the model and the results are shown in Figure 6-19 for wheel 1. The results clearly explain the reasons for the high specific energy required in grinding operations at very low material removal conditions. As can be seen, the ploughing force accounts for a greater portion of the total value at small depth of cuts similar to the previous case of low feed rate. This is again due to the fact that at very low depth of cut, the maximum chip thickness is less than the critical value for most of the active grits resulting in increased total force. In this case, the active grits that encounter maximum chip thickness that is less than critical, only create the ploughing force, and do not participate in the material removal process. It is worth mentioning that the ploughing and DMZ mechanisms do not contribute to the material removal process, however, they contribute to the total force due to the inherent characteristics of the grinding process, (namely micro-scale material removal process) by grits having low clearance angles, negative rake angle and a hone radii in scale of chip thickness. By increasing the depth of cut or feed rates (Figure 7-16 and 7-19) the ploughing portion of the grinding force is decreased in proportion, where both DMZ and the cutting portion of the total force increase. Accordingly, at low depth of cut and feed rate, the ploughing portion, and at high depth of cut and feed rate, the DMZ portion, of the force results in higher grinding force. This phenomenon partially explains the reason for higher specific energy in grinding compared to other material removal processes.

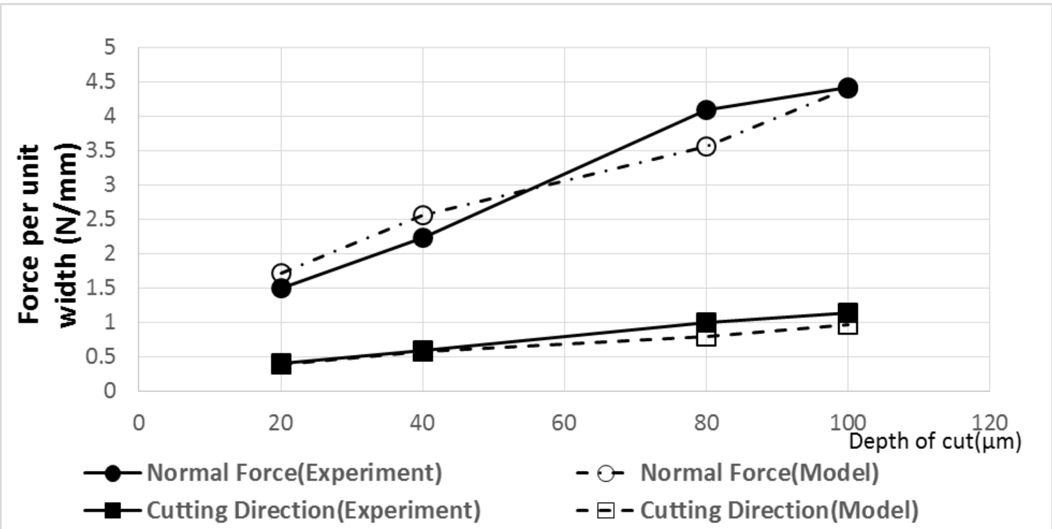

Figure 7-17 Grinding force per unit width in the cutting and normal direction for wheel 1 at different depth of cuts, feed 0.01 mm/rev, run out 10 µm

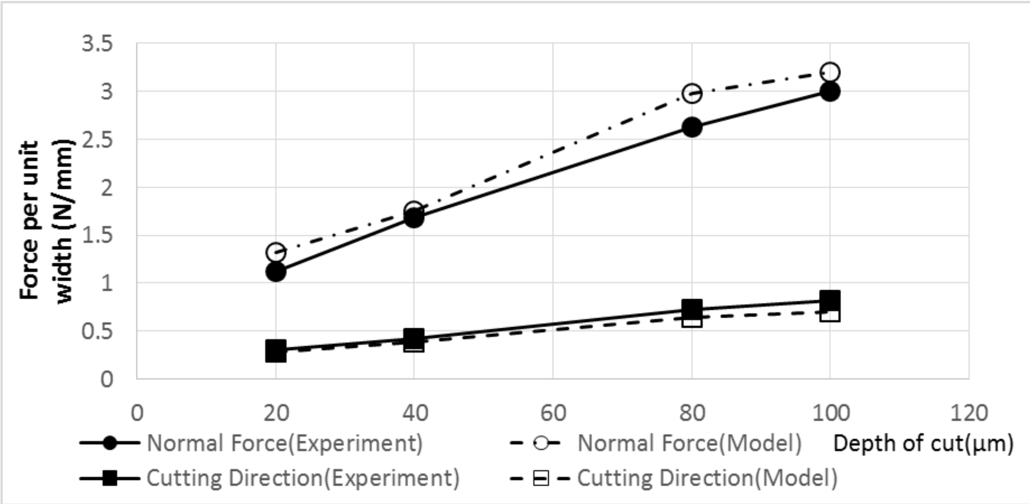

Figure 7-18 Grinding force per unit width in the cutting and normal direction for wheel 2 at different depth of cuts, feed 0.01 mm/rev, run out 10 µm

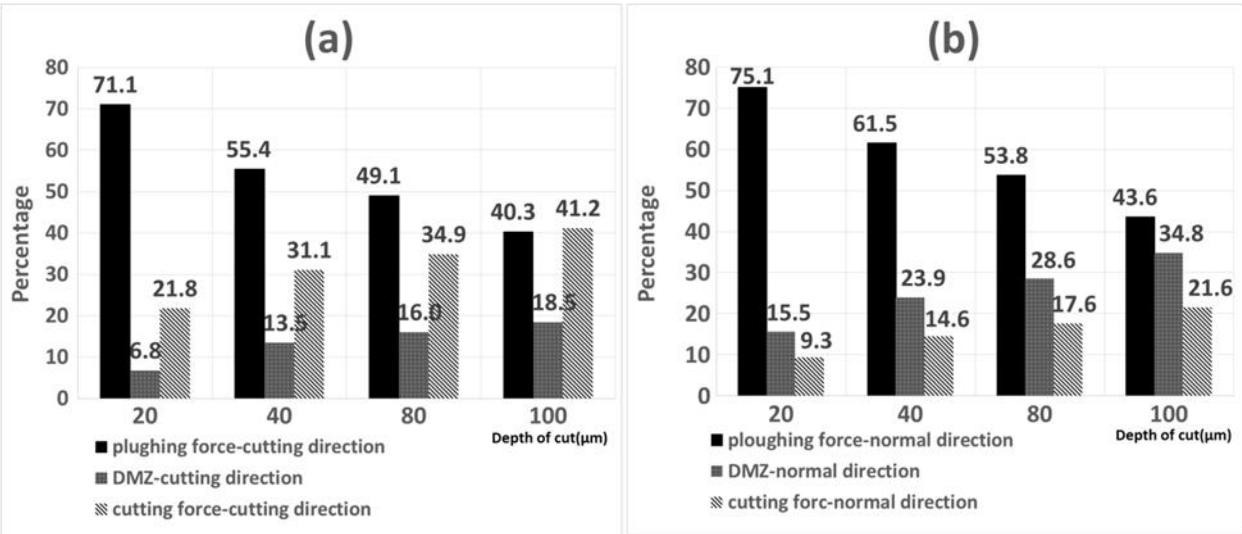

Figure 7-19 Contribution of force parts in the cutting direction (a) and normal direction (b) for wheel 1 at different depth of cuts, feed 0.01 mm/rev, run out 10 µm

In order to further examine the validity of the force model additional experiments were carried out with wheels 3, 4 and 5. Figure 7-20 shows the forces for wheel 3 at different depths of cut to investigate the effects of depth of cut while the feed rate was fixed at the high value of 0.1 mm/rev in order to examine the validity of the model in a wide range of grinding conditions. The discrepancies in the cutting and normal directions are 14% and 13%, respectively.

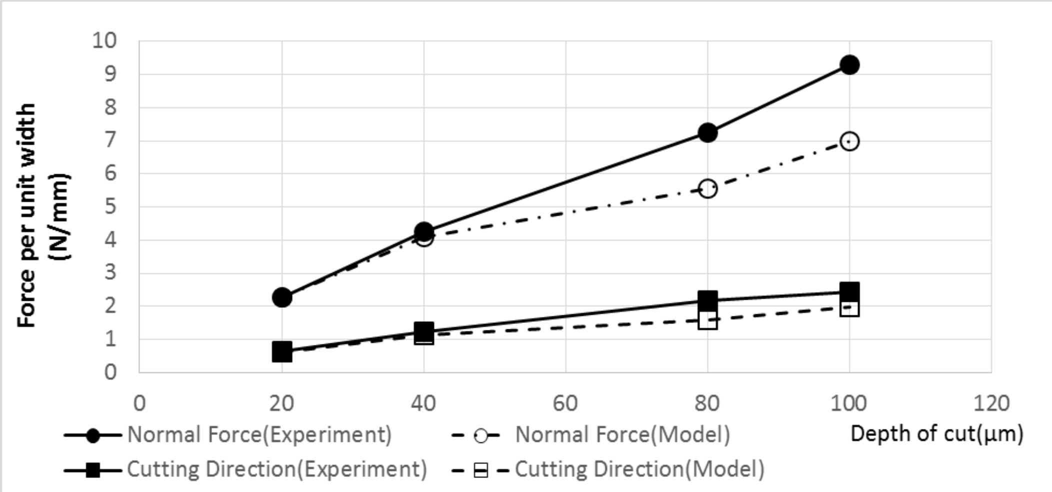

Figure 7-20 Grinding force per unit width in the cutting and normal direction for wheel 3 at different depth of cuts, feed 0.1 mm/rev, run out 10 μm

In Figure 7-21, the grinding force predictions and measurements are shown for wheel 1 (fresh), 4 (trued) and 5 (worn). The aim of these experiments were to investigate the effect of different grit properties on the grinding force under constant grinding conditions. Two copies of wheel 1 were used to test the trued and the worn wheels. Table 7-1 shows the specific characteristics of these wheels. The most important differences between these wheels are their grit height distributions and clearance angles. According to Table 7-1, the fresh wheel has the highest average and grit height standard deviations whereas the trued wheel comes in second, and while the worn wheel has the smallest average and standard deviation of the grit height. Furthermore, the worn wheel has the smallest average value for the grit clearance angle and the trued and the fresh wheels follow behind. As it can be seen the fresh wheel has the minimum force compared to the trued wheel and the worn wheel which has the highest force value. This is due to the grit characteristics of these wheels. Distribution of grit height plays a vital role in the active number of grits, and thus on the total grinding force. As it was mentioned earlier, the standard deviation of the data for the grit height has the highest value for the fresh wheel which implies a low active number of grits, and thus a lower force. The worn wheel has the lowest grit height standard deviation which increases the active number of grits and thus the grinding force. Moreover, the lower clearance angle of grits in the worn and the trued wheel compared to the fresh one increases the ploughing portion of the force causing an increase in the total force. This fact can be confirmed by looking at the contribution of each force portion for these wheels (Figure 7-22). As it can be observed from this figure, the ploughing force accounts for more than 50% of the total force for the worn wheel and 29% for the trued wheel while this portion is below 3.5% for the fresh wheel in both cutting and normal directions. The current model could predict the grinding force for these wheels with average discrepancies of 8% and 9% in cutting and normal directions, respectively.

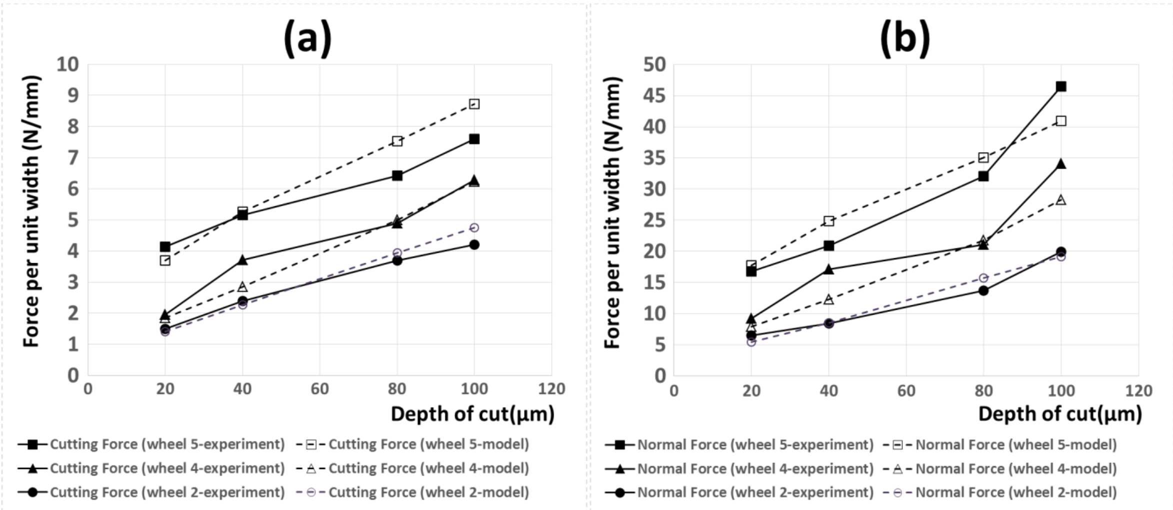

Figure 7-21 Grinding force per unit width in the cutting direction (a) and normal direction (b) for wheel 2 (fresh), 4 (trued) and 5 (worn) at different depth of cuts, feed 0.1 mm/rev, run out 10 µm

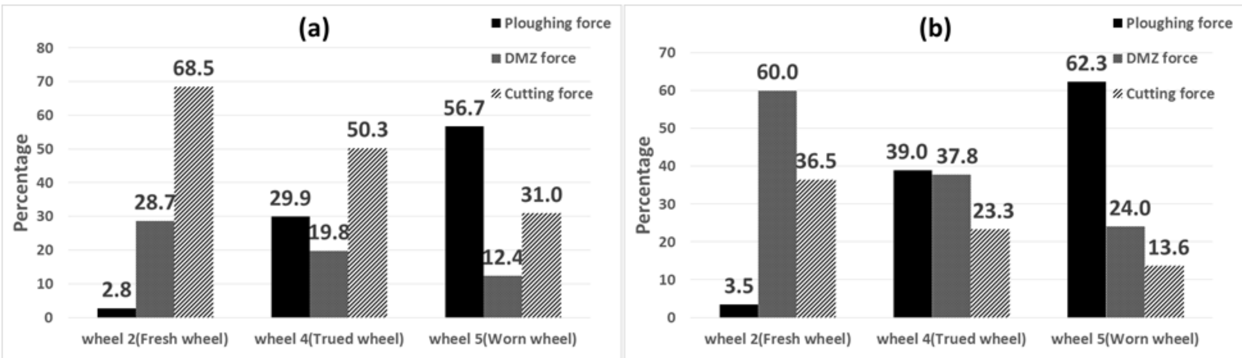

Figure 7-22 Contribution of force parts in the cutting direction (a) and normal direction (b) for the fresh, trued and worn wheels, depth of cut 0.08 µm, feed 0.1 mm/rev run out 10 µm

7.5 Verification of the Temperature Model

In order to validate the thermal model grinding tests were carried out using CBN electroplated and aluminum oxide wheels in dry and wet conditions in a wide range of grinding conditions. The effect of grinding conditions including depth of cut, feed rate and cutting speed on the maximum workpiece temperature has been explained using the current model in this section.

Figure 7-23 shows a sample temperature signal obtained from the thermocouples along with the predicted profile using the proposed model for dry condition and using the CBN wheel. As it can be seen the model is able to predict the temperature profile and the maximum temperature precisely. Furthermore, the temperature fluctuation is strong near the thermocouple position both in the model and experiment signal as it was expected and discussed in the thermal model. A small discrepancy between the experiment and the model results in the temperature profile may be attributed to the constant thermal and physical properties used for workpiece material and the wheel while in reality they are temperature-dependent variables.

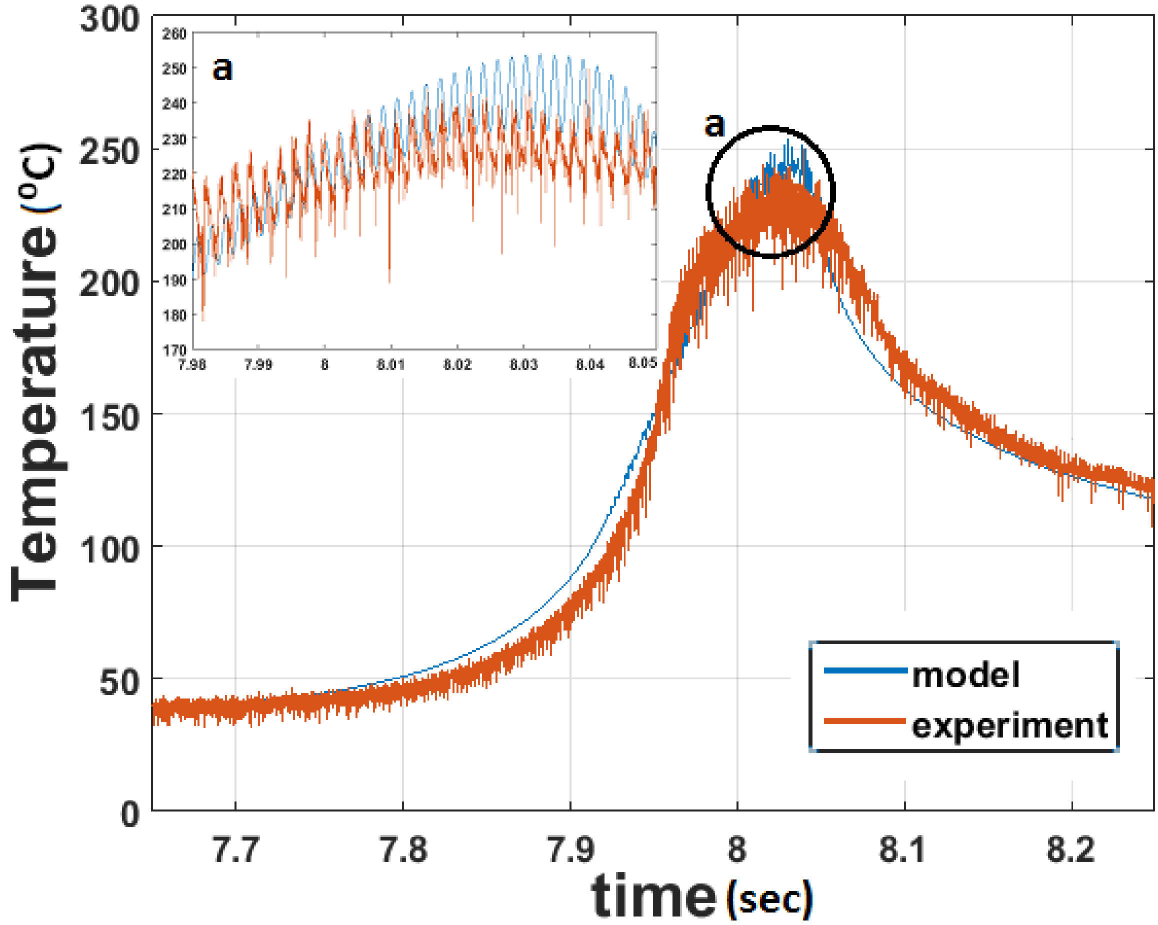

Figure 7-23 Temperature signal collected using CBN wheel, under dry condition with depth of cut of 100 µm, feed rate of 600mm/min and cutting speed of 29 m/sec

Figure 7-24 shows the effect of depth of cut on the maximum temperature using the CBN wheel in dry and wet conditions.

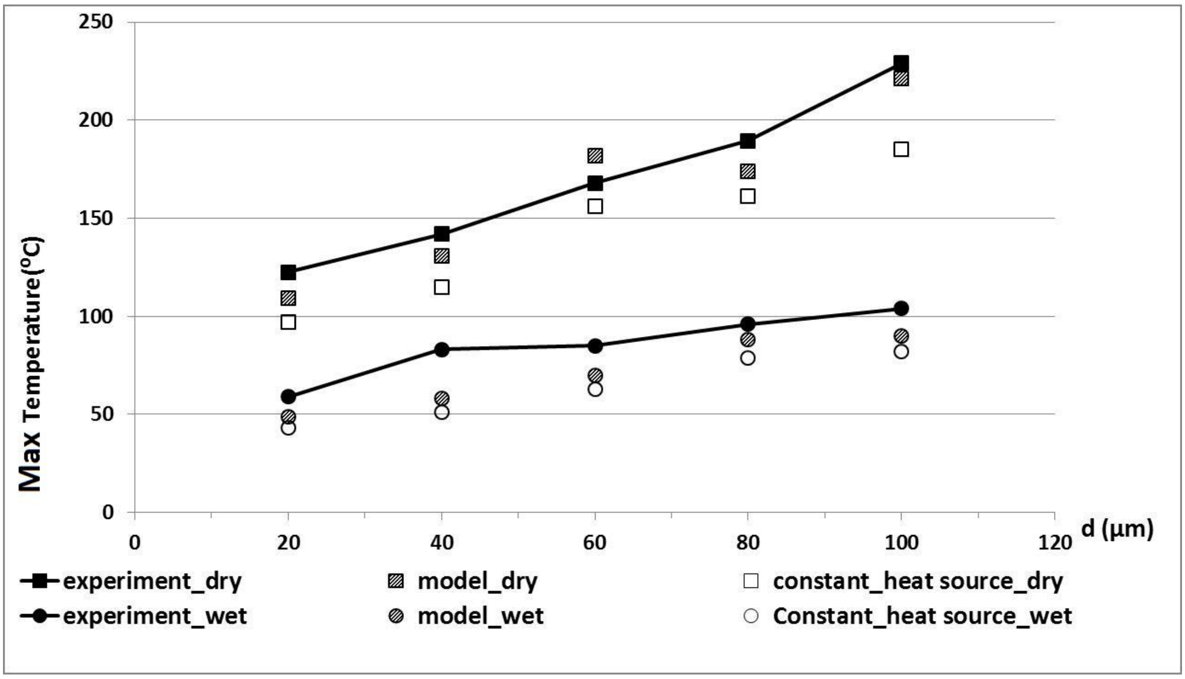

Figure 7-24 Maximum temperature in dry condition using CBN wheel at different depth of cuts, feed rate 600mm/min, cutting speed 29 m/sec

According to the figure, increasing the depth of cut resulted in higher maximum temperature as expected. The discrepancy between the experimental data and the model predictions are 7% and 17% for dry and wet conditions, respectively. The effect of including the periodic heat source in the model can be seen by comparing the temperature results obtained from considering a constant heat source in the model. According to the figure, maximum workpiece temperature using a constant heat source is lower than the model prediction considering the periodic heat source. The average discrepancy between the experimental and the model results in this case was 16% and 30% in dry and wet conditions, respectively. This data shows considering the periodic heat source can improve model prediction by approximately 11%.

Figure 7-25 shows the effect of the feed on maximum temperature in dry and wet conditions, respectively, using the CBN wheel again.

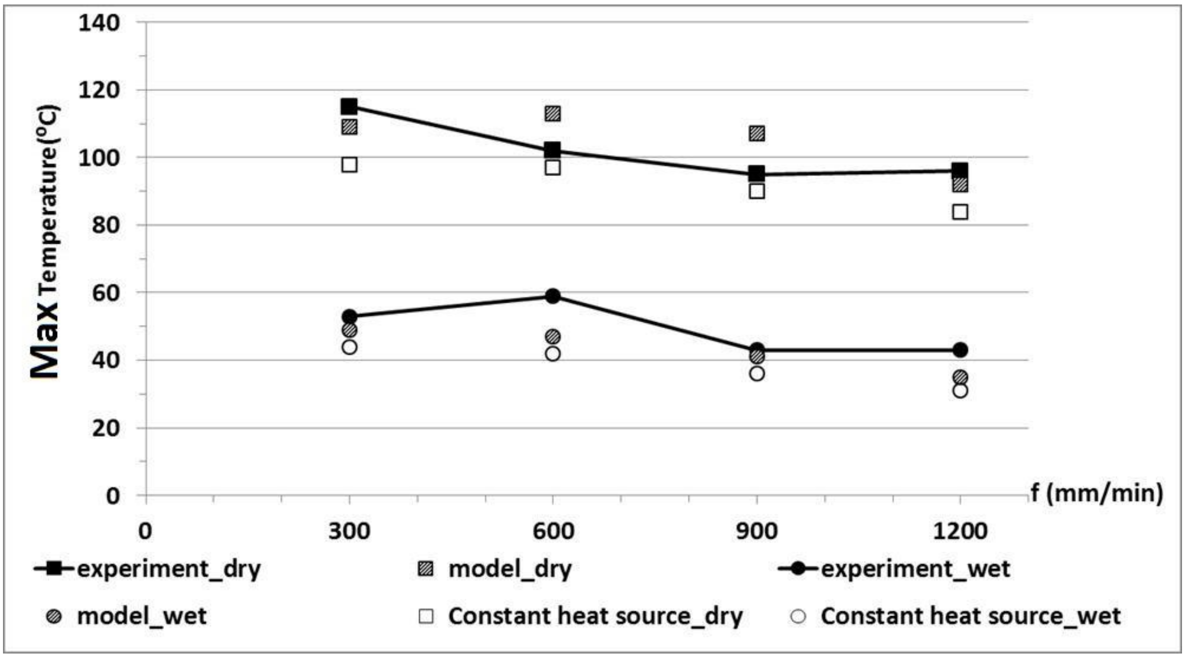

Figure 7-25 Maximum temperature in dry and wet conditions at different feed rates, depth of cut 20 µm, cutting speed 29 m/sec

The effect of feed rate on the maximum temperature can be explained by considering two contrary mechanisms. Increasing the feed rate results in moderate increase in the cutting force and consequently the strength of the heat source because the heat source strength is some portion of total power and the total power is proportional to the force in feed direction according to Equation 4-20. However, at the same time higher velocity of the heat source travelling on the surface decreases the time of heat flow going into the workpiece. These two mechanisms counterbalance each other, and the final effect depends on the strength of each mechanism. There is a very moderate increase [128], decrease trend [129] and constant behavior [130] reported in the literature. As shown in Figure 17, increasing the feed rate resulted in a very moderate decrease in the maximum temperature and the model could predict the behavior with a good accuracy (4.5% and 12.5% discrepancies with the measurements, respectively). Furthermore, considering the periodic heat source improved the temperature prediction as the discrepancy between experimental data and constant heat source model is 9% and 21% in dry and wet conditions, respectively, when considering the constant heat source in the model.

The experiments were also carried out using an aluminum oxide wheel. Figures 7-26 and 7-27 shows the maximum temperature measured at different depth of cut and feed rate, respectively. The temperature model could predict the maximum temperature with an average discrepancy of 11% and 8%, respectively. Based on Figures 7-26 and 7-27, considering a constant heat source in the model predicted the maximum workpiece temperature with an average error of 16% and 18% respectively

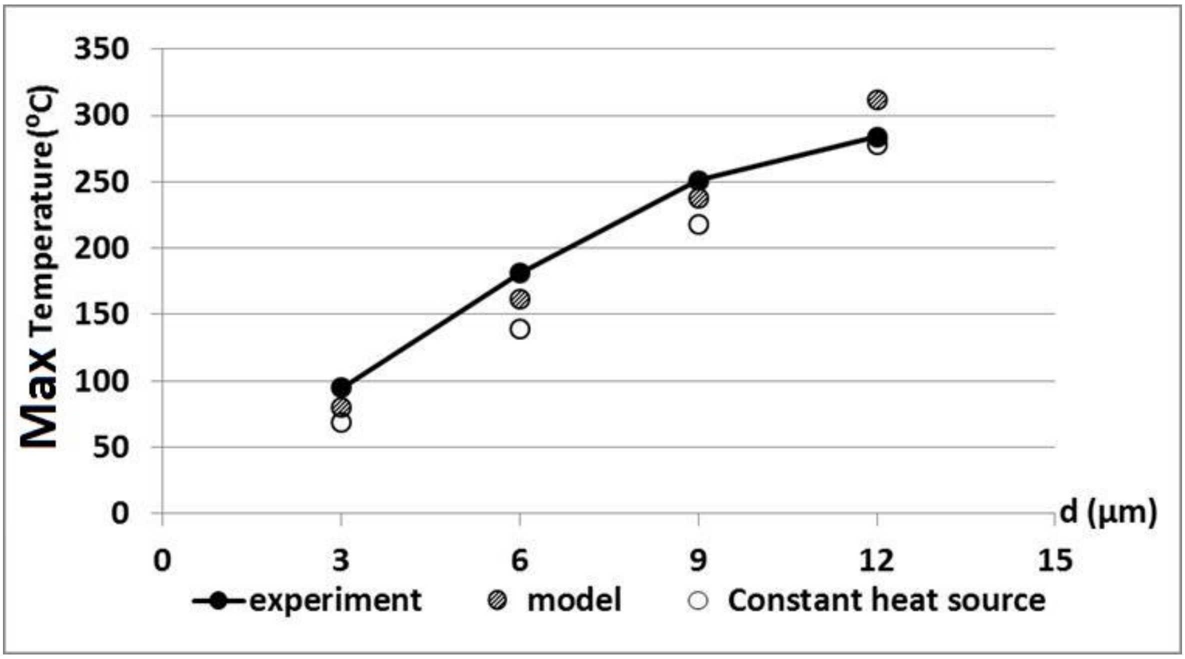

Figure 7-26 Maximum temperature in dry condition using aluminum oxide wheel at different depths of cut, and feed rate of 600mm/min and forcutting speed 10.4 m/sec

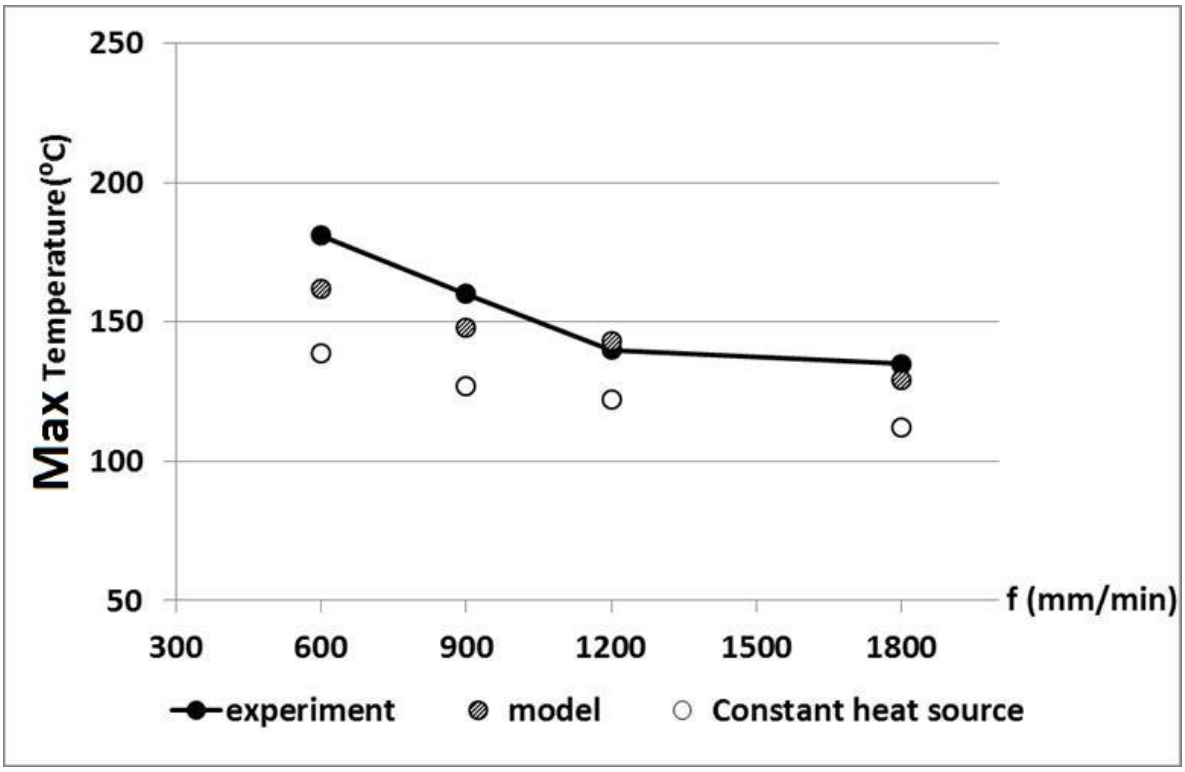

Figure 7-27 Maximum temperature in dry condition at different feed rates using aluminum oxide wheel where the depth of cut was 6 µm and the cutting speed was 10.4 m/sec.

The effect of cutting speed on maximum temperature was investigated by changing the grinding wheel rotational speed at a constant depth of cut and feed rate (Figure 6-28). As it can be seen, increasing the cutting speed resulted in a very moderate increase in maximum temperature of the workpiece. Increasing the cutting speed tends to increase the grinding power on one hand and on the other hand, the grinding force decreases with increased wheel speed as the average maximum chip thickness for all active grits decreases since the feed rate is kept constant. These two mechanisms counteracted each other and resulted in a moderate increase on the maximum temperature with grinding speed. Based on Figure 18, the model can predict the temperature with an average discrepancy of 8% while considering a constant heat source gives an average discrepancy of 15%.

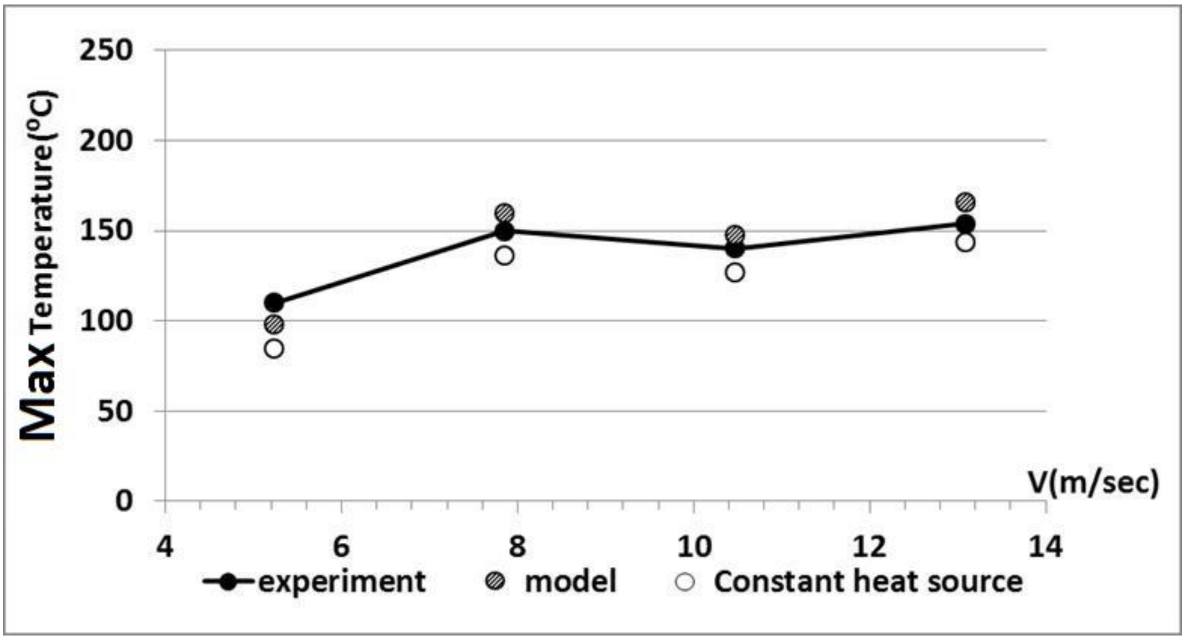

Figure 7-28 Maximum temperature in dry condition at different cutting speed using aluminum oxide wheel, depth of cut 6 µm, feed rate 1200 mm/min

Based on the overall experimental results it can be concluded that the depth of cut is the most influential grinding parameter causing temperature rise in the workpiece while increasing the feed rate or cutting speed changed the temperature very moderately. The reasons for these behaviors can be explained by using the developed models in these thesis. Increasing depth of cut resulted to increase the grinding force which increase the heat source strength. At the same time it increases the wheel workpiece contact length which resulted to increase the length of heat source. These synergistic effects make the depth of cut to be a influential parameter in workpiece temperature. The effect of feed on the other hand is small. As it was mentioned two conflicting effects counteract each other. In one hand increasing the feed rate increases the force and heat source strength. On the other hand the speed of heat source increases by increasing the feed rate which results in decreasing the exposure time.

Furthermore, grinding with a worn wheel can increase the maximum temperature via increasing the required power to cut the workpiece material. These results suggest that by using a wheel in good condition, decreasing the depth of cut and increasing cutting speed and feed rate it is possible to keep the temperature under control without sacrificing the productivity and material removal rate.

7.6 Verification of the Surface Burn Model

In order to have different workpiece temperature profiles causing the surface burn, grinding tests were carried out at different wheel speed, depth of cut and feed and wheel conditions. Table 7-3 listed the grinding conditions used for surface burn experiments.

After the grinding tests, the workpiece samples were cut, and the cross section of the workpieces were polished and etched (Nital 5%) to investigate under SEM microscope. Energy dispersive x-ray analysis (EDX) was also performed to analyze the burn layers. Figure 7-29 shows the cross section of the samples.

Table 7-3 Grinding condition for the burn experiment along with burn thickness expeimental data and predicted values

Test number	Wheel speed (m/s)	Depth of cut (µm)	Feed (mm/min)	Burn thickness (predicted)	Burn thickness (measured)	Oxygen percentage
1	2000	20	600	71	95	6.74
2	2000	30	1200	34	40	5.22
3	2000	35	2400	24	32	7.30
4	2000	30	1800	22	25	4.11
5	2000	5	1800	14	19	5.15
6	2000	20	1800	18	17	5.27

7	2000	20	1200	26	29	6.09
8	3500	15	1800	10	9	4.37

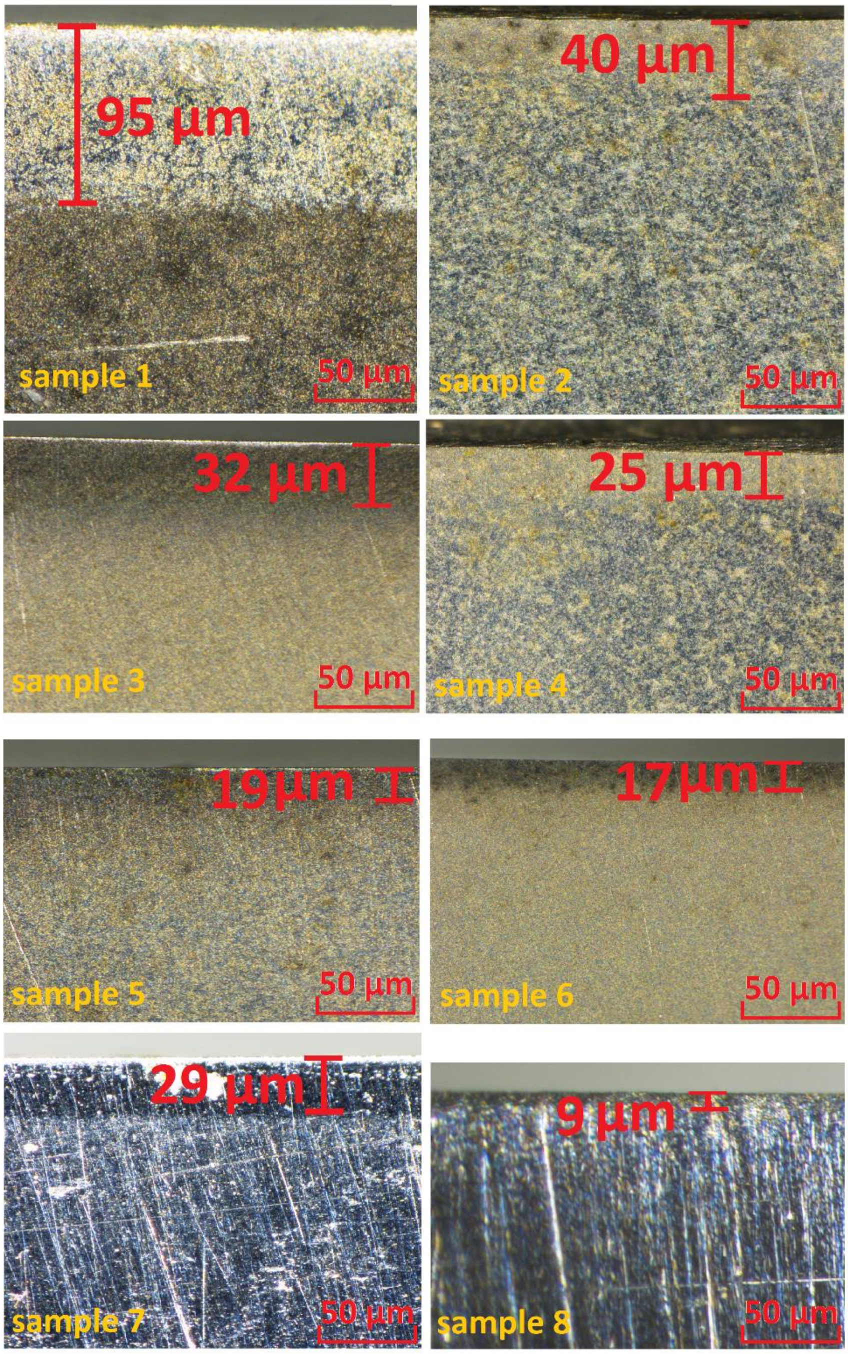

Figure 7-29 Cross-sections of the workpiece samples.

Table 7-3 shows the thickness of the burn layer of the samples. Figure 7-30 shows the temperature profile of the samples. The numbers in the figure indicates the tests listed in table 7-3.

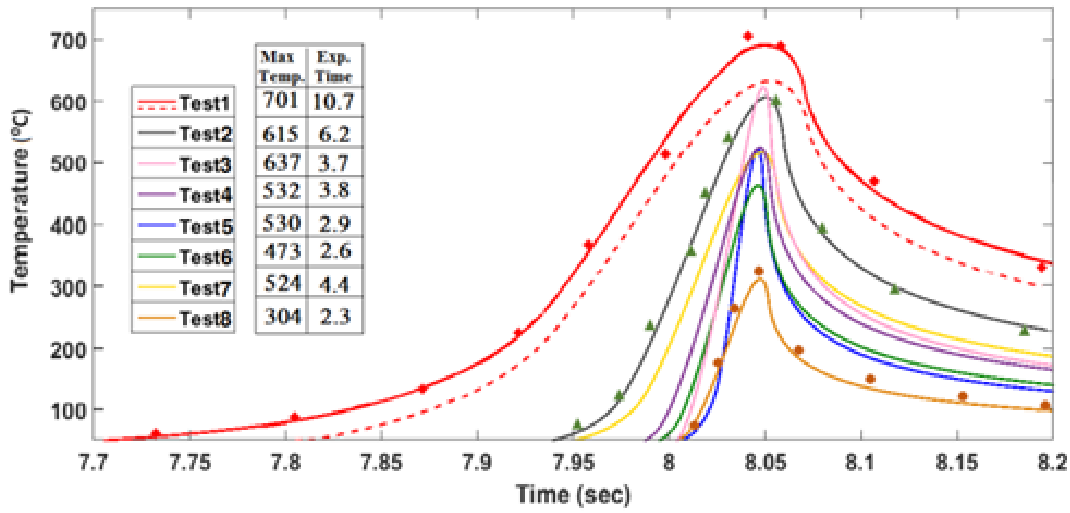

Figure 7-30 Temperature profiles of the samples.

Based on Table 7-3 and Figure 7-30, the maximum temperature in sample 1 raises approximately to 700ºC which is higher than the other tests with also longer exposure time compared to others. Accordingly, the thickest burn layer belongs to this sample. The maximum surface temperature for samples 2 and 3 are approximately the same and equal to 600ºC, while the temperature profiles are different. It is to be noted that even though the maximum workpiece temperature in sample 2 is slightly lower than that in sample 3, the burn thickness for sample 2 is about 10 µm thicker. This is due to the longer heating and cooling periods of sample 2 (6.2 vs. 3.7 sec.). Longer exposure time in sample 2 is attributed to lower feed rate. A similar observation can be made for Test 1 and 3. Although the maximum surface temperature in sample 3 is only 86ºC lower than that in sample 1, the thickness of the burn layer in sample 1 is about 3 times that in sample 3 again due to much lower feed rate used in Test 1 compared to Test 3. These results indicate that the maximum temperature of the workpiece is not the only affecting parameter in the surface burn as reported in previous studies [9-13]. While samples 4, 5 and 7 experienced approximately the same maximum temperature of about 530ºC the burn layer was different in each sample due to different workpiece exposure times. The surface burn in Sample 7 with longer exposure time (4.4 sec.) was thicker than the sample 4 having a shorter exposure time (3.8 sec.) and the burn thickness in sample 5 with shorter exposure time (2.9 sec.) was smaller than the other samples. Finally, the burn layer for sample 8 is smallest among all samples which can be attributed to its low maximum temperature and short exposure time. Based on the above discussion, it can be concluded that both the maximum workpiece temperature and the exposure time affect the burn layer. Figure 7-31 shows the SEM photo of sample 2 Rectangles A and B show two areas in the burn layer and the bulk area respectively which were analyzed for elemental composition. The results of EDS analyses and elemental composition have been shown in Figure 7-32 and 7-33 respectively. The percentage of oxygen in the bulk material is nearly zero (0.28%) while in the burn layer the oxygen percentage is significantly higher (5.22%) based on the Figure 7-33. The oxygen percentage for the other samples are between 4.11 to 7.30% (See Table 7-3) in the burn areas while in the bulk areas there is no trace of it. This observation suggests that the burn can be correlated with oxidation process and its thickness can be predicted accurately based on the current model. It is worth mentioning that carburization also occurred as the percentage of the carbon increased from 1.14% to 2.14% in the burn layer. Carbon may have been absorbed from the environment and the grit bonding materials. Due to high temperature and pressure between the aluminum oxide grits and the surface of the workpiece, aluminum also diffused to the burn layer. As the elemental composition in Fig. 6 shows, percentage of the aluminum in the burn layer is 3.29% while there is no trace of this element in the bulk area. These results indicate that in addition to the oxidation other chemical reactions such as carburization or aluminum diffusion may occur depending on the grit, bonding type, temperature and exposure time. However, the oxidation process always occurs since oxygen is constantly present in the environment.

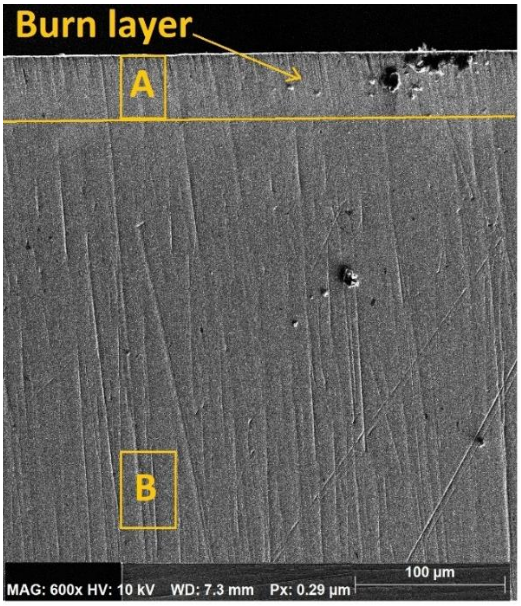

Figure 7-31 SEM photo of sample 2

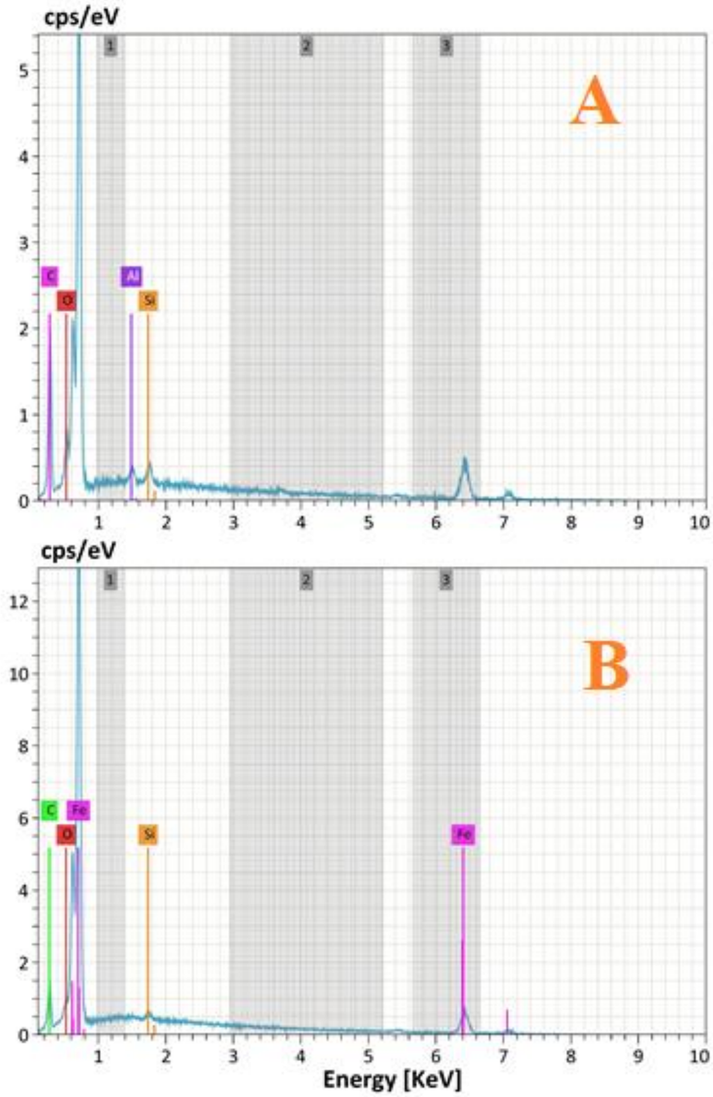

Figure 7-32 EDS analyze of sample 2 in two areas: A (Burn layer) and B(Balk area)

Element	AT. No.	Mass Norm (%)	Abs.error[%] (1 sigma)
Oxygen	8	5.22	0.01
Carbon	16	2.11	0.26
Silicon	14	0.86	0.04
Iron	26	87.04	0.45
Chromium	24	1.48	0.16
Aluminum	13	3.29	0

Area A (Burn)

Element	AT. No.	Mass Norm (%)	Abs.error[%] (1 sigma)
Oxygen	8	0.28	0.01
Carbon	16	1.14	0.26
Silicon	14	0.26	0.04
Iron	26	96.87	0.45
Chromium	24	1.45	0.16
Aluminum	13	0	0

Area B (No burn)

Figure 7-33 Elemental composition percentage in burn and unburn areas

It should be mentioned that other thermal damages cannot be predicted by the proposed burn model. Based on the developed model, surface burn has been defined as the oxidation process between workpiece material and the oxygen in the environment and metal oxidation at high temperature was applied to predict it. This does not mean that in absence of oxygen in the environment other thermal damages due to temperature rise cannot occur. Further investigation is suggested to study and correlate other thermal damages with burn and its thickness. A primarily experiment was done in this thesis to investigate occurrence of other thermal damages in absence of Oxygen. A single test was conducted in which Argon as a noble gas was used to protect the grinding zone from oxidation. Figure 7-34 shows the setup. Grinding conditions was as the same as experiment 1.

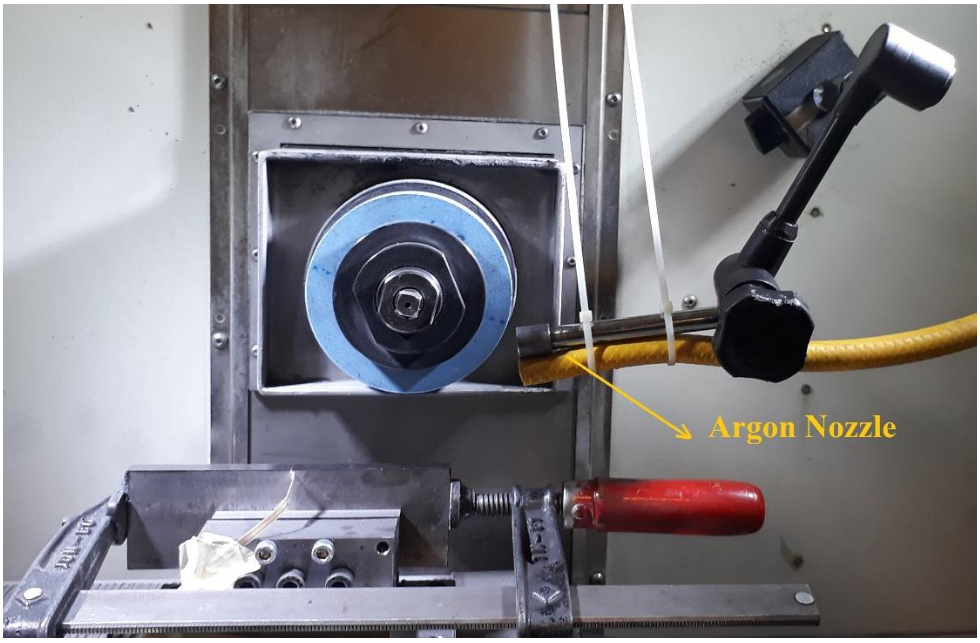

Figure 7-34 Setup of experiment to perform grinding test in absence of oxygen

Figure 7-35 shows the cross section of workpiece after the test.

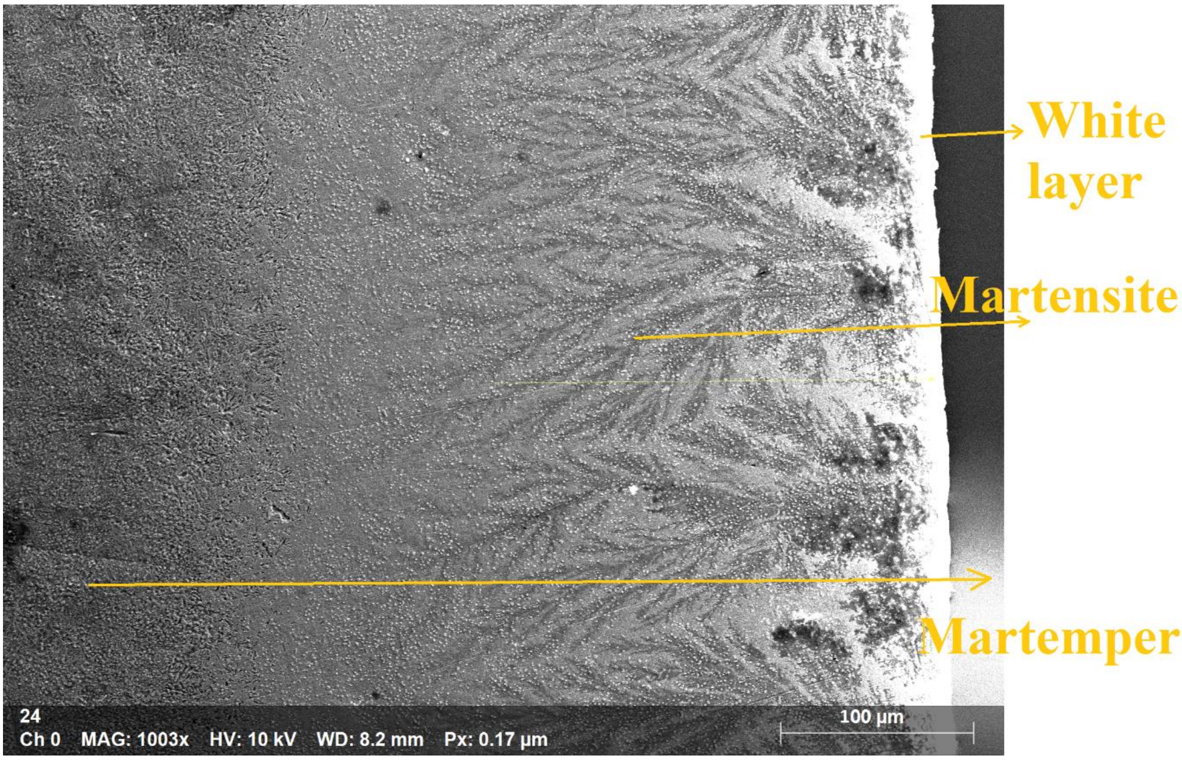

Figure 7-35 Cross section of a sample after grinding in absense of oxygen

As it can be seen in the Figure, there are different phase transformation including while phase formation, Martensite and martemper. Results of EDS analysis in different areas showed no trace of Oxygen in the workpiece material (Figure 7-36).

Element	AT. No.	Mass Norm (%)	Abs.error[%] (1 sigma)
Oxygen	8	0.20	0.01
Carbon	16	1.96	0.26
Silicon	14	0.31	0.04
Iron	26	92.78	0.45
Chromium	24	1.45	0.16
Aluminum	13	3.3	0

Figure 7-36 Elemental composition percentage in the heat affected zone in absense of Oxygen

These results indicate that other thermal damages (in this case phase transformation and formation of the white layer) are independent of oxygen presence in the environment. Further research is required to investigate and model different thermal damages during the process.

8 CONCLUSION AND RECOMMENDATIONS FOR FUTURE RESEARCH

8.1 Conclusion and Original Contributions of the thesis

In this thesis grinding process was studied in detail and different analytical models were proposed that can be used to improve part quality and productivity. The models were original and experimentally verified. Specific contributions are listed as follow:

- Individual interaction between abrasive grits and the workpiece material was modeled analytically. Statistical models were developed to represent the distribution of the grits on the wheel and their geometrical properties. Grits' properties were extracted from microscopic measurement results and it was found that the grits height distribution as one of the important influential parameters change over time and the initial normal distribution of grit height was not valid when the wheel is trued or worn.
- Active number of grits was identified by modeling grit-workpiece trajectory. The effect of run out was considered in the model for the first time. The effects of active number of grits on the process was studied and it was found that a small percentage of the total abrasive grits were engaged in the process. The active number of grit reduces more in situations where the wheel have some run out.
- The mechanics of the material removal was studied, and a new analytical force model was developed to predict the grinding force. It was found that formation of the region called dead metal zone ahead of the grit due to their very high negative rake angle along with the ploughing force constitute a large portion of the grinding force. The model could properly explain the behavior of the grinding force under various grinding conditions for different wheels. The model predicted the force in practical conditions with the total average discrepancy of 11% without needing much calibration test.
- The grinding conditions and wheel parameters should be chosen in such a way that ploughing and DMZ portions of the force should be at their minimum magnitude to have a smaller grinding force. By using the current model, the contribution of each force portion can be calculated and if necessary, grinding conditions can be modified to minimize specific grinding energy. It was found that grits with sharper edges, higher clearance angle and higher standard deviation of height create smaller force.
- In various grinding operations, the process force has a cyclic nature resulting in a discontinuous or time-dependent heat source which has been neglected in previous research. In this thesis, by including a time-dependent heat source representing force fluctuations, a 3D analytical temperature model for surface grinding was developed to predict the temperature distribution in the workpiece with higher accuracy and more detail.
- The effect of heat convection from sides of the workpiece has not been studied analytically before and was addressed in this thesis by considering adiabatic and convective boundary conditions representing the real heat convection from all surfaces of the slab workpiece in dry and wet conditions. The theoretical results

showed that considering the time-dependent nature of the heat source in the model provided more detailed information on the workpiece temperature during heating and cooling periods provided closer predictions to the measurements.

- Theoretical result indicates that the 2D solution is reliable and precise enough to predict the maximum temperature of the slab workpiece both in dry and wet conditions, whereas the convection from the side of a thin workpiece in wet condition cannot be neglected. Experimental observation is carried out to evaluate the theoretical model predictions and the effects of grinding conditions as well as wheel properties on the workpiece temperature. It is shown that the proposed model improved temperature predictions by approximately 47 % in comparison to the constant heat source-based model. Furthermore, it predicts the maximum temperature with less than 10 % average discrepancy with the measurements.
- Regarding thermal damages during the process, surface burn was investigated in this thesis and a model was proposed to predict the occurrence and the thickness of the burn layer for the first time in literature. Based on the model, surface burn can be directly correlated to the metal oxidation at high temperature. In this study, surface burn. Analysis of the surface burn layer of the ground samples by EDX detector of SEM microscopy showed a uniform existence of oxygen for different ground samples while a very small trace of this element was found in the bulk material. According to the proposed burn model, both maximum temperature and exposure time which is sum of the heating and cooling periods during the process are influential parameters in the burn thickness.

8.2 Suggestions for Future Research

Suggestions for future research are as follow:

- The active number of grits in the process is an important parameter. Direct experimental measurement of the active grits using acoustic sensors is suggested for better and more accurate procedure to validate theoretical results.
- Characteristics of dead metal zone can be further understood in a quick stop test using single grit experiment.
- An optimization procedure is suggested to build in order to integrate the developed models and find the optimum grinding conditions in practical situations.
- The developed model is suggested to modify for application of engineered wheels where the grit positions and properties are defined.
- The temperature model can be successfully applied in grinding using engineered wheels. The effect of discontinuous heat source can be studied in those wheels and optimum wheel parameters can be obtained.
- Since any unwanted thermal damages including surface burn (oxidation), phase transformation, grain size growth, residual stress, white layer formation etc. must be avoided, correlation between surface burn and other thermal damages can be studied.

REFERENCES

[1] J.P. Davim, Machining, Springer London, London, 2008. https://doi.org/10.1007/978-1-84800-213-5.

[2] S. Malkin, Grinding of metals: Theory and application, J. Appl. Metalwork. 3 (1984) 95–109. https://doi.org/10.1007/BF02833688.

[3] E. Brinksmeier, J.C. Aurich, E. Govekar, C. Heinzel, H.W. Hoffmeister, F. Klocke, J. Peters, R. Rentsch, D.J. Stephenson, E. Uhlmann, K. Weinert, M. Wittmann, Advances in modeling and simulation of grinding processes, CIRP Ann. - Manuf. Technol. 55 (2006) 667–696. https://doi.org/10.1016/j.cirp.2006.10.003.

[4] R. Cai, W.B. Rowe, Assessment of vitrified CBN wheels for precision grinding, Int. J. Mach. Tools Manuf. 44 (2004) 1391–1402. https://doi.org/10.1016/j.ijmachtools.2004.04.004.

[5] Y. Liu, A. Warkentin, R. Bauer, Y. Gong, Investigation of different grain shapes and dressing to predict surface roughness in grinding using kinematic simulations, Precis. Eng. 37 (2013) 758–764. https://doi.org/10.1016/j.precisioneng.2013.02.009.

[6] D. Aslan, E. Budak, Surface roughness and thermo-mechanical force modeling for grinding operations with regular and circumferentially grooved wheels, J. Mater. Process. Technol. 223 (2015) 75–90. https://doi.org/10.1016/j.jmatprotec.2015.03.023.

[7] T.A. Nguyen, D.L. Butler, Simulation of precision grinding process, part 1: Generation of the grinding wheel surface, Int. J. Mach. Tools Manuf. 45 (2005) 1321–1328. https://doi.org/10.1016/j.ijmachtools.2005.01.005.

[8] S. Chakrabarti, S. Paul, Numerical modelling of surface topography in superabrasive grinding, Int. J. Adv. Manuf. Technol. 39 (2008) 29–38. https://doi.org/10.1007/s00170-007-1201-y.

[9] A. Darafon, A. Warkentin, R. Bauer, Characterization of grinding wheel topography using a white chromatic sensor, Int. J. Mach. Tools Manuf. 70 (2013) 22–31. https://doi.org/10.1016/j.ijmachtools.2013.03.003.

[10] H.C. Chang, J.J.J. Wang, A stochastic grinding force model considering random grit distribution, Int. J. Mach. Tools Manuf. 48 (2008) 1335–1344. https://doi.org/10.1016/j.ijmachtools.2008.05.012.

[11] H. Yu, J. Wang, Y. Lu, Modeling and analysis of dynamic cutting points density of the grinding wheel with an abrasive phyllotactic pattern, Int. J. Adv. Manuf. Technol. 86 (2016) 1933–1943. https://doi.org/10.1007/s00170-015-8262-0.

[12] J.C. Aurich, O. Braun, G. Warnecke, Development of a superabrasive grinding wheel with defined grain structure using kinematic simulation, CIRP Ann. - Manuf. Technol. 52 (2003) 275–280. https://doi.org/10.1016/S0007-8506(07)60583-6.

[13] S. Malkin, C. Guo, Grinding Technology: Theory and Application of Machining with Abrasives, Industrial Press, 2008.

[14] R.L. Hecker, I.M. Ramoneda, S.Y. Liang, Analysis of wheel topography and grit force for grinding process modeling, J. Manuf. Process. 5 (2003) 13–23. https://doi.org/10.1016/S1526-6125(03)70036-X.

[15] J. Jiang, P. Ge, J. Hong, Study on micro-interacting mechanism modeling in grinding

process and ground surface roughness prediction, Int. J. Adv. Manuf. Technol. 67 (2013) 1035–1052. https://doi.org/10.1007/s00170-012-4546-9.

[16] W. Ding, C. Dai, T. Yu, J. Xu, Y. Fu, Grinding performance of textured monolayer CBN wheels: Undeformed chip thickness nonuniformity modeling and ground surface topography prediction, Int. J. Mach. Tools Manuf. 122 (2017) 66–80. https://doi.org/10.1016/j.ijmachtools.2017.05.006.

[17] H.N. Li, T.B. Yu, Z.X. Wang, L. Da Zhu, W.S. Wang, Detailed modeling of cutting forces in grinding process considering variable stages of grain-workpiece micro interactions, Int. J. Mech. Sci. 126 (2017) 319–339. https://doi.org/10.1016/j.ijmecsci.2016.11.016.

[18] Y. Zhang, C. Fang, G. Huang, X. Xu, Modeling and simulation of the distribution of undeformed chip thicknesses in surface grinding, Int. J. Mach. Tools Manuf. 127 (2018) 14–27. https://doi.org/10.1016/j.ijmachtools.2018.01.002.

[19] P. Koshy, V.K. Jain, G.K. Lal, Stochastic simulation approach to modelling diamond wheel topography, Int. J. Mach. Tools Manuf. 37 (1997) 751–761. https://doi.org/10.1016/S0890-6955(96)00086-7.

[20] J.L. Jiang, P.Q. Ge, W.B. Bi, L. Zhang, D.X. Wang, Y. Zhang, 2D/3D ground surface topography modeling considering dressing and wear effects in grinding process, Int. J. Mach. Tools Manuf. 74 (2013) 29–40. https://doi.org/10.1016/j.ijmachtools.2013.07.002.

[21] G. Werner, W. Koenig, Influence of work material on grinding forces, Ann. CIRP. (1978) 243–248.

[22] L. Lichun, F. Jizai, J.Peclenik, A Study of Grinding Force Mathematical Model, CIRP Ann. 29 (1980) 245–249.

[23] M.C. Shaw, Principles of abrasive processing, 1996.

[24] X. Chen, W.B. Rowe, Analysis and simulation of the grinding process. Part II: Mechanics of grinding, Int. J. Mach. Tools Manuf. 36 (1996) 883–896. https://doi.org/10.1016/0890-6955(96)00117-4.

[25] E.D. Doyle, S.K. Dean, An Insight into Grinding from a Materials Viewpoint, CIRP Ann. 29 (1980) 571–575. https://doi.org/10.1016/S0007-8506(16)30155-X.

[26] J. Buda, J. Liptak, Grinding mechanism investigation based on winning and evaluation of the chip roots, J. Mech. Work. Technol. 17 (1988) 157–165.

[27] B. Denkena, J. Köhler, J. Kästner, Chip formation in grinding: An experimental study, Prod. Eng. 6 (2012) 107–115. https://doi.org/10.1007/s11740-011-0360-8.

[28] S. Malkin, T.W. Hwang, Grinding Mechanisms for Ceramics, CIRP Ann. - Manuf. Technol. 45 (1996) 569–580. https://doi.org/10.1016/S0007-8506(07)60511-3.

[29] D. Anderson, A. Warkentin, R. Bauer, Experimental and numerical investigations of single abrasive-grain cutting, Int. J. Mach. Tools Manuf. 51 (2011) 898–910. https://doi.org/10.1016/j.ijmachtools.2011.08.006.

[30] D. Anderson, A. Warkentin, R. Bauer, Comparison of spherical and truncated cone geometries for single abrasive-grain cutting, J. Mater. Process. Tech. 212 (2012) 1946–1953. https://doi.org/10.1016/j.jmatprotec.2012.04.021.

[31] D. Axinte, C. Akgun, K. Kolluru, On grinding behavior of ductile and brittle materials, Int.

J. Mach. Tools Manuf. 74 (2013) 12–18. https://doi.org/10.1016/j.ijmachtools.2013.06.002.

[32] M. Rasim, P. Mattfeld, F. Klocke, Analysis of the grain shape influence on the chip formation in grinding, J. Mater. Process. Technol. 226 (2015) 60–68. https://doi.org/10.1016/j.jmatprotec.2015.06.041.

[33] R. Transchel, C. Leinenbach, K. Wegener, Cutting and ploughing forces for small clearance angles of hexa-octahedron shaped diamond grains, CIRP Ann. - Manuf. Technol. 63 (2014) 325–328. https://doi.org/10.1016/j.cirp.2014.03.030.

[34] C. Rubenstein, The mechanics of grinding, Int. J. Mach. Tool Des. Res. 12 (1972) 127–139.

[35] H. Chang, J.J.J. Wang, A stochastic grinding force model considering random grit distribution, Int. J. Mach. Manuf. 48 (2008) 1335–1344. https://doi.org/10.1016/j.ijmachtools.2008.05.012.

[36] D. Aslan, E. Budak, Journal of Materials Processing Technology Surface roughness and thermo-mechanical force modeling for grinding operations with regular and circumferentially grooved wheels, J. Mater. Process. Tech. 223 (2015) 75–90. https://doi.org/10.1016/j.jmatprotec.2015.03.023.

[37] A. Darafon, A. Warkentin, R. Bauer, Characterization of grinding wheel topography using a white chromatic sensor, Int. J. Mach. Tools Manuf. 70 (2013) 22–31. https://doi.org/10.1016/j.ijmachtools.2013.03.003.

[38] Y.D. Gong, B. Wang, W.S. Wang, The simulation of grinding wheels and ground surface roughness based on virtual reality technology, 129 (2002) 123–126.

[39] H. Ren, Y. Altintas, Mechanics of Machining With Chamfered Tools, 122 (2017).

[40] Y. Huang, S.Y. Liang, Force modelling in shallow cuts with large negative rake angle and large nose radius tools — application to hard turning, Int J Adv Manuf Technol. (2003) 626–632. https://doi.org/10.1007/s00170-003-1550-0.

[41] F.Z. Fang, G.X. Zhang, An experimental study of edge radius effect on cutting single crystal silicon, Int J Adv Manuf Technol. 22 (2003) 703–707. https://doi.org/10.1007/s00170-003-1593-2.

[42] J.A. Patten, W. Gao, Extreme negative rake angle technique for single point diamond nano-cutting of silicon, 25 (2001) 165–167.

[43] Y. Ohbuchi, T. Obikawa, Finite Element Modeling of Chip Formation in the Domain of Negative Rake Angle Cutting, J. Eng. Mater. Technol. 125 (2013) 324–332. https://doi.org/10.1115/1.1590999.

[44] Y. Kita, M. Ido, S. Hata, The Mechanism of Metal Removal by an Abrasive Tool, Wear. 47 (1978) 185–193.

[45] W. Lortz, A model of the cutting mechanism in grinding, Wear. 53 (1979) 115–128. https://doi.org/10.1016/0043-1648(79)90223-0.

[46] S. Agarwal, P.V. Rao, International Journal of Machine Tools & Manufacture Predictive modeling of force and power based on a new analytical undeformed chip thickness model in ceramic grinding, Int. J. Mach. Tools Manuf. 65 (2013) 68–78. https://doi.org/10.1016/j.ijmachtools.2012.10.006.

[47] T. Warren, Modelling of ceramic grinding processes Part I . Number of cutting points and grinding forces per . grit, 6 (1997).

[48] D. Wang, P. Ge, W. Bi, J. Jiang, Grain trajectory and grain workpiece contact analyses for modeling of grinding force and energy partition, Int. J. Adv. Manuf. Technol. 70 (2014) 2111–2123. https://doi.org/10.1007/s00170-013-5428-5.

[49] C. Yao, T. Wang, W. Xiao, X. Huang, J. Ren, Experimental study on grinding force and grinding temperature of Aermet 100 steel in surface grinding, Elsevier B.V., 2014. https://doi.org/10.1016/j.jmatprotec.2014.04.013.

[50] B.W. Rowe, Principles of Modern Grinding Technology: Vol-2, 2014.

[51] J. C. Jaeger, Moving sources of heat and the temperature at sliding contacts, Proc. R. Soc. New South Wales. 76 (1942) 203–224. https://doi.org/10.1109/TCST.2018.2852743.

[52] Carslaw H. S., J.C. Jaeger, Conduction of Heat in Solids, second edi, Oxford University Press, London, 1959.

[53] S.Z. Shuja, B.S. Yilbas, Laser produced melt pool: Influence of laser intensity parameter on flow field in melt pool, Opt. Laser Technol. 43 (2011) 767–775. https://doi.org/10.1016/j.optlastec.2010.12.003.

[54] X. Deng, J. Fu, Y. Zhang, A Predictive Model for Temperature Rise of Spindle–Bearing Integrated System, J. Manuf. Sci. Eng. 137 (2015) 021014. https://doi.org/10.1115/1.4029445.

[55] D. Couëdel, P. Rogeon, P. Lemasson, M. Carin, J.C. Parpillon, R. Berthet, 2D-heat transfer modelling within limited regions using moving sources: Application to electron beam welding, Int. J. Heat Mass Transf. 46 (2003) 4553–4559. https://doi.org/10.1016/S0017-9310(03)00288-6.

[56] A.A.O. Tay, A review of methods of calculating machining temperature, J. Mater. Process. Tech. 36 (1993) 225–257. https://doi.org/10.1016/0924-0136(93)90033-3.

[57] S. Malkin, C. Guo, Thermal Analysis of Grinding, CIRP Ann. - Manuf. Technol. 56 (2007) 760–782. https://doi.org/10.1016/j.cirp.2007.10.005.

[58] W.B. Rowe, M.N. Morgan, D.A. Allanson, An Advance in the Modelling of Thermal Effects in the Grinding Process, CIRP Ann. - Manuf. Technol. 40 (1991) 339–342. https://doi.org/10.1016/S0007-8506(07)62001-0.

[59] N. R. Des Ruisseaux, R.D. Zerkle, Temperature in Semi-Infinite and Cylindrical Bodies Subjected to Moving Heat Sources and Surface Cooling, ASME J. Heat Transf. 92 (1970) 456–464.

[60] C. Guo, S. Malkin, Analysis of Energy Partition in Grinding, J. Eng. Ind. 117 (1995) 55–61. https://doi.org/10.1115/1.2803278.

[61] D. Anderson, A. Warkentin, R. Bauer, Comparison of numerically and analytically predicted contact temperatures in shallow and deep dry grinding with infrared measurements, Int. J. Mach. Tools Manuf. 48 (2008) 320–328. https://doi.org/10.1016/j.ijmachtools.2007.10.010.

[62] T. Jin, W.B. Rowe, D. McCormack, Temperatures in deep grinding of finite workpieces, Int. J. Mach. Tools Manuf. 42 (2002) 53–59. https://doi.org/10.1016/S0890-6955(01)00094-3.

[63] S.M. Shah, D. Nélias, M. Zain-Ul-Abdein, M. Coret, Numerical simulation of grinding induced phase transformation and residual stresses in AISI-52100 steel, Finite Elem. Anal. Des. 61 (2012) 1–11. https://doi.org/10.1016/j.finel.2012.05.010.

[64] A. Brosse, P. Naisson, H. Hamdi, J.M. Bergheau, Temperature measurement and heat flux characterization in grinding using thermography, J. Mater. Process. Technol. 201 (2008) 590–595. https://doi.org/10.1016/j.jmatprotec.2007.11.267.

[65] Y. Tian, B. Shirinzadeh, D. Zhang, X. Liu, D. Chetwynd, Effects of the heat source profiles on the thermal distribution for ultraprecision grinding, Precis. Eng. 33 (2009) 447–458. https://doi.org/10.1016/j.precisioneng.2008.12.002.

[66] T. Jin, G.Q. Cai, Analytical Thermal Models of Oblique Moving Heat Source for Deep Grinding and Cutting, J. Manuf. Sci. Eng. 123 (2002) 185. https://doi.org/10.1115/1.1343458.

[67] W.B. Rowe, T. Jin, Temperatures in High Efficiency Deep Grinding (HEDG), CIRP Ann. - Manuf. Technol. Volume 50 (2001) 205–208. https://doi.org/10.1016/S0007-8506(07)62105-2.

[68] D. Wang, S. Sun, J. Jiang, X. Liu, The profile analysis and selection guide for the heat source on the finished surface in grinding, J. Manuf. Process. 30 (2017) 178–186. https://doi.org/10.1016/j.jmapro.2017.09.023.

[69] Z.B. Hou, R. Komanduri, On the mechanics of the grinding process, Part II - Thermal analysis of fine grinding, Int. J. Mach. Tools Manuf. 44 (2004) 247–270. https://doi.org/10.1016/j.ijmachtools.2003.09.008.

[70] B. Rajmohan, V. Radhakrishnan, A study on the thermal aspects of chips in grinding, Int. J. Mach. Tools Manuf. 32 (1992) 563–569. https://doi.org/10.1016/0890-6955(92)90045-I.

[71] S. Kohli, C. Guo, S. Malkin, Energy Partition to the Workpiece for Grinding with Aluminum Oxide and CBN Abrasive Wheels, J. Eng. Ind. 117 (2008) 160. https://doi.org/10.1115/1.2803290.

[72] X. Xu, Experimental study on temperatures and energy partition at the diamond-granite interface in grinding, Tribol. Int. 34 (2001) 419–426. https://doi.org/10.1016/S0301-679X(01)00039-1.

[73] C. Guo, S. Malkin, Energy partition and cooling during grinding, J. Manuf. Process. 2 (2000) 151–157. https://doi.org/10.1016/S1526-6125(00)70116-2.

[74] T. Jin, G.Q. Cai, H.D. Jeong, N.K. Kim, Study on heat transfer in super-high-speed grinding: Energy partition to the workpiece in HEDG, J. Mater. Process. Technol. 111 (2001) 261–264. https://doi.org/10.1016/S0924-0136(01)00530-1.

[75] A.S. Lavine, A Simple Model for Convective Cooling During the Grinding Process, J. Eng. Ind. 110 (2009) 1. https://doi.org/10.1115/1.3187837.

[76] A.S. Lavine, T.C. Jen, Coupled heat transfer to workpiece, wheel, and fluid in grinding, and the occurrence of workpiece burn, Int. J. Heat Mass Transf. 34 (1991) 983–992. https://doi.org/10.1016/0017-9310(91)90009-4.

[77] W.B. Rowe, Thermal analysis of high efficiency deep grinding, Int. J. Mach. Tools Manuf. 41 (2001) 1–19. https://doi.org/10.1016/S0890-6955(00)00074-2.

[78] J. Li, J.C.M. Li, Temperature distribution in workpiece during scratching and grinding,

Mater. Sci. Eng. A. 409 (2005) 108–119. https://doi.org/10.1016/j.msea.2005.07.057.

[79] M. Putz, M. Cardone, M. Dix, R. Wertheim, Analysis of workpiece thermal behaviour in cut-off grinding of high-strength steel bars to control quality and efficiency, CIRP Ann. (2019). https://doi.org/10.1016/j.cirp.2019.04.023.

[80] J. Jiang, P. Ge, S. Sun, D. Wang, Y. Wang, Y. Yang, From the microscopic interaction mechanism to the grinding temperature field: An integrated modelling on the grinding process, Int. J. Mach. Tools Manuf. 110 (2016) 27–42. https://doi.org/10.1016/j.ijmachtools.2016.08.004.

[81] Z. Wang, T. Yu, X. Wang, T. Zhang, J. Zhao, P.H. Wen, Grinding temperature field prediction by meshless finite block method with double infinite element, Int. J. Mech. Sci. 153–154 (2019) 131–142. https://doi.org/10.1016/j.ijmecsci.2019.01.037.

[82] A.M.O. Mohamed, A. Warkentin, R. Bauer, Use of surface roughness measurements to improve the estimation of the heat partition in grinding, J. Mater. Process. Technol. 211 (2011) 566–572. https://doi.org/10.1016/j.jmatprotec.2010.11.008.

[83] P.S. Balaji, V. Yadava, Three dimensional thermal finite element simulation of electro-discharge diamond surface grinding, Simul. Model. Pract. Theory. 35 (2013) 97–117. https://doi.org/10.1016/j.simpat.2013.03.007.

[84] D.W.M. Veldman, R.H.B. Fey, H.J. Zwart, M.M.J. van de Wal, J.D.B.J. van den Boom, H. Nijmeijer, Semi-analytic approximation of the temperature field resulting from moving heat loads, Int. J. Heat Mass Transf. 122 (2018) 128–137. https://doi.org/10.1016/j.ijheatmasstransfer.2018.01.085.

[85] H.N. Li, D. Axinte, On a stochastically grain-discretised model for 2D/3D temperature mapping prediction in grinding, Int. J. Mach. Tools Manuf. 116 (2017) 60–76. https://doi.org/10.1016/j.ijmachtools.2017.01.004.

[86] H.N. Li, D. Axinte, On the inverse design of discontinuous abrasive surface to lower friction-induced temperature in grinding: An example of engineered abrasive tools, Int. J. Mach. Tools Manuf. 132 (2018) 50–63. https://doi.org/10.1016/j.ijmachtools.2018.04.006.

[87] B. He, C. Wei, S. Ding, Z. Shi, A survey of methods for detecting metallic grinding burn, Meas. J. Int. Meas. Confed. 134 (2019) 426–439. https://doi.org/10.1016/j.measurement.2018.10.093.

[88] W.B. Rowe, M.N. Morgan, S.C.E. Black, B. Mills, A Simplified Approach to Control of Thermal Damage in Grinding, CIRP Ann. - Manuf. Technol. 45 (1996) 299–302. https://doi.org/10.1016/S0007-8506(07)63067-4.

[89] ASM Handbook Volume 04: Heat Treating, n.d.

[90] S. Malkin, Thermal Aspects of Grinding, Part 2 Surface Temperatures and Workpiece Burn, ASME. (1974) 1184–1191.

[91] J.S. Tang, X.F. Pu, H.J. Xu, Y.Z. Zhang, Studies on Mechanisms and Improvement of Workpiece Burn During Grinding of Titanium Alloys, CIRP Ann. - Manuf. Technol. 39 (1990) 353–356. https://doi.org/10.1016/S0007-8506(07)61071-3.

[92] M.K. Sinha, D. Setti, S. Ghosh, P. Venkateswara Rao, An investigation on surface burn during grinding of Inconel 718, J. Manuf. Process. 21 (2016) 124–133. https://doi.org/10.1016/j.jmapro.2015.12.004.

[93] A. Bell, T. Jin, D.J. Stephenson, Burn threshold prediction for High Efficiency Deep Grinding, Int. J. Mach. Tools Manuf. 51 (2011) 433–438. https://doi.org/10.1016/j.ijmachtools.2011.01.006.

[94] B. Lin, K. Zhou, J. Guo, Q.Y. Liu, W.J. Wang, Influence of grinding parameters on surface temperature and burn behaviors of grinding rail, Tribol. Int. 122 (2018) 151–162. https://doi.org/10.1016/j.triboint.2018.02.017.

[95] T. Jianshe, P. Xuefeng, X. Hongjun, Z. Youzhen, The Prediction and Control of Workpiece Burn During Grinding Process - Application of Graphite-Penetrated Wheels, CIRP Ann. - Manuf. Technol. 35 (1986) 227–230. https://doi.org/10.1016/S0007-8506(07)61876-9.

[96] W.B. Rowe, S.C.E. Black, B. Mills, H.S. Qi, M.N. Morgan, Experimental Investigation of Heat Transfer in Grinding, CIRP Ann. - Manuf. Technol. 44 (1995) 329–332. https://doi.org/10.1016/S0007-8506(07)62336-1.

[97] W.B. Rowe, J.A. Pettit, A. Boyle, J.L. Moruzzi, Avoidance of Thermal Damage in Grinding and Prediction of the Damage Threshold, CIRP Ann. - Manuf. Technol. 37 (1988) 327–330. https://doi.org/10.1016/S0007-8506(07)61646-1.

[98] M. Neslušan, J. Čížek, K. Kolařík, P. Minárik, M. Čilliková, O. Melikhova, Monitoring of grinding burn via Barkhausen noise emission in case-hardened steel in large-bearing production, J. Mater. Process. Technol. 240 (2017) 104–117. https://doi.org/10.1016/j.jmatprotec.2016.09.015.

[99] A. Thanedar, G.G. Dongre, R. Singh, S.S. Joshi, Surface integrity investigation including grinding burns using barkhausen noise (BNA), J. Manuf. Process. 30 (2017) 226–240. https://doi.org/10.1016/j.jmapro.2017.09.026.

[100] G. Dobre, M.R. Vladu, Grinding Burn on Gears: Correlation Between Flank-Load-Carrying Capacity and Material Characteristics, in: Power Transm. Springer, 2013. https://doi.org/10.1007/978-94-007-6558-0.

[101] Y.M. Ali, L.C. Zhang, A fuzzy model for predicting burns in surface grinding of steel, Int. J. Mach. Tools Manuf. 44 (2004) 563–571. https://doi.org/10.1016/j.ijmachtools.2003.10.030.

[102] A.K. Srivastava, D.B. Rogers, M.A. Elbestawi, Workpiece burn and surface finish during controlled force robotic disk grinding, Int. J. Mach. Tools Manuf. 32 (1992) 797–809. https://doi.org/10.1016/0890-6955(92)90032-C.

[103] R. Dražumerič, R. Roininen, J. Badger, P. Krajnik, Temperature-based method for determination of feed increments in crankshaft grinding, J. Mater. Process. Technol. 259 (2018) 228–234. https://doi.org/10.1016/j.jmatprotec.2018.04.032.

[104] E. Ozlu, A. Molinari, E. Budak, Two-zone analytical contact model applied to orthogonal cutting, Mach. Sci. Technol. 14 (2010) 323–343. https://doi.org/10.1080/10910344.2010.512794.

[105] W.A. Kline, R.E. DeVor, The effect of runout on cutting geometry and forces in end milling, Int. J. Mach. Tool Des. Res. 23 (1983) 123–140. https://doi.org/10.1016/0020-7357(83)90012-4.

[106] E. Budak, E. Ozlu, H. Bakioglu, Z. Barzegar, CIRP Annals - Manufacturing Technology Thermo-mechanical modeling of the third deformation zone in machining for prediction of cutting forces, CIRP Ann. - Manuf. Technol. 65 (2016) 121–124. https://doi.org/10.1016/j.cirp.2016.04.110.

[107] X. Jin, Y. Altintas, Slip-line field model of micro-cutting process with round tool edge effect, J. Mater. Process. Technol. 211 (2011) 339–355. https://doi.org/10.1016/j.jmatprotec.2010.10.006.

[108] Y. Altintas, Manufacturing automation, 2012.

[109] G.. Stabler, The chip flow law and its consequences, Proc. 5th Mach. Tool Des. Res. Conf. (1964) 243–251.

[110] E. Budak, E. Ozlu, Development of a thermomechanical cutting process model for machining process simulations, CIRP Ann. - Manuf. Technol. 57 (2008) 97–100. https://doi.org/10.1016/j.cirp.2008.03.008.

[111] A.C. Ramos, H. Autenrieth, T. Strauß, M. Deuchert, J. Hoffmeister, V. Schulze, Characterization of the transition from ploughing to cutting in micro machining and evaluation of the minimum thickness of cut, J. Mater. Process. Technol. 212 (2012) 594–600. https://doi.org/10.1016/j.jmatprotec.2011.07.007.

[112] Y. Kita, M. Ido, Y. Tuji, The influence of the cutting speed on the mechanism of metal removal by an abrasive tool, Wear. 71 (1981) 55–63. https://doi.org/10.1016/0043-1648(81)90139-3.

[113] M.R. Movahhedy, Y. Altintas, M.S. Gadala, Numerical Analysis of Metal Cutting With Chamfered and Blunt Tools, ASME. 124 (2002) 178–188. https://doi.org/10.1115/1.1445147.

[114] E. Ozlu, A. Molinari, E. Budak, Two-zone analytical contact model applied to orthogonal cutting, Mach. Sci. Technol. 14 (2010) 323–343. https://doi.org/10.1080/10910344.2010.512794.

[115] H.N. Li, D. Axinte, Textured grinding wheels: A review, Int. J. Mach. Tools Manuf. 109 (2016) 8–35. https://doi.org/10.1016/j.ijmachtools.2016.07.001.

[116] T. Foeckerer, M.F. Zaeh, O.B. Zhang, A three-dimensional analytical model to predict the thermo-metallurgical effects within the surface layer during grinding and grind-hardening, Int. J. Heat Mass Transf. 56 (2013) 223–237. https://doi.org/10.1016/j.ijheatmasstransfer.2012.09.029.

[117] G.H. Meier, High Temperature Oxidation and Corrosion of Metal-Silicides, 1986. https://doi.org/10.1557/proc-81-443.

[118] R.Y. Chen, W.Y.D. Yuen, Review of the high-temperature oxidation of iron and carbon steels in air or oxygen, Oxid. Met. 59 (2003) 433–468. https://doi.org/10.1023/A:1023685905159.

[119] A.S. Khanna, High Temperature Oxidation, in: Handb. Environ. Degrad. Mater., Second Edi, Elsevier, 2012: pp. 127–194. https://doi.org/10.1016/B978-1-4377-3455-3.00005-5.

[120] H. Abuluwefa, The effect of oxygen concentration on the oxidation of low-carbon steel in the temperature range 1000 to 1250°C, Oxid. Met. 46 (1996) 423–440. https://doi.org/10.1007/BF01048639.

[121] F. Klocke, D. Lung, S. Buchkremer, Inverse identification of the constitutive equation of inconel 718 and AISI 1045 from FE machining simulations, Procedia CIRP. 8 (2013) 212–217. https://doi.org/10.1016/j.procir.2013.06.091.

[122] B. Shen, G. Xiao, C. Guo, S. Malkin, A.J. Shih, Thermocouple Fixation Method for Grinding Temperature Measurement, J. Manuf. Sci. Eng. 130 (2008) 051014.

https://doi.org/10.1115/1.2976142.

[123] A.D. Batako, W.B. Rowe, M.N. Morgan, Temperature measurement in high efficiency deep grinding, Int. J. Mach. Tools Manuf. 45 (2005) 1231–1245. https://doi.org/10.1016/j.ijmachtools.2005.01.013.

[124] G.D. Ruxton, D.M. Wilkinson, M. Neuhäuser, Advice on testing the null hypothesis that a sample is drawn from a normal distribution, Anim. Behav. 107 (2015) 249–252. https://doi.org/10.1016/j.anbehav.2015.07.006.

[125] A. Ghasemi, S. Zahediasl, Normality tests for statistical analysis: A guide for non-statisticians, Int. J. Endocrinol. Metab. 10 (2012) 486–489. https://doi.org/10.5812/ijem.3505.

[126] H.C. Thode, Testing for normality, Marcel Dekker Inc, New York, n.d.

[127] S.G. Coles, An introduction to Statistical Modeling of Extreme Values, 2001. https://doi.org/10.1007/978-1-4471-3675-0.

[128] X. Zhang, B. Lin, H. Xi, Validation of an analytical model for grinding temperatures in surface grinding by cup wheel with numerical and experimental results, Int. J. Heat Mass Transf. 58 (2013) 29–42. https://doi.org/10.1016/j.ijheatmasstransfer.2012.11.022.

[129] T.D. Howes, K. Neailey, A.J. Harrison, P.A. McKeown, Fluid Film Boiling in Shallow Cut Grinding, CIRP Ann. 36 (1987) 223–226. https://doi.org/10.1016/S0007-8506(07)62591-8.

[130] J. Zhang, P. Ge, T.C. Jen, L. Zhang, Experimental and numerical studies of AISI1020 steel in grind-hardening, Int. J. Heat Mass Transf. 52 (2009) 787–795. https://doi.org/10.1016/j.ijheatmasstransfer.2008.06.037.